THE UNIVERSITY OF CHICAGO

MEASUREMENT OF THE $WW + WZ$ PRODUCTION CROSS SECTION IN A SEMILEPTONIC DECAY MODE AT CDF

A DISSERTATION SUBMITTED TO
THE FACULTY OF THE DIVISION OF THE PHYSICAL SCIENCES
IN CANDIDACY FOR THE DEGREE OF
DOCTOR OF PHILOSOPHY

DEPARTMENT OF PHYSICS

BY
MARTINA HURWITZ

CHICAGO, ILLINOIS
MARCH 2010

TABLE OF CONTENTS

LIST OF FIGURES

LIST OF TABLES

ACKNOWLEDGEMENTS

This thesis would not have been possible without the help and support of many, many people. First and foremost, I'd like to thank my advisors, Jim Pilcher and Florencia Canelli. Jim was a very good advisor, always closely interested in the work I was doing and ready with useful recommendations. He kept me away from things that would waste my time and promoted my work within ATLAS. When I moved to CDF, Florencia adopted me and helped me get integrated very quickly. She devoted a ton of time to me and my questions and was always willing to think about even the smallest issues. Thanks also to both of them for their continued support as I move forward.

The CDF collaboration as a whole was very welcoming to me, allowing me to come in and do an analysis on data that I did not help collect. The collaborative atmosphere at CDF is great and it always felt like people's comments and criticisms were scientific and in the spirit of improving our analysis. I'd particularly like to thank the CDF spokespeople, Rob Roser and Jaco Konigsberg, and the Higgs group convenors, Ben Kilminster and Eric James, for their support.

Much of the ground work for this analysis was laid by the WH and single top matrix element group: Barbara Alvarez, Florencia Canelli, Bruno Casal, Peter Dong, Ricardo Eusebi, Craig Group, Enrique Palencia, and Bernd Stelzer. They set up a framework that was easy to understand and patiently answered all of my questions. The godparents of our analysis, Mark Kruse, Tom Junk, and Gene Flanagan gave helpful comments on our work and helped see the analysis through to completion. Tom was especially helpful in sorting out various statistical questions.

Although this thesis does not contain any ATLAS work, I spent five years working on ATLAS during graduate school. I met many smart colleagues who also became my friends, and learned a lot about detectors and high energy physics. I particularly enjoyed all of my time in the TileCal community: taking shifts at the testbeam; continuing to analyze the data five years later; building up "Team 5;" being much too precise about the CIS calibration; and of course eating Italian, Spanish, American, and Brazilian food at the BBQs. I'm grateful to Bob Stanek, Ana Henriques, Irene Vichou, Richard Teuscher, Giulio Usai, Esteban Fullana, Belen Salvachua, Gerolf Schlager, Iacopo Vivarelli, Andrea Dotti, Imai Jen-La Plante, Claudio Santoni, Vincent Giangiobbe, Lukas Pribyl, Monica Dunford, and many other members of TileCal for all of those years of work and fun. As I moved towards physics analysis on ATLAS, Ambreesh Gupta, Jimmy Proudfoot, Amir Farbin, Tancredi Carli, Martine Bosman, and Tom LeCompte were all helpful advisors. Finally, thanks to the rest of the Chicago ATLAS group, including Mel Schochet, Mark Oreglia, Frank Merritt, Kelby Anderson, Eric Feng, Georgios Choudalakis, and Peter Onyisi for their help over the years.

Outside of work, many friends have made the past several years bearable and even fun. Monica Dunford became a close friend and someone I could always count on to boost my ego. Of course, she's also a great training buddy, and I hope at some point soon we'll be training for triathlons together. Imai Jen-La Plante is also a great friend and a generous sharer of snacks; I always looked forward to taking a break and chatting about real life with her. I'm so glad I met Pauline Gagnon and Iris Tetford, who are very cool women who know how to run, eat, and enjoy life. Belen Salvachua and Esteban Fullana, two of the first people I met on TileCal, have been close friends both at CERN and now in Chicago and Naperville. Their hospitality and generosity never cease to amaze me. Barbara Alvarez has taken me under her wing at Fermilab; it's always fun to crash her

Spanish lunches and whine about the software to her.

My first few years in Chicago were fun thanks to the other students in my class, including Wojtek, Laura, Ben, Robert, Andy, Raf, Matthew, and Dimitris. Thanks to Raf, Margo, and Andy for their willingness to help in an emergency when I came back to Chicago after years of being out of touch. I enjoyed eating weekly cookies with the HEP students, Collin, Erin, and Jahred; more recently, thanks to Jahred for this thesis template and to him and Wojtek for introducing me to foie gras (though I have no intention of consuming it again). It was great meeting and trying to be as cool as Jim Lamb and Steven while at CERN. And nowadays, I always look forward to the conversations over lunch with Constantinos, Antonio, Anton, Shawn, Joe, and Chris.

I am very fortunate to have a supportive and loving family. I can always count on them if I need help, and it's wonderful to have people to talk to and a place to go in good times or bad. It was nice to have the chance to see more of Tante Chrille, Onkel Hans, Philipp, Mathilde, and Omi while I was living in Europe. Thanks to them for their hospitality and marzipan. Mom, Dad, and Stefan are unconditionally supportive, which makes everything in life seem easier. I always look forward to going home to Saratoga and relaxing completely: shopping and baking with Mom; doing crosswords and watching sports with Dad; trying to fix computers with Stef; and arguing with everyone just for fun.

Finally, thanks to my best friend and partner Matt for many things, including innumerable snacks.

ABSTRACT

The measurement of the $WW + WZ$ production cross section in a semileptonic decay mode is presented. The measurement is carried out with 4.6 fb^{-1} of integrated luminosity collected by the CDF II detector in $\sqrt{s} = 1.96$ TeV proton-antiproton collisions at the Tevatron. The main experimental challenge is identifying the signal in the overwhelming background from W+jets production. The modeling of the W+jets background is carefully studied and a matrix element technique is used to build a discriminant to separate signal and background. The cross section of $WW + WZ$ production is measured to be $\sigma(p\bar{p} \rightarrow WW + WZ) = 16.5^{+3.3}_{-3.0}$ pb, in agreement with the next-to-leading order theoretical prediction of 15.1 ± 0.9 pb. The significance of the signal is evaluated to be 5.4σ. This measurement is an important milestone in the search for the Standard Model Higgs boson at the Tevatron.

CHAPTER 1

INTRODUCTION

The Standard Model of particle physics has been remarkably successful in describing experimental results over the last several decades. But one important particle in the model, the Higgs boson, has not yet been observed. In addition, there is strong theoretical motivation for the existence of new particles and interactions at energy scales beyond those explored by experiments so far.

The Standard Model has been tested extensively at the current highest-energy collider in the world, the Tevatron. No significant deviations from prediction have been observed. Current activity at the Tevatron is focused on precise measurements of Standard Model parameters, where small deviations from predictions could indicate the presence of new physics, and the search for the Standard Model Higgs boson. In most analyses at the Tevatron, the search for small effects requires sophisticated techniques that take advantage of every piece of information available from the experiment.

This thesis presents the measurement of the $WW + WZ$ production cross section in a channel with a lepton and two jets. The challenge of the analysis lies in extracting a small signal from large backgrounds. This analysis is closely related to the search for the Higgs boson at the Tevatron, and can eventually also be used to explore new physics theories. Matrix element calculations are used to separate the $WW + WZ$ signature from the backgrounds.

The rest of this chapter presents some aspects of Standard Model theory relevant to the analysis, as well as the experimental context of the measurement. The experimental

	Generation I		Generation II		Generation III		Charge
Quarks	u	1.5 - 3.3 MeV	c	1.27 GeV	t	171.2 GeV	$2/3e$
	d	3.5 - 6.0 MeV	s	104 MeV	b	4.2 GeV	$-1/3e$
Leptons	e	0.511 MeV	μ	106 MeV	τ	1780 MeV	$-e$
	ν_e	< 2 eV	ν_μ	< 2 eV	ν_τ	< 2 eV	0

Table 1.1: Mass and charge of the fermions.

apparatus used for the analysis is described in Chapter 2. Chapters 3 and 4 present the details of the event selection and Monte Carlo modeling, followed by a description of the matrix element methodology in Chapter 5. The likelihood fit used for the measurement and the systematic uncertainties that must be taken into account are described in Chapters 6 and 7. Finally, the results are presented in Chapter 8.

1.1 Standard Model

The Standard Model of particle physics (SM) contains the current understanding of particles and their interactions. According to the SM, matter is composed of fundamental particles called fermions. The interactions due to three forces, the electromagnetic force, the weak force, and the strong force, are described in the SM by the $SU(3) \times SU(2) \times U(1)$ gauge group. Gauge bosons mediate each of these forces.

Twelve types of fermions exist: six leptons (electron, electron neutrino, muon, muon neutrino, tau, and tau neutrino) and six quarks (up, down, charm, strange, bottom, and top). All of these particles have corresponding anti-particles. The fermions are often grouped into three generations, ordered by mass, as shown in Figure 1.1. The masses and charges of the 12 fermions are listed in Table 1.1 [1].

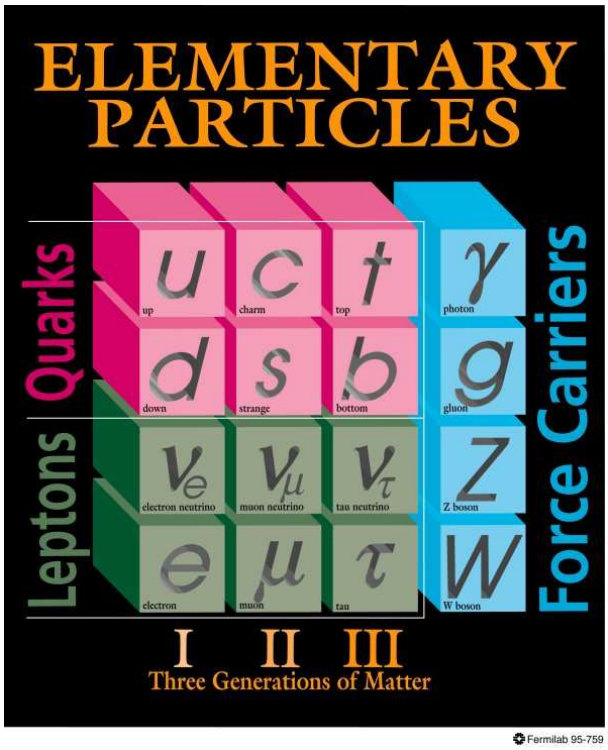

Figure 1.1: Particle content of the Standard Model.

1.1.1 Electroweak interactions

The electroweak sector of the SM unifies the electromagnetic and weak forces into an $SU(2) \times U(1)$ gauge group. The electromagnetic force acts between charged particles and is mediated by the massless photon (γ particle). The weak force, as its name implies, is feeble with respect to the electromagnetic (and strong) forces, but it can act on any quark or lepton. The weak force is the only force that allows quarks or leptons to change flavor, as well as being the only force that acts on neutrinos. The massive W and Z bosons mediate the weak force. Two W bosons with charges of $+1$ and -1 exist, where the charge is in units of the electron charge; the W boson mass is $m_W = 81.4$ GeV/c^2. The Z boson is neutral with a mass of $m_Z = 91.2$ GeV/c^2 [1].

The high mass of the W and Z gauge bosons cannot be accommodated in the $SU(2) \times U(1)$ gauge group without introduction of an additional field. The Higgs mechanism introduces this additional field with a structure that leads to spontaneous electroweak symmetry breaking, resulting in massive W and Z bosons and a massless photon. The Higgs mechanism also predicts the existence of an additional neutral scalar boson, the Higgs boson. The mass of the Higgs boson is not predicted by the SM. It has not yet been observed experimentally; the experimental limits on its existence are described in more detail in Section 1.3.

1.1.2 Strong interactions

The strong force acts on quarks and is described by Quantum Chromodynamics (QCD). In QCD, quarks are assigned a color charge, and color must be conserved in strong interactions. The strong force is mediated by the gluon, a neutral and massless boson, which

carries a color and an anticolor charge. As a result gluons can interact with each other as well as with quarks.

One important property of QCD is asymptotic freedom, or the fact that the strong force becomes weaker at shorter distances. A second important property called color confinement requires that a particle with color charge (e.g. a quark) cannot exist in isolation; rather it must be bound into a color-neutral hadron. These two properties have an important phenomenological effect in particle physics experiments: if a quark or gluon is produced by a collision, it cannot exist on its own but rather becomes a jet of hadrons. These jets of hadrons, or jets for short, are what we detect in an experiment and are used to infer the presence of quarks and gluons in the final state.

1.2 WW and WZ production and decay

A measurement of diboson production at colliders allows a test of the electroweak SM predictions for gauge boson self-interactions. Pairs of W bosons (WW events) were first observed at electron-positron collider LEP, where precision measurements of the WW cross section in several decay channels were carried out. The observed cross sections agreed well with Standard Model predictions. Production of a W boson in association with a Z boson (WZ) was not possible at LEP.

At the proton-antiproton Tevatron collider at Fermilab (described further in Section 2.1), pairs of W bosons (WW events) and a W boson in association with a Z boson (WZ events) can be produced via the diagrams shown in Figures 1.2 and 1.3. The production cross sections predicted at next-to-leading order for these processes are $\sigma(p\bar{p} \to WW) = 11.66 \pm 0.70$ pb and $\sigma(p\bar{p} \to WZ) = 3.46 \pm 0.30$ pb [2].

Each of the two vector bosons can decay either leptonically ($W \to l\nu_l$, $Z \to ll$) or hadronically ($W \to qq'$, $Z \to q\bar{q}$). Here and in the following, l is taken to mean a

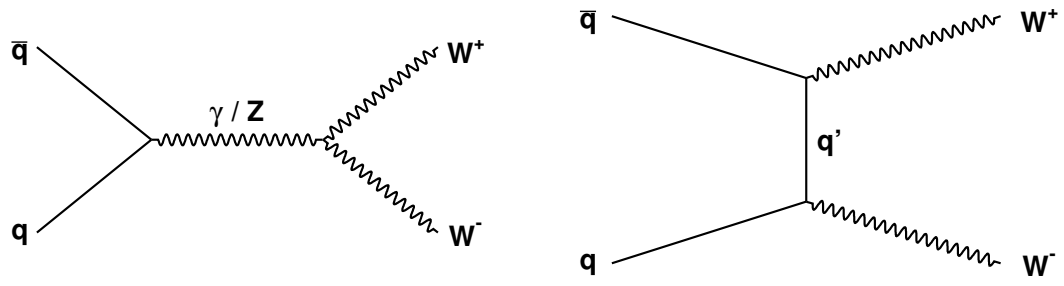

Figure 1.2: Leading-order s-channel (left) and t-channel (right) WW production diagrams.

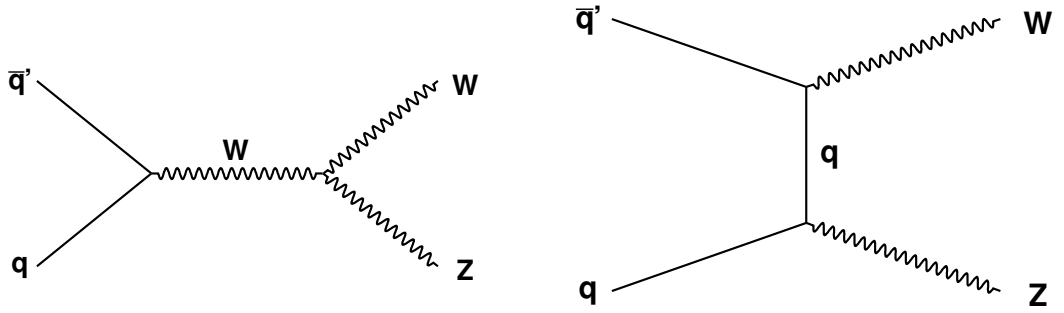

Figure 1.3: Leading-order s-channel (left) and t-channel (right) WZ production diagrams.

charged lepton. The "fully leptonic" final states are those in which both bosons decay leptonically, whereas in "semileptonic decays" one boson decays to leptons and the other to quarks. The branching ratio for the hadronic decays of W and Z is higher than for leptonic decays. Table 1.2 lists the branching ratios for several decay modes together with the cross sections of WW and WZ production [1, 2].

While the branching ratio for the semileptonic decay modes is higher than for the fully leptonic modes, the fully leptonic decays are less challenging to observe at a hadronic collider. Since they do not contain jets in their final state, the backgrounds are small. WW and WZ production have both been observed in their fully leptonic decay modes at

Process	Cross section (pb)	Decay mode	Branching ratio (%)
WW	11.66 ± 0.70	$l\nu l\nu$	10.5
		$l\nu qq$	43.8
WZ	3.46 ± 0.30	$l\nu ll$	3.3
		$l\nu\nu\nu$	6.5
		$l\nu qq$	22.6
		$qqll$	6.8
		$qq\nu\nu$	13.5

Table 1.2: Production cross sections and branching ratios for WW and WZ processes. Only leptonic and semileptonic channels are listed.

the Tevatron and their measured cross sections are in agreement with theoretical predictions [3, 4, 5, 6].

The semileptonic decay modes, on the other hand, suffer from large backgrounds due to W+jets and Z+jets production, which have large production cross sections. Nonetheless, diboson events in semileptonic modes have recently been observed. The first observation was achieved in a final state with two jets and large invisible energy [7]. In the channel with an identified lepton and jets, D0 saw evidence of diboson production [8] and CDF published an observation [9]. This thesis presents the details of the methodology used for the observation in the lepton plus jets channel at CDF, with some improvements and a larger data sample.

The lepton plus jets channel is sensitive to both $WW \to l\nu qq$ and $WZ \to l\nu qq$. The two quarks are observed in the detector as jets. Figure 1.4 shows the invariant mass reconstructed from the two jets for simulated WW and WZ events. The invariant mass distributions for the WW and WZ processes overlap because of the limited resolution for the jet energies. Because of this overlap, separating WW from WZ events is not feasible, and we measure the sum of their production cross sections. Note also that WW production is the dominant signal process. The cross section times branching ratio for

$WW \to l\nu qq$ is about five times that of $WZ \to l\nu qq$.

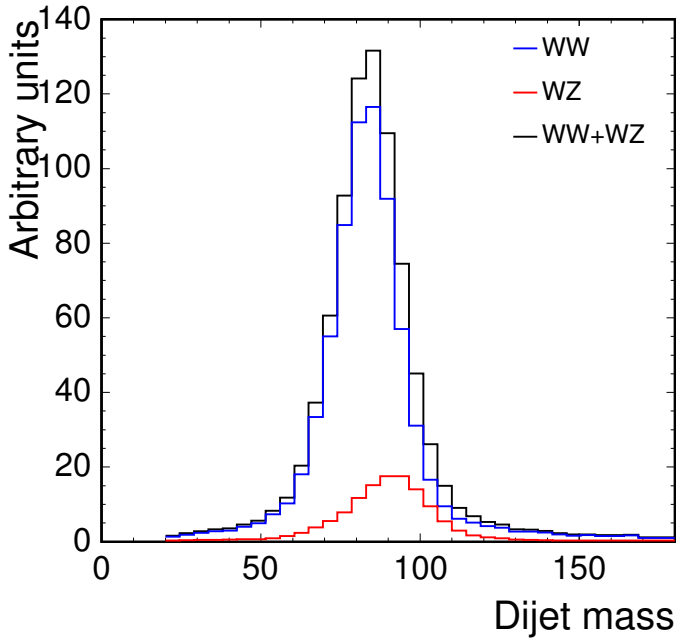

Figure 1.4: Invariant mass reconstructed from the two jets in WW and WZ events.

The WWZ coupling, present in the s-channel production of both WW and WZ, is sensitive to "new physics," or physics interactions that have not yet been observed experimentally. A common approach to WWZ and other triple gauge boson couplings (TGCs) is a model-independent effective theory. The new physics is assumed not to be directly observable, entering the theory instead as virtual contributions to the TGCs. Measurements of WW and WZ production at the Tevatron have been used to place limits on non-SM contributions to the TGC and both leptonic and hadronic channels have contributed to those limits. The measurement presented in this thesis has not yet been converted to a limit on new contributions to the TGCs, but could be used to do so in the future.

1.3 Context of measurement

The cross sections of various processes at the Tevatron are shown in Figure 1.5. The horizontal light blue lines indicate the predicted cross sections while the points mark the measured values. The production cross sections of processes measured at the Tevatron span several orders of magnitude. The lowest predicted cross sections shown on the plot correspond to production mechanisms of the Higgs boson. The limits are not at the predicted cross sections yet, but are continually improving.

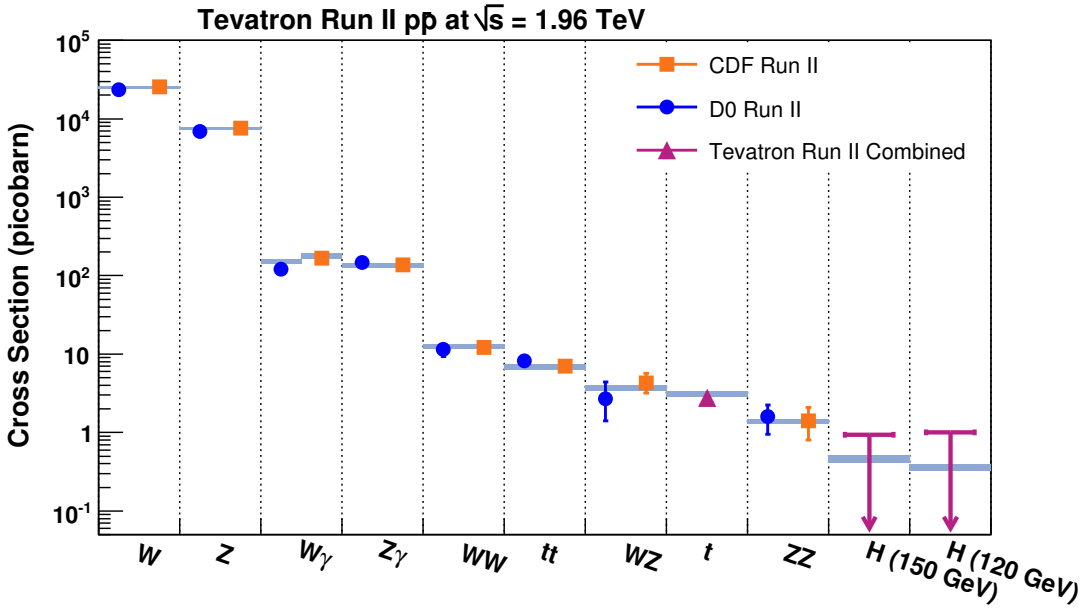

Figure 1.5: Production cross sections of several processes at the Tevatron.

The search for the Higgs boson is a subject of great interest in experimental particle physics. The LEP collider was able to exclude the existence of a Higgs boson with a mass $m_H < 114$ GeV/c^2 at the 95% confidence level. Indirect probes, based on measurements of electroweak observables like the masses of the W boson and top quark, find $m_H < 185$ GeV/c^2 at 95% confidence level. At the Tevatron, searches for the Higgs boson at masses

between these two bounds are taking place. In the spring of 2009, the Tevatron was able to exclude Higgs production at the 95% confidence level for Higgs bosons with masses between 160 and 170 GeV/c^2.

The most sensitive channels in the Tevatron Higgs search with $m_H < 135$ GeV/c^2 are when a Higgs boson is produced in association with a W or Z boson and the Higgs decays to a pair of b quarks ($WH \to l\nu b\bar{b}$, $ZH \to llb\bar{b}$, and $ZH \to \nu\nu b\bar{b}$). For $m_H > 135$ GeV/c^2, the most sensitive search channel is direct Higgs production, with the Higgs decaying to two W bosons ($H \to W^+W^-$).

Figure 1.6 compares the production cross section times branching ratio ($\sigma \times B.R.$) in several channels of interest for diboson physics and the Higgs boson search. In this figure and the following discussion, l represents an electron or muon. In the $l\nu jj$ channel used in this thesis, the $\sigma \times B.R.$ for $WW + WZ \to l\nu qq$ is significantly larger than for $WH \to l\nu b\bar{b}$, but is still an order of magnitude smaller than the dominant background, W+jets production. Another low cross-section process in this final state is single top quark production, which was recently observed at the Tevatron [10] [11].

The similarity between the final state topologies of $WW + WZ \to l\nu qq$, $WH \to l\nu b\bar{b}$, and single top quark production means that similar techniques can be used to isolate the signal in the three analyses. The implementation of the matrix element technique employed for the analysis in this thesis is related to the ones employed in the single top quark observation and being used in the Higgs search [10] [12]. But the $WW + WZ$ analysis also faces unique challenges: the absence of b quarks in the final state (which are expected in both single top and WH events) removes one useful tool in separating signals from backgrounds. Also, the mass of the dijet resonance from W/Z decay is lower than that expected from Higgs decay, making it more difficult to separate signal from background. Finally, the systematic uncertainties must be very well understood in

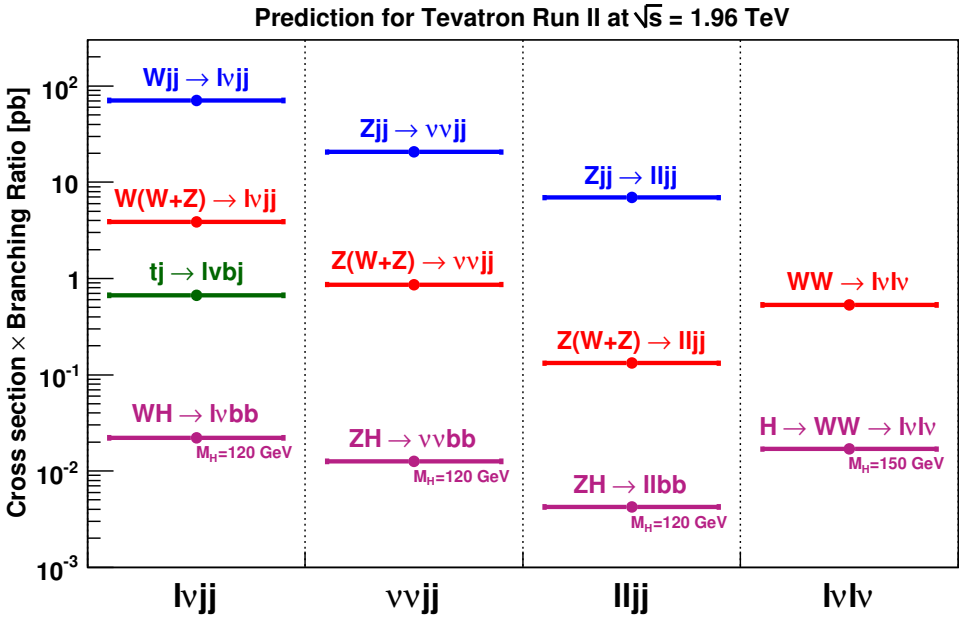

Figure 1.6: Cross section times branching ratio of signal and background in several important channels for the Higgs boson search at the Tevatron.

the $WW + WZ$ search, where a large number of signal events are expected, whereas in the Higgs search, the statistical uncertainty dominates the systematic uncertainty. As we approach observation of a signal in the Higgs search, however, the systematic uncertainties will become more significant, and the analysis of the systematic uncertainties in this thesis will be a useful reference.

CHAPTER 2

EXPERIMENTAL APPARATUS

The work described in this thesis is carried out using data from the Tevatron, a collider at the Fermi National Accelerator Laboratory outside of Chicago, Illinois [13]. The detector used to collect the data is the Collider Detector at Fermilab, or CDF [14]. Both the Tevatron and CDF are described in this chapter.

2.1 Tevatron

The Tevatron collides a proton (p) beam with an antiproton ($\bar{p}$) beam at a center-of-mass energy of 1.96 TeV. A sequence of accelerators is necessary to achieve two such high-energy beams. A schematic of the Tevatron accelerator complex is shown in Figure 2.1.

The process of creating a beam of protons begins with pure hydrogen gas. The hydrogen gas atoms are ionized in the pre-accelerator, and the negatively charged ions are brought to an energy of 750 keV by an electrostatic potential in a Cockroft-Walton dome. The ions enter a linear accelerator, the Linac, where they are further accelerated by a series of radio-frequency (RF) cavities to 400 MeV. As the beam enters the Booster at the end of the Linac, it passes through a sheet of copper which strips the electrons from the ions, leaving a beam of protons. The Booster is a circular accelerator with another series of RF cavities. After about 20000 revolutions in the Booster, the beam reaches an energy of 8 GeV.

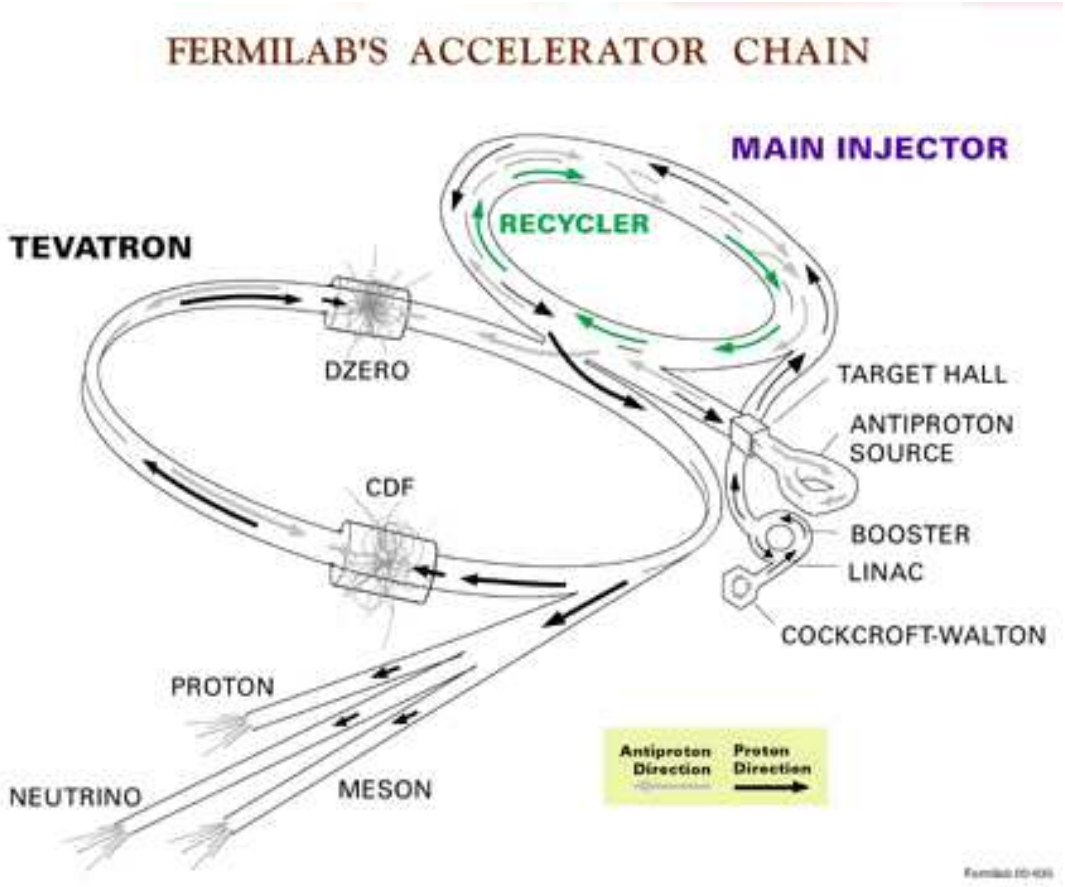

Figure 2.1: Schematic of the Tevatron accelerator complex.

The 8 GeV beam of protons enters the Main Injector, which serves several different functions. It accelerates the proton beam to either 150 GeV for injection into the Tevatron or 120 GeV for injection into the Antiproton Source. The Main Injector also receives antiprotons from the Antiproton Source and accelerates them to 150 GeV for injection into the Tevatron.

In the Antiproton Source, 120 GeV protons impinge on a nickel target. The collision between the protons and the nickel atoms creates secondary particles, including some antiprotons. A dipole magnet selects negatively charged particles with an energy around 8 GeV, creating a beam of antiprotons. The antiprotons enter the Debuncher, where

their momentum spread is reduced and the phase structure of the beam is removed. The de-bunched beam of 8 GeV antiprotons is sent to the Antiproton Storage Ring and then to the Recycler. When a sufficient number of antiprotons have been collected, they are injected into the Main Injector. The limiting factor for the Tevatron luminosity is the rate at which antiprotons can be produced. For roughly every 100,000 protons sent to the Antiproton Source, one antiproton is produced.

The Tevatron itself is a ring with a radius of about 1 km. The proton and antiproton beams travel in opposite directions in the same beam pipe. Each beam is composed of 36 bunches of particles, which are kept separated at key locations around the ring by electrostatic separators. The beams are injected at 150 GeV and are accelerated up to 980 GeV each, again by use of RF cavities. Dipole and quadrupole magnets with fields of up to 4.2 Tesla steer the beam around the ring. The beams cross at two collision points, producing $p\bar{p}$ collisions at 1.96 TeV. The 36 bunches stored in the Tevatron cross each other every 396 ns, or with a frequency of about 2.5 MHz.

When the proton beams collide, interactions occur between the partons within the proton, potentially producing other particles. The goal of a particle physics collider experiment is to learn about fundamental particles and their interactions by analyzing the outcome of these collisions. In order to do this, a detector is built around the interaction point of the two beams. The detector measures the energies, momenta, and angles of outgoing particles. There are two general-purpose detectors at the Tevatron, one at each beam crossing point: the D0 detector and the Collider Detector at Fermilab (CDF).

2.2 Collider Detector at Fermilab

CDF is a general-purpose collider detector, meaning it can be used to detect a variety of event signatures. Measurements involving leptons, photons, and jets of hadrons (and

combinations of these objects) have all been carried out at CDF. The detector has several layers, all of which serve a function in the detection of these particles.

Figure 2.2 is a schematic showing how particles interact in different regions of the detector. Closest to the beam pipe there is a tracking system which measures the bending radius of charged particles (like electrons, positrons, muons, and charged hadrons) in a magnetic field to find their momentum. Outside the tracking system there are two layers of calorimetry, referred to as electromagnetic and hadronic calorimeters. Photons, electrons, and positrons shower quickly and deposit much of their energy in the electromagnetic calorimeter. Hadronic particles usually shower later in the calorimeter and deposit a large fraction of their energy in the hadronic calorimeter. Muons generally do not interact strongly in the calorimeters, meaning they deposit only a small amount of energy there and are not stopped. As a result, additional detectors outside of the calorimeters are used in conjunction with the tracking system to identify and measure the momentum of muons.

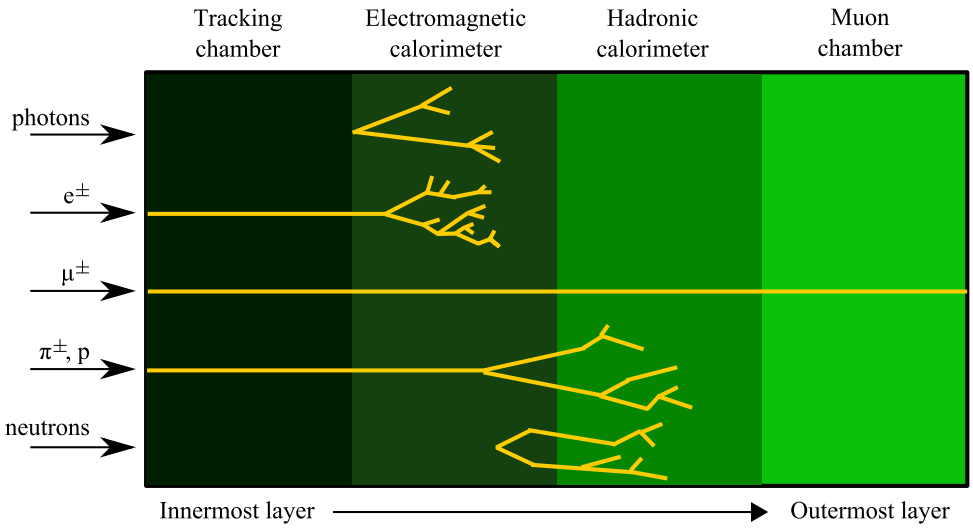

Figure 2.2: Representation of particle interactions in a detector.

The coordinate system at CDF is right-handed, with the z-axis pointing along the

proton beam, the x-axis pointing away from the center of the Tevatron ring, and the y-axis pointing up. Cylindrical coordinates are often used, with $r = \sqrt{x^2 + y^2}$, $\phi = \tan^{-1}\frac{y}{x}$, and $\theta = \cos^{-1}\frac{z}{r}$. The Lorentz-invariant rapidity, $y = \frac{1}{2}\ln\frac{E+p_z}{E-p_z}$, is often used instead of θ. In the limit where particles' energies are much higher than their masses (as is usually the case in a high-energy collider) the pseudo-rapidity $\eta = -\ln(\tan\frac{\theta}{2})$ is a good approximation for y.

A cutaway view of CDF is shown in Figure 2.3 and a schematic is shown in Figure 2.4. Details of the components of the detector are given below.

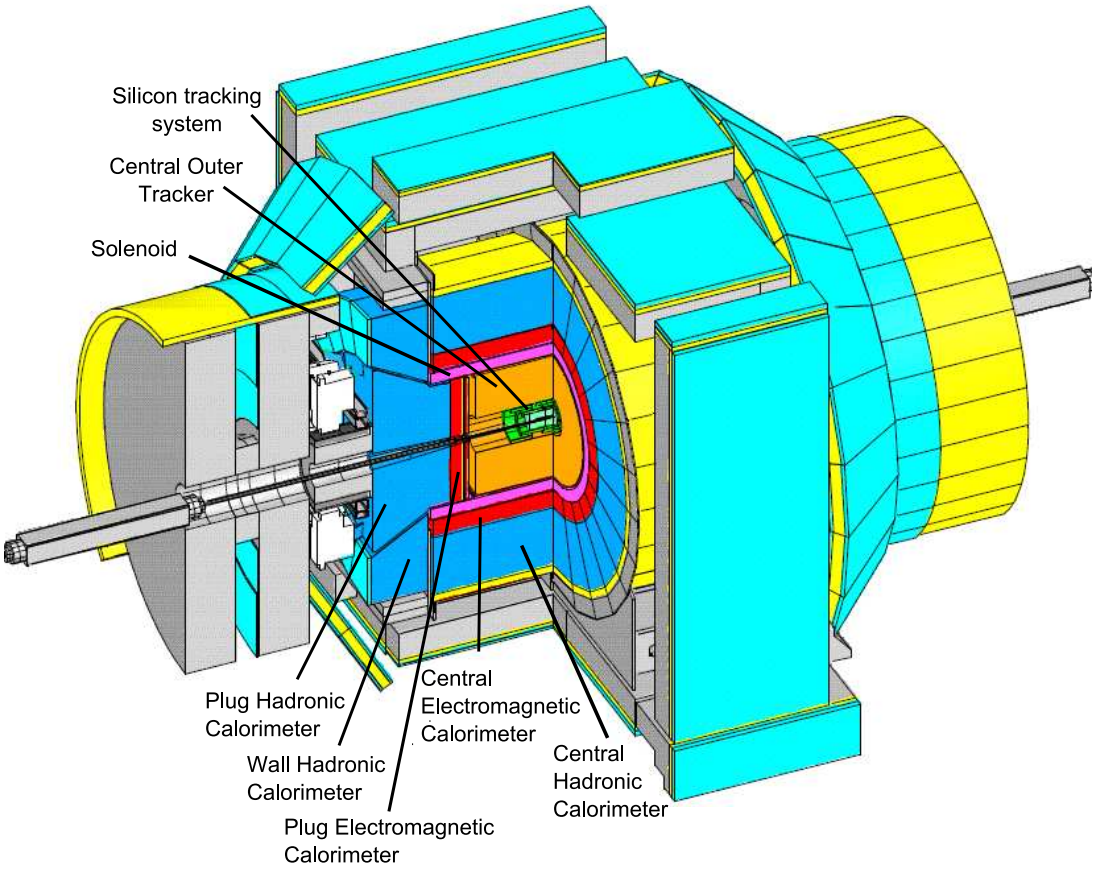

Figure 2.3: Cutaway view of the CDF II detector with tracking and calorimeter components labeled.

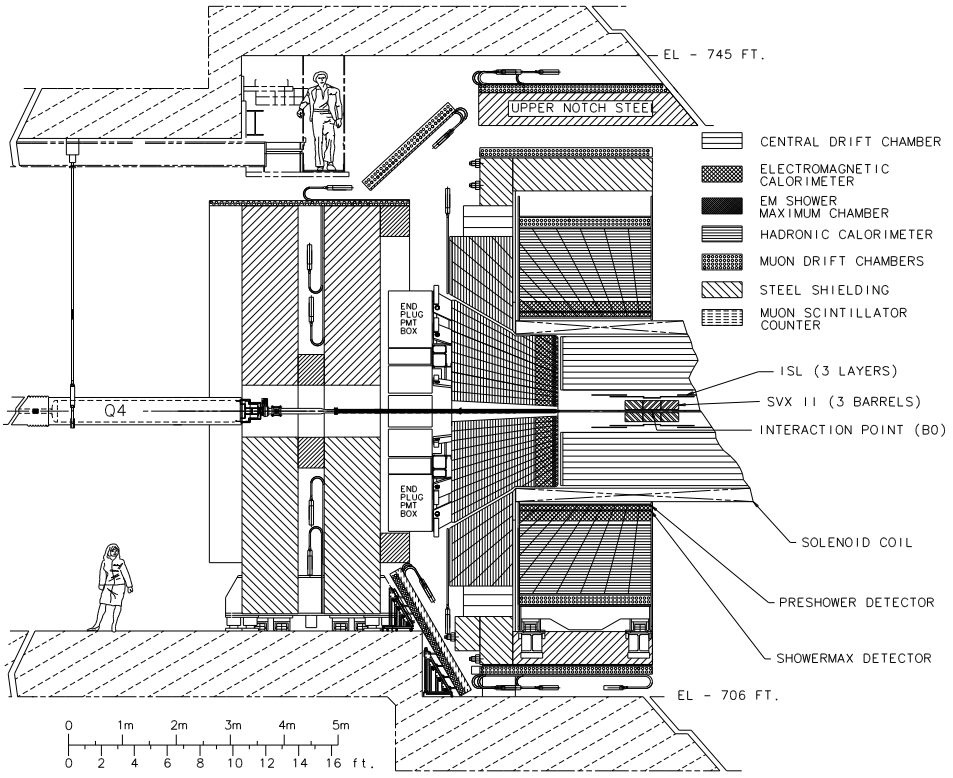

Figure 2.4: Schematic of the CDF detector.

2.2.1 Tracking system

The tracking system at CDF is composed of silicon strip detectors surrounded by a drift chamber, all enclosed in a solenoidal magnet applying a magnetic field of 1.4 Tesla. The CDF tracking system is shown in Figure 2.5.

Silicon tracking system

Silicon strips extend from right on the beam pipe (r = 1.5 cm) to r = 29 cm in seven layers. The innermost layer, Layer 00, has a special one-sided design because of the high levels of radiation it must endure. The next five layers are called the Silicon Vertex Detector (SVXII) system. Each layer of SVXII consists of double-sided silicon wafers.

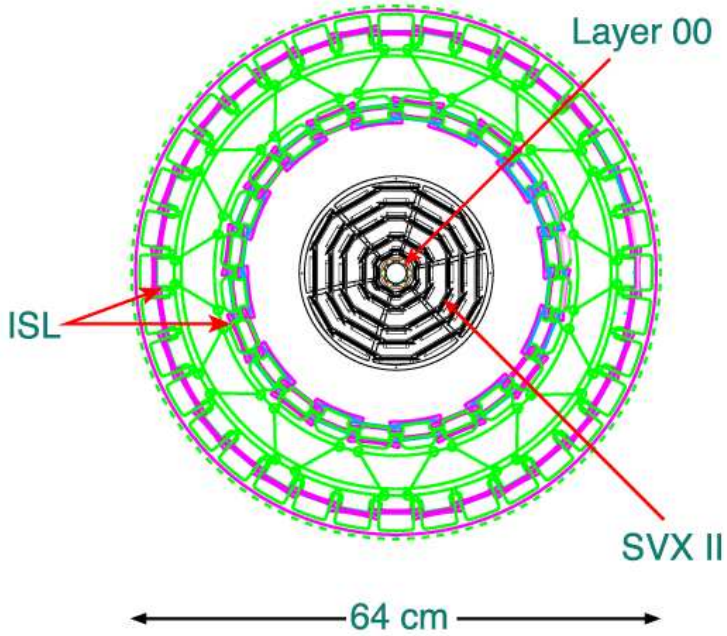

Figure 2.5: Transverse slice of the CDF tracking system.

The two sides are placed at a small stereo angle to each other, giving the capability of measuring track momenta in three dimensions. Finally, the Intermediate Silicon Layers (ISL) provide between one and two extra layers of silicon depending on η.

The coverage of the silicon extends to $|\eta| < 2$. It provides precise measurements of the vertex of a track. The resolution in the measurement of the impact parameter (the distance between a track's vertex and the beam line in the $r - \phi$ plane) is 40 μm, while the resolution of the measurement of z_0 (z position of a track's vertex) is 30 μm.

Central Outer Tracker

The Central Outer Tracker (COT) is a cylindrical drift chamber surrounding the silicon system. It covers the range from $40 < r < 137$ cm, giving a long distance over which to reconstruct a track's curvature and thus a charged particle's momentum. The COT extends to $|\eta| < 1.0$ and consists of 96 measurement layers, grouped into 8 alternating axial and

$\pm 2^\circ$ stereo superlayers. The mixture of argon and ethane gases used in the COT provides a relatively fast response, with a maximum drift time of 100-200 ns. The momentum resolution of a charged particle track in the COT is $\sigma(p_T)/{p_T}^2 = 0.0015$ $(\mathrm{GeV/c})^{-1}$.

2.2.2 Time of flight system

A time-of-flight (TOF) system sitting just outside the tracking system consists of scintillators read out by photomultiplier tubes. It measures the difference between the time of arrival of particles on the scintillator and the time of the beam interactions with a resolution of about 100 ps. It can be used for some particle discrimination, but in this analysis it is used to remove events due to cosmic rays, which are not expected to occur in time with beam collisions.

2.2.3 Calorimetry

All of the calorimeters on CDF are sampling calorimeters with scintillator tiles composing the active material. The electromagnetic calorimeters use lead as the absorber, whereas the hadronic calorimeters use steel. The readout is accomplished by wavelength shifting fibers, which carry the light from the scintillators to photomultiplier tubes. There are several separate components of the CDF calorimeter, which are labeled in Figure 2.3.

The central electromagnetic calorimeter (CEM) has a depth of 18 radiation lengths and extends to $|\eta| < 1.1$. Surrounding the CEM there is the central hadronic calorimeter (CHA) with a depth of 4.7 interaction lengths, and extending to $|\eta| < 0.9$. The wall hadronic calorimeter (WHA), with a similar design to the CHA, provides hadronic calorimetry in the region $0.8 < |\eta| < 1.2$. The central calorimeters are all segmented into towers with $\Delta\phi \times \Delta\eta$ of 0.26×0.1.

Plug calorimeters extend the η coverage of both electromagnetic and hadronic calorimetry to about $|\eta| < 3.6$. The same lead-scintillator (iron-scintillator) technologies are used for electromagnetic (hadronic) calorimetry in the plug region as in the central region.

Both central and plug electromagnetic calorimeters have a so-called shower maximum (ShowerMax) detector, a thin detector located about six radiation lengths into the electromagnetic calorimeter, where one expects (on average) the widest point of the electromagnetic shower. The ShowerMax detectors are composed of wire chambers to provide an axial position measurement and cathode strips for a stereo measurement. The fine segmentation in the ShowerMax detectors allows for a precise position measurement of electromagnetic clusters. This leads to better matching to tracks and improves the electron identification.

2.2.4 Muon system

Muons typically do not deposit much energy in the detector, behaving instead as minimum ionizing particles as they pass through the calorimeters. Outside the calorimeters, the muon system is used in conjunction with the inner detector tracking to reconstruct muon momentum. The muon system is composed of drift chambers with several layers (or stubs) which record hits as a muon passes through them.

The CDF muon system consists of four separate detectors, all with very similar technologies. The Central Muon Detector (CMU) is located directly outside the calorimeters and has six layers of drift chambers. Outside the CMU, 60 cm of iron provide shielding in front of the Central Muon Upgrade (CMP), another four layers of drift chambers. The shielding absorbs hadronic particles leaking from the calorimeter and reduces the number of fake muons. The CMU and CMP detect muons with $|\eta| < 0.6$ and p_T >1.4 GeV/c. The pseudo-rapidity coverage is extended to $|\eta| < 1.0$ by the Central Muon Extension

(CMX). Finally the Barrel Muon Detector (BMU), sits even farther forward, covering $1.0 < |\eta| < 1.5$. Both the CMX and BMU detectors have scintillator systems associated with them, which provide timing information that is useful for cosmic ray rejection.

2.2.5 Luminosity counters

The integrated luminosity, $\mathcal{L}$, is an important parameter in a cross section measurement, since the cross section $\sigma = N/\mathcal{L}$, where N is the number of events. Cherenkov Luminosity Counters (CLCs) are used to measure the instantaneous luminosity of the Tevatron at CDF; the integrated luminosity is calculated from the instantaneous luminosity measurements. The CLCs consist of gaseous Cherenkov counters located at high pseudo-rapidity, $3.6< |\eta| <4.6$. They measure the rate of inelastic collisions. Using the CLC acceptance derived from simulation and the total inelastic cross section of $p\bar{p}$ collisions, the instantaneous luminosity can be calculated with an accuracy of about 6%.

2.2.6 Triggers

Interactions occur in CDF at an approximate rate of 2.5 MHz. Storing full detector read-out information for all of these collisions would be impossible due to constraints on available storage space and the speed with which information can be written to disk. Only a small fraction of these events contain interactions that are of interest for modern physics. The three-level trigger system at CDF is responsible for picking out the interesting events. A schematic of the trigger system is shown in Figure 2.6.

The Level-1 trigger is a hardware trigger that uses simple objects in its decision. Some of the objects available at Level-1 are XFT (fast tracks built in the COT) and individual calorimeter towers. The rate is reduced to about 20 kHz at Level-1.

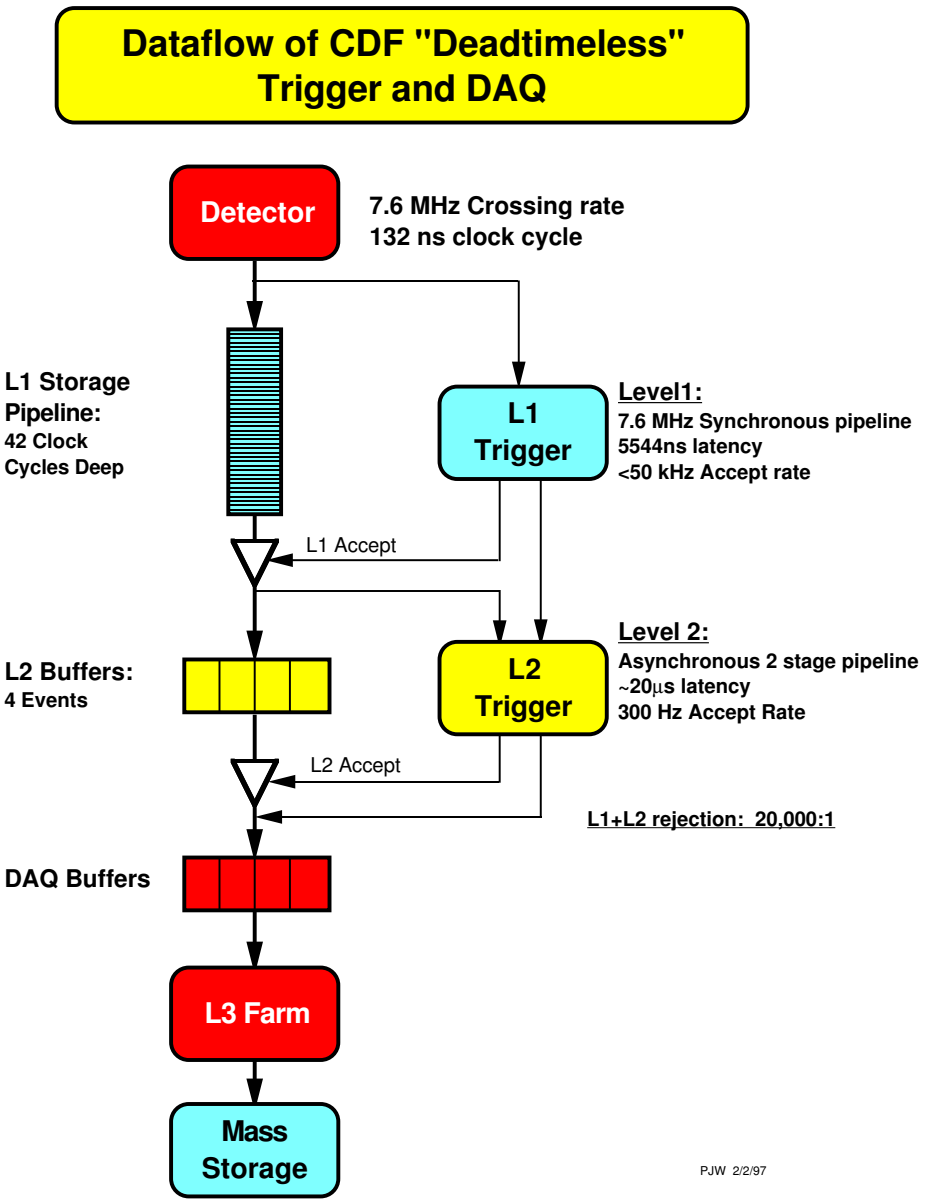

Figure 2.6: Schematic of the CDF trigger system.

The Level-2 trigger uses hardware to build somewhat more complicated objects, like displaced vertices or clusters of towers, sending this information to a processor that makes the decision about whether or not to accept the event. After Level-2, the event rate has been reduced to about 300 Hz.

Finally, the software Level-3 trigger performs a full event reconstruction. Complicated trigger chains are implemented at Level-3. The final rate of events is around 100 Hz. Events accepted at Level-3 are passed to the offline reconstruction code for use in physics analysis.

2.3 Data sample

The integrated luminosity delivered by the Tevatron during Run II is shown in Figure 2.7. Also shown is a curve representing the integrated luminosity recorded by CDF. The difference between the two curves is due to time when the detector is off while the beam is running (e.g. at the beginning of a store when beam losses could damage the detector). The rate at which data is delivered and collected has been steadily increasing over the last few years as the Tevatron achieves higher instantaneous luminosities, shown in Figure 2.8. In recent running, the peak luminosity of a store has routinely reached 3×10^{32} cm^{-2}sec^{-1}.

The events used for offline analysis are compared to a "good run" list, which ensures that the full detector was operating well when the events were taken. The analysis presented in this thesis uses a data sample corresponding to 4.6 fb^{-1} of integrated luminosity. This sample was collected through March, 2009.

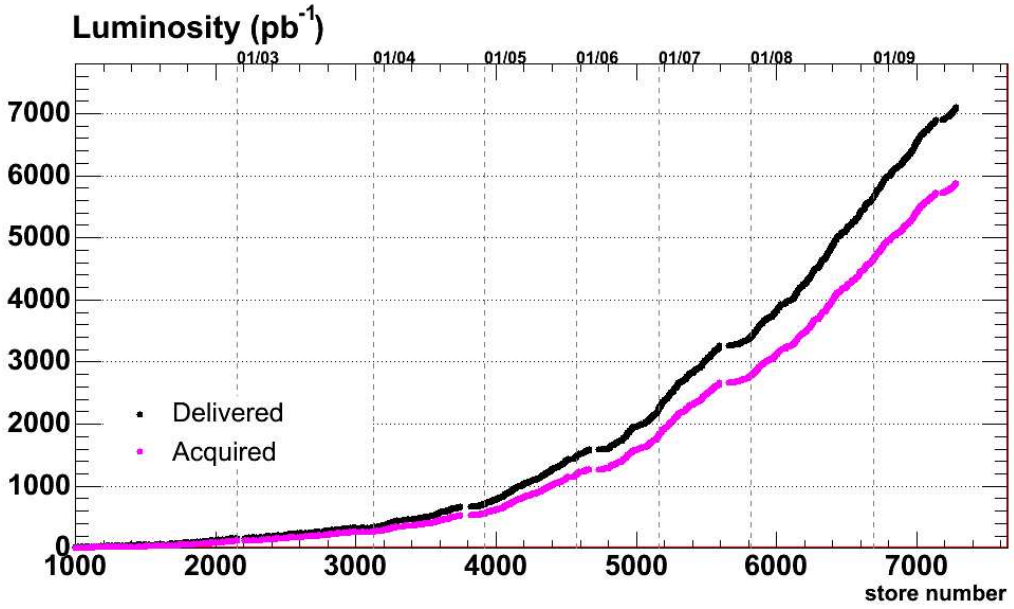

Figure 2.7: Integrated luminosity delivered by the Tevatron and acquired by CDF as a function of time up to July, 2009.

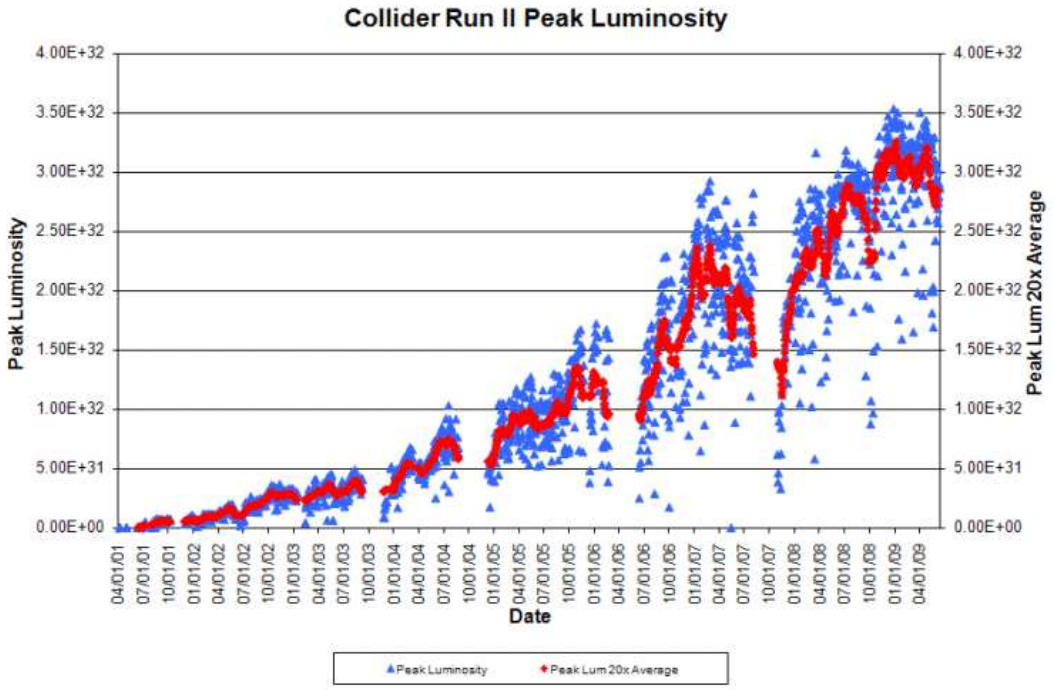

Figure 2.8: Peak instantaneous luminosity as a function of time at the Tevatron.

CHAPTER 3

EVENT SELECTION

The event selection chosen for this analysis is based on the topology of semi-leptonic WW and WZ decays, shown in Figure 3.1, which contains a charged lepton, a neutrino, and two quarks. The charged lepton is required to be an electron or muon, which can be identified with high purity in the detector. The neutrino escapes the detector without interaction, and so its presence must be indirectly inferred from the missing energy in the transverse plane ($\not\!\!E_T$). The two quarks quickly hadronize into clusters of hadronic particles, or jets; we require the presence of two jets in the event.

The details of the reconstruction and event selection requirements are given in this chapter. First the trigger paths used to select interesting events for the analysis are described in Section 3.1, followed by the details of the offline event selection in Section 3.2.

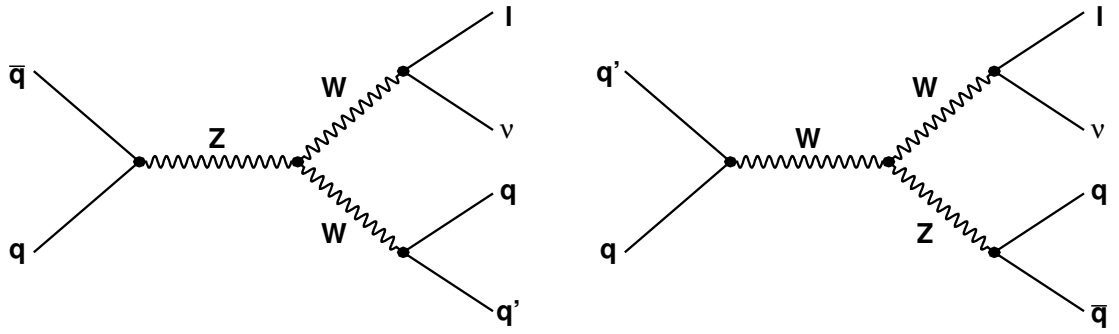

Figure 3.1: Feynman diagrams for WW and WZ production decaying to a lepton, neutrino, and two quarks.

3.1 Trigger paths

Events used in this analysis are collected by four trigger paths. Three of them take advantage of the presence of a high-p_T electron or muon, while the fourth triggers on two jets and $\not\!\!E_T$.

3.1.1 Central electron trigger

Roughly half of the events used in this analysis come from the central electron trigger path. These events are referred to CEM events.

At L1, CEM events are required to have a calorimeter trigger tower with E_T >8 GeV, a track in the COT with p_T >8 GeV/c, and E_{had}/E_{EM} (the ratio between energy deposited in the hadronic calorimeter and energy deposited in the electromagnetic calorimeter) less than 0.125. At L2, several calorimeter towers are grouped together to form a cluster which is required to have E_T >18 GeV. Finally, at L3, shower profile requirements are imposed.

The efficiency of the CEM trigger is evaluated from a sample of $W \rightarrow e\nu$ events collected by a different trigger requiring an electron and missing transverse energy. The CEM trigger is found to be about 96% efficient. In addition there is a small turn-on of the efficiency as a function of electron p_T. We raise the offline energy threshold for electrons to 20 GeV, where the effect of the turn-on is at the few percent level, small enough not to affect the analysis.

3.1.2 Central muon trigger

Events collected by the central muon trigger path are referred to as CMUP events.

At L1, the CMUP requires hits (or stubs) in both the CMU and CMP consistent with a muon of p_T >6 GeV/c and a matching track with p_T >4 GeV/c. At L2, the calorimeter

cluster corresponding to the stubs must have an energy consistent with that of a minimum ionizing particle, and the track p_T threshold is raised to 15 GeV/c. At L3, requirements are placed on the distance between a stub and the corresponding track extrapolated to the muon detectors.

In $Z \rightarrow \mu^+\mu^-$ events where one muon passes the trigger requirements, the second muon can be used to evaluate the trigger efficiency. The CMUP trigger is about 93% efficient. Similar to CEM events, the offline momentum threshold is raised to 20 GeV/c to avoid the effect of a trigger turn-on.

3.1.3 Central muon extension trigger

Events with muons in the pseudo-rapidity range $0.6 < |\eta| < 1.0$ can be collected by the CMX trigger. The requirements are very similar to the requirements for the CMUP trigger, and the efficiency is about 92%. However, in the CMX region there is no second shielded layer of drift tubes, so there is a higher probability of jets faking muons. To reduce the trigger rate to a level that can be handled by the DAQ system, the CMX trigger is prescaled, meaning a certain fraction of events passing the CMX trigger requirements are rejected.

3.1.4 $\not\!\!E_T$+ jets trigger

There are large gaps in the geometrical coverage of the CMUP and CMX triggers described above. An additional trigger path relying on two jets and large $\not\!\!E_T$ (referred to as the $\not\!\!E_T$+jets trigger) can fill in those gaps. Figure 3.2 shows the CMUP and CMX coverage in green and blue; the other colors show events with muons collected with the $\not\!\!E_T$+jets trigger. The muon events are selected from the data sample from this trigger offline.

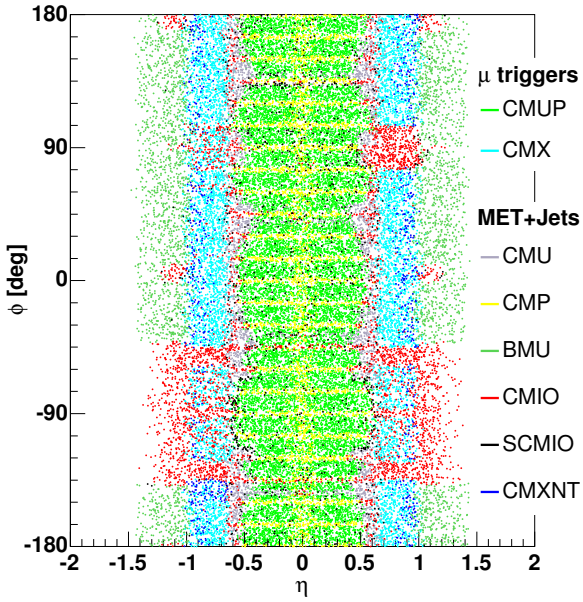

Figure 3.2: Coverage of the muon subdetector systems in η and ϕ.

At L1, events are required to have $\not\!\!E_T > 15$ GeV, where the $\not\!\!E_T$ is calculated based on calorimeter towers with $E_T > 1$ GeV. At L2, there must be a calorimeter cluster with E_T >10 GeV and two or more jets. The L3 requirement is $\not\!\!E_T$ >35 GeV. In fairly recent data with high instantaneous luminosity, the rate of events selected by the $\not\!\!E_T$+jets trigger grew too large for the DAQ, so an additional criterion that one jet be central was imposed.

Events passing this trigger are required to fulfill a few offline selection criteria so that the trigger is fully efficient at L2:

- the event must contain two jets, each with $E_T > 25$ GeV,
- one jet must be central, with $|\eta| < 0.9$, and
- the distance between the two jets in $\eta - \phi$ space ($\Delta R_{jj} = \sqrt{(\Delta\eta)^2 + (\Delta\phi)^2}$) must be greater than 1.0.

Trigger	Integrated luminosity (fb^{-1})
CEM	4.598
CMUP	4.588
CMX	4.532
$\not\!\!E_T$+jets	4.197

Table 3.1: Integrated luminosity corresponding to the data sample collected by each of the four triggers used.

The efficiency of the trigger as a function of the offline $\not\!\!E_T$ (which can differ from the trigger $\not\!\!E_T$ due to different calibrations and corrections) is studied using events from the CMUP trigger. The resulting turn-on curve in the efficiency is applied to Monte Carlo events so that their modeling of the trigger will match what is observed in data.

3.1.5 Integrated luminosity

Because of prescales and different times of implementation, the integrated luminosity of the data sample collected by the triggers can differ. Table 3.1 summarizes the integrated luminosity for each trigger type. The integrated luminosity of the data samples for the central lepton triggers are all similar, whereas the integrated luminosity for the $\not\!\!E_T$+jets trigger is somewhat lower because of prescales. We abbreviate the information in Table 3.1 by saying the integrated luminosity of the measurement is 4.6 fb^{-1}.

3.2 Offline event selection

3.2.1 Lepton selection

Events are required to contain one high quality electron or muon. The details of the electron and muon identification are given below.

Electron identification

Electrons are identified at CDF by finding a cluster of energy in the calorimeter that matches an isolated track in the inner detector. Various cuts are imposed to ensure that only well-measured electrons are taken into account. These cuts reduce fake electrons coming from detector noise, muons or hadrons from the collision, or non-collision particles (e.g. cosmic rays or beam halo particles). The following requirements were imposed:

- $E_T > 20$ GeV.
- Electron is fiducial in the CEM volume, within the region where the trigger is efficient.
- Isolation ≤ 0.1, where isolation is the ratio between the transverse energy deposited in a cone of size $\Delta R < 0.4$ around the lepton and the transverse energy of the lepton.
- $p_T^{trk} \geq 10$ GeV where p_T^{trk} is the p_T of the track matched to the electron.
- $E_{had}/E_{em} \leq 0.055 + 0.00045E$ where E_{had} is the energy deposited in the hadronic calorimeter, E_{em} is the energy deposited in the electromagnetic calorimeter, and E is the total energy of the electron. (An electromagnetically interacting particle like an electron is expected to deposit a large fraction of its energy in the electromagnetic calorimeter.)
- $L_{shr} \leq 0.2$, where L_{shr} is the lateral energy sharing, which quantifies the difference between the electron's lateral shower profile and that expected from the detector simulation and test beams.

- $E/p < 2$ if $E_T < 100$ GeV or $p_T^{trk} > 50$ GeV if $E_T \geq 100$ GeV, where E is the energy measured in the calorimeter and p is the momentum of the track matched with the electron.

- $|z_0| < 60$ cm where z_0 is the origin of the track, measured with respect to the center of the detector. (This cut ensures that the electron originated close to the nominal beam crossing point.)

- $|\Delta z| \leq 3$ cm where $|\Delta z|$ is the difference between the z-position of the calorimeter cluster and the z-position of the associated track.

- $-3.0 \leq Q \times \Delta x \leq 1.5$ cm where Q is the charge of the particle and Δx is the distance in the $r-\phi$ plane between the cluster and the track when it is extrapolated to the shower max.

- $\chi^2_{strip} \leq 10.0$, where χ^2_{strip} is the χ^2 between the observed and expected shower profile in the shower max.

- ≥ 3 good COT axial segments.

- ≥ 2 good COT stereo segments.

- There is no second track close to the electron's track which would be consistent with a photon converting to two charged electrons.

Muon identification

The different muon definitions are listed in Table 3.2. CMUP and CMX muons come from the corresponding trigger paths, while the other types of muons are collected by the $\not\!\!E_T$+jets trigger. The coverage in η and ϕ of the muon types is shown in Figure 3.2.

Trigger	Offline muon type	Definition
CMUP	CMUP	Stub in both CMU and CMP
CMX	CMX	Stub in CMX
$\not\!\!E_T$+jets	CMU	Stub in CMU but not in CMP
	CMP	Stub in CMP but not in CMU
	BMU	Hits in the BMU
	CMXNT	Stub in non-trigger region of CMX
	CMIO	Isolated track matched to calorimeter cluster
	SCMIO	Isolated track matched to non-fiducial stub

Table 3.2: Definitions of offline muon types.

The following requirements are imposed on all muons:

- $p_T > 20$ GeV/c.
- Isolation ≤ 0.1, where isolation is defined in the same way as for electrons.
- $E_{em} \leq \max(2, 2 + 0.0115(p - 100))$, where E_{em} is the energy deposited in the electromagnetic calorimeter and p is the muon momentum.
- $E_{had} \leq \max(6, 6 + 0.028(p - 100))$, where E_{had} is the energy deposited in the hadronic calorimeter. (This cut, together with the previous one, ensures that the muon looks like a minimum ionizing particle in the calorimeters, reducing the fake muons from hadronic punch-through.)
- $|z_0| \leq 60$ cm where z_0 is the origin of the track, and the distance is taken with respect to the center of the detector. (This cut ensures that the muon originated close to the nominal beam crossing point.)
- ≥ 3 good COT axial segments.
- ≥ 2 good COT stereo segments.

- $|d_0| \leq 0.2$ cm if there are no silicon hits, or $|d_0| \leq 0.02$ cm if there are silicon hits.

In addition there are some requirements dependent on the type of muon, summarized in Table 3.3. Many of these refer to a quantity Δx, which is the distance in the $r-\phi$ plane between the track extrapolated to the muon system and the stub in the muon system.

Muon type	Requirement
CMUP	Δx_{CMU} <7 cm, Δx_{CMP} <5 cm
CMX	Δx_{CMX} <6 cm
CMU	Δx_{CMU} <7 cm
CMP	Δx_{CMP} <5 cm
BMU	Δx_{BMU} <9 cm
CMXNT	Δx_{CMX} <6 cm
CMIO	$E_{EM} + E_{had} > 0.1$ GeV
SCMIO	$E_{EM} + E_{had} > 0.1$ GeV

Table 3.3: Muon event selection requirements dependent on the muon type.

3.2.2 Jet reconstruction

Final state quarks and gluons undergo parton showering and hadronization to form collimated jets. Jets are clustered using a seeded cone algorithm. The opening angle of the cone is taken to be $\Delta R = \sqrt{(\Delta\phi)^2 + (\Delta\eta)^2} < 0.4$. The algorithm searches for seed calorimeter towers with $E_T > 1$ GeV. Towers within a cone of $\Delta R = 0.4$ around the seed are added together, and a new E_T-weighted jet centroid is calculated. The process is iterated until the list of towers assigned to a jet is stable. If two jets overlap and share more than 50% of their energy, they are merged; if a tower is part of two different jets, it is assigned uniquely to the closer jet.

A jet is a complicated object, and a variety of corrections are needed to measure its energy. In particular, one needs to calibrate the relationship between the measured jet

transverse momentum (${p_T}^{jet}$), the transverse momentum of all particles within the jet cone corrected for instrumental effects (${p_T}^{particle}$), and the transverse momentum of the parton (quark or gluon) from which the jet originated (${p_T}^{parton}$) [15]. This relationship can be expressed as

$$\begin{aligned} {p_T}^{parton} &= {p_T}^{particle} - C_{UE} + C_{OOC}, \\ {p_T}^{particle} &= ({p_T}^{jet} \times C_\eta - C_{MI}) \times C_{ABS}, \end{aligned} \tag{3.1}$$

where the C's are various correction factors.

- C_{UE} is the extra energy in the jet cone due to the underlying event. This correction is derived from PYTHIA Monte Carlo events which are tuned to agree with minimum bias data from Run I of the Tevatron.

- C_{OOC} is the energy lost outside of the cone due to radiation. This correction is derived from PYTHIA Monte Carlo dijet samples.

- C_η is an η-dependent factor that ensures a uniform response across the whole calorimeter η range. This correction is derived separately for data and Monte Carlo using dijet events.

- C_{MI} is the energy deposited in the cone by additional $p\bar{p}$ interactions in the same bunch crossing. This correction is a function of the number of vertices in the event, and the average correction applied per vertex is derived from a minimum bias data sample.

- C_{ABS} is the calorimeter response function, correcting the raw calorimeter measurement to the momentum of the particle. This is the largest correction and is derived

from the detector simulation, whose response to hadronic particles is validated using test beams and collision data from a single track trigger.

We select events with two jets with the following requirements placed on jets:

- $E_T > 25$ GeV for the higher-E_T jet in the event, with E_T corrected to the particle level.
- $E_T > 20$ GeV for the lower-E_T jet in the event, with E_T corrected to the particle level.
- $|\eta| < 2.0$ for both jets in the event.

3.2.3 Missing transverse energy definition

The neutrino from the W boson decay escapes the detector without leaving any signal. Using conservation of momentum in the transverse plane, it is possible to reconstruct the missing transverse energy. It is defined as

$$\vec{\not\!\!E}_T = -\sum_i E_{Ti}\vec{n_i} \tag{3.2}$$

where i runs over the calorimeter towers, E_{Ti} is the $E_T = E\sin\theta$ in the ith tower, and $\vec{n_i}$ is the vector pointing from the interaction vertex to the center of the tower. The interaction vertex is reconstructed for each event using high-quality tracks in the COT. In events with a muon, the $\vec{p_T}$ of the muon is used in the summation, and the energy deposited by the muon in the calorimeter is subtracted from the tower energies used in the calculation. Similarly, for events with a jet, the corrected jet energy is used in the calculation. We define our cuts in terms of the scalar missing transverse energy, $\not\!\!E_T = |\vec{\not\!\!E}_T|$.

We require:

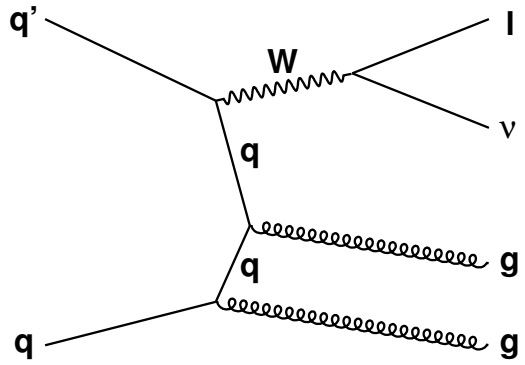

Figure 3.3: One of the contributing diagrams for a W boson produced in association with two gluons.

- $\not\!\!E_T$ >25 GeV for events with an electron and $\not\!\!E_T$ >20 GeV for events with a muon. (The higher $\not\!\!E_T$ threshold for electron events reduces the background due to QCD multi-jet events, as will be discussed in Section 4.1.4).

3.3 Backgrounds and event vetoes

By requiring two jets, $\not\!\!E_T$, and a lepton, we select events that look like our signal. But many background processes also have final state topologies similar to this signal. The contribution of these background processes can be reduced with event vetoes.

3.3.1 W+jets background and jet veto

The dominant background process is a W boson produced with accompanying jets (W+jets) with the W decaying leptonically ($W \to e\nu$ or $W \to \mu\nu$). An example diagram for a W boson produced in association with two gluons is shown in Figure 3.3. This background has a high production cross section, but looks very similar to our signal and cannot be reduced with simple event selection criteria.

Uncertainty in the modeling of the W+jets background results in significant systematic uncertainty in the measurement. One way of reducing this uncertainty is to veto events with additional jets. We remove events with a third jet with $E_T > 12$ GeV and $|\eta| < 2.0$.

3.3.2 Z+jets background and the Z boson veto

Z+jets events can enter our sample if the Z decays to an electron or muon pair and one of the leptons is not identified, leading to significant $\not\!\!E_T$.

The Z boson veto works by looking for a second lepton in the event that fulfills much looser electron and muon identification criteria than those described above for the first lepton in the event. For example, an isolated track is considered a loose lepton in the Z veto. If the second lepton has the opposite charge of the identified lepton in the event, and the invariant mass of the two leptons is close to the Z boson mass ($76 < M_{ll} < 106$ GeV/c^2), the event is rejected.

3.3.3 QCD multi-jet background and the QCD veto

QCD multi-jet events (also referred to as non-W events because they do not contain a real W boson) are produced with a very high cross section at the Tevatron. They can contain a real lepton from leptonic or semileptonic decay of heavy quarks; jets can also fake an electron or muon in the detector. QCD multi-jet events with either real or fake leptons form a background to our signal when mismeasurement of the jet energies leads to large $\not\!\!E_T$. Because this background is difficult to model (see Section 4.1), it is best to reduce it as much as possible with a veto specifically designed for the purpose. Jets fake electrons more often than they fake muons, so the veto is tighter for electron events.

One useful quantity is the transverse mass of the lepton-$\not\!\!E_T$ system, which is the transverse mass of the W in events with a real W. The transverse mass is defined as

$$m_T(W) = \sqrt{2(p_{Tl}p_{T\nu} - p_{xl}p_{x\nu} - p_{yl}p_{y\nu})}. \tag{3.3}$$

We require $m_T(W) > 10$ GeV for muon events and $m_T(W) > 20$ GeV for electron events.

Some additional cuts are imposed in electron events. A variable called the $\not\!\!E_T$ significance is defined:

$$\not\!\!E_T{}^{sig} = \frac{\not\!\!E_T}{\sqrt{\vec{E}_{Tunclustered} \cdot \hat{\not\!\!E}_T}}. \tag{3.4}$$

We require $\not\!\!E_T{}^{sig} > 0.05 m_T + 3.5$ and $\not\!\!E_T{}^{sig} > 2.5 - 3.125\Delta\phi_{\not\!\!E_T, jet2}$.

3.3.4 $t\bar{t}$ background and the dilepton veto

Top quark pair production can form a background for our signal when both top quarks decay leptonically and one lepton is not identified or when one top quark decays leptonically and the other hadronically and two jets are not identified.

We reduce the background due to fully leptonic $t\bar{t}$ decays by vetoing events with a second lepton. The second lepton is identified as any tight lepton as well as an electron in the plug calorimeter or a non-isolated lepton in the CEM, CMUP, or CMX.

The background from semileptonic $t\bar{t}$ decays will be strongly reduced by the veto on events with a third jet with $E_T > 12$ GeV mentioned earlier.

3.3.5 Small backgrounds

Single top quark production also leads to events with two jets, $\not\!\!E_T$, and a lepton. But the single top quark production cross section is significantly smaller than the production

cross section of our signal. We do not expect these events to form a large background.

ZZ events could also form a background if one of the Z bosons decays leptonically and one lepton is not identified. Again, the ZZ production cross section is small compared to that of our signal processes, and the Z veto will reduce the contribution from ZZ events further.

3.3.6 Cosmic rays and the cosmic ray veto

Muons from cosmic rays may pass muon identification criteria. The cosmic ray veto takes advantage of tracking and timing information. The tracking can be used to separate particles passing through the detector from top to bottom from particles originating in collision interactions with back-to-back tracks. Timing information from the TOF system (see Section 2.2.2) is also useful because cosmic ray events are usually not in time with collisions.

CHAPTER 4

MONTE CARLO MODELING

The analysis described in this thesis relies on accurate Monte Carlo modeling of signal and background processes. In particular, the kinematics of the processes affect the result of the matrix element calculations as well as the estimated efficiency of event selection criteria. In this chapter, the samples used for modeling events with an electron or muon, missing transverse energy, and two jets are described. The procedure to derive the event yield for each process and the comparison of the models with data are also presented.

4.1 Samples used for modeling

The signal processes and all background processes except for the QCD multi-jet background are modeled using events generated by a Monte Carlo program which are run through the CDF II detector simulation. The QCD multi-jet background is difficult to simulate, so it is modeled using data.

4.1.1 Monte Carlo programs

Table 4.1 shows the Monte Carlo event generators used for various background and signal processes.

PYTHIA is a leading-order event generator that uses a parton shower framework to simulate higher-order processes [16]. PYTHIA version 6.216 is used for the simulation of the WW and WZ signals.

Sample	Generator
WW	PYTHIA
WZ	PYTHIA
W+jets	ALPGEN + PYTHIA
Z+jets	ALPGEN + PYTHIA
$t\bar{t}$	PYTHIA
Single top	MADEVENT + PYTHIA

Table 4.1: Monte Carlo programs used to generate events for signal and background processes.

ALPGEN is a fixed-order parton level event generator [17]. To generate W/Z+jet events, it generates samples with $W/Z + n$ partons, where n ranges from 0 to 4. These samples are weighted by their relative cross sections and added together. The events generated by ALPGEN are passed to PYTHIA where the rest of the parton shower is simulated. An MLM matching framework removes double counting that arises from using both tree-level diagrams and a parton shower framework to simulate higher-order processes [18]. We use ALPGEN version 2.1′ interfaced with PYTHIA version 6.325 to simulate the W+jets and Z+jets backgrounds.

The single top background is generated using MADEVENT version 4 [19] interfaced with PYTHIA. The $t\bar{t}$ background is generated using PYTHIA version 6.216. The top mass is assumed to be 175 GeV/c^2 in the modeling of both of these backgrounds.

An important input to the event generators are the parton distribution functions (PDFs) of the incoming protons. These parameterize the longitudinal momenta of different types of quarks and gluons within the proton as a function of the momentum transfer of the collision. The CTEQ5L PDFs are used in generating all Monte Carlo samples in this analysis [20].

4.1.2 CDF II detector simulation

The CDF II detector simulation uses GEANT3 to simulate particle interactions with matter [21]. All of the major detector components are simulated and the simulation includes a detailed description of inactive material within the detector. The GEANT3 particle shower is parameterized at several points to reduce the computation time. The simulation is validated by comparison with well-understood processes in data, and generally the description is found to be very good [22]. A few aspects of the simulation are discussed here.

The charge deposition model for the silicon detectors uses a parameterized model based on GEANT3 and tuned to data. As a result, the simulation of the silicon detector reproduces well the size and spatial resolution of charged particle clusters.

In the central outer tracker, the GARFIELD package is used for the drift model [23]. The simulated track curvature agrees with data for muons in $W \rightarrow \mu\nu$ events.

Calorimeter showers are modeled using the GFLASH parameterization interfaced with GEANT3; use of this parameterization significantly decreases the computation time needed for the simulation [24]. The parameterized showers are initiated by a particle undergoing inelastic scattering in the calorimeter. The electromagnetic shower in GFLASH is tuned using electron test beam data, and the high energy hadronic shower characteristics are tuned using data from pion test beams. The low energy hadronic shower and lateral shower profiles are tuned with minimum bias data. The E/p distributions in data and Monte Carlo agree well for pions ranging in momentum from less than 1 GeV to several hundred GeV.

No parameterization is used in the muon system; the main challenge lies in describing its complicated geometry. $W \rightarrow \mu\nu$ and $Z \rightarrow \mu^+\mu^-$ events are used to validate the simulation's description of the geometry.

4.1.3 Modeling of the instantaneous luminosity

As pointed out in Section 2.1, the instantaneous luminosity in the Tevatron collider has been steadily increasing over time. Higher instantaneous luminosity generally means that there are more $p\bar{p}$ interactions per bunch crossing. This can lead to a higher contribution from the underlying event and affect various aspects of the reconstruction.

Different instantaneous luminosities can be simulated in the Monte Carlo by tuning the number of additional interactions per bunch crossing. The samples used in this analysis were generated with two different luminosity profiles. The WW, WZ, and W+jets samples have a profile based on the first 2.7 fb^{-1} of data recorded, while the other samples were generated with a profile corresponding to about the first 1.0 fb^{-1} of data. Since we are using a 4.6 fb^{-1} data sample, and most of the additional data had high instantaneous luminosities, we expect the average simulated instantaneous luminosity to be lower than in our data sample.

One measure of the instantaneous luminosity is the number of reconstructed vertices. This quantity is shown in a stack plot for data and Monte Carlo in Figure 4.1 (left). As expected, the data and Monte Carlo do not agree.

We deal with this disagreement by reweighting the Monte Carlo events. The weights are given by the ratio between the two histograms in Figure 4.1 (left). The weight of a Monte Carlo event is then chosen according to the number of vertices in the event. Figure 4.1 (right) shows the reweighted comparison of the number of vertices in data and Monte Carlo.

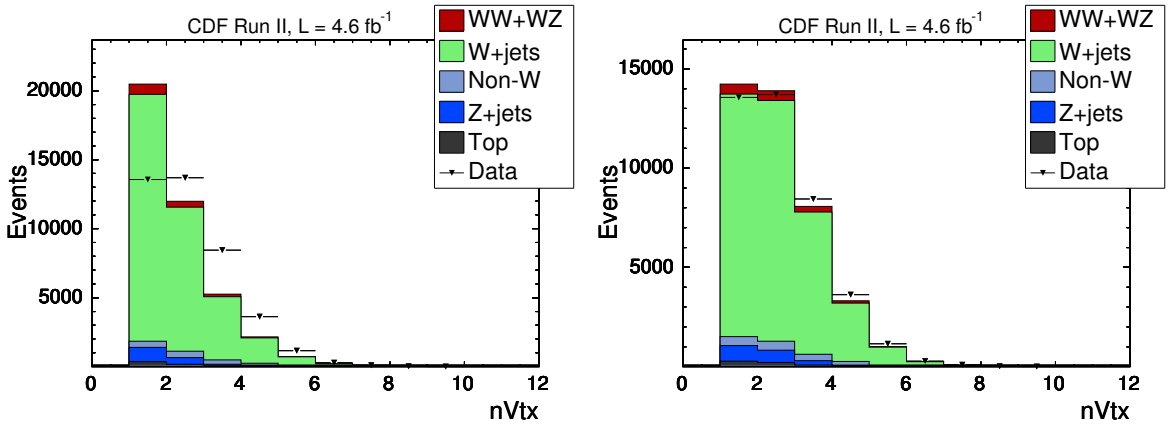

Figure 4.1: Distribution of the number of vertices in data and Monte Carlo before reweighting (left) and after reweighting (right).

4.1.4 QCD multi-jet background

QCD multi-jet events form a background for this channel when one jet in the event fakes an electron or muon and mismeasurement of the jet energies leads to large missing transverse energy[1]. The probability for a jet to fake an electron is higher than the probability for a jet to fake a muon. The QCD multi-jet background is small relative to the dominant W+jets background, but larger than the signal in electron events and roughly as large as the signal in muon events. It is therefore important to model its kinematics.

Simulating the QCD background is difficult. First, since the rate for a jet to fake an electron or muon is quite low, one would have to generate large QCD samples in order to have sufficient events passing the event selection. Second, mismeasurement of jet energies leading to large missing transverse energy is often due to instrumental effects that aren't accurately reproduced in the detector simulation. Because of these factors, data is used to model the QCD multi-jet background.

1. QCD multi-jet events can also contain real leptons from the decay of heavy flavor quarks, but the background from fake leptons is larger.

Three types of data are used for the QCD multi-jet background model, called jet electrons, anti-electrons, and non-isolated muons.

- Jet electrons are events that pass a 20 GeV jet trigger where one jet resembles an electron ($E_T > 20$ GeV and between 80% and 95% of its energy deposited in the electromagnetic calorimeter). The jet is also required to have at least four tracks, effectively removing events that may have a real electron.

- Anti-electron events come from the central electron trigger. They must fulfill the same kinematic requirements as tight electrons, but must fail at least two of five cuts related to shower shapes. The five cuts chosen are the cuts on E_{had}/E_{em}, L_{shr}, Δz, $Q \times \Delta x$, and χ^2_{strip} described in Section 3.2.1.

- Non-isolated muons pass the central muon trigger and contain a muon passing all identification requirements except the isolation requirement.

The anti-electron and jet-electron samples are small but provide a better kinematic description of the QCD multi-jet background than the larger non-isolated muons. In fact, even though the samples are based on jets faking electrons, they also provide a good kinematic description of muon events. As a result we use these events in both electron and muon channels. In the muon channels they are added to the non-isolated sample. In events with electrons, the total size of the samples used to model the non-W background is small.

4.2 Background normalization estimate

For the signal and all backgrounds except for W+jets and QCD non-W, the expected number of events is calculated based on the cross section of the process and the Monte

Carlo determination of the detector acceptance. Table 4.2 lists the assumed cross sections. The diboson cross sections are taken from the NLO calculations with MCFM [2]. For the Z+jets background, the CDF inclusive $Z \to l^+l^-$ cross section measurement is used [25]. Predictions based on NLO calculations are also used for the $t\bar{t}$ and single top backgrounds [26] [27].

Process	$\sigma \times B.R.$ (pb)
WW inclusive	11.66 ± 0.70
WZ inclusive	3.46 ± 0.30
ZZ inclusive	1.51 ± 0.20
Z+jets, $Z \to e, \mu, \tau$	787 ± 85
$t\bar{t}$, inclusive	6.70 ± 0.83
single top, inclusive	2.86 ± 0.36

Table 4.2: Cross section times branching ratio of signal and background processes used to estimate event yields.

Estimation of the QCD multi-jet background normalization requires a data-driven technique. We use the fact that the $\not\!\!E_T$ spectrum for non-W events looks different than that of the other backgrounds, which contain real W bosons. So by fitting the $\not\!\!E_T$ spectrum (before applying the $\not\!\!E_T$ cut of our event selection) in data to a sum of the background $\not\!\!E_T$ shapes, we can derive an expected non-W normalization. In this fit, the Z+jets, $t\bar{t}$, and single top backgrounds are constrained within fairly small uncertainties to the normalizations derived from their cross sections. The normalizations of the non-W and W+jets events are free parameters.

Figure 4.2 shows the fit to the $\not\!\!E_T$ for four lepton categories (CEM electrons, CMUP muons, CMX muons, and extended muons). The fits are generally quite good. The arrows indicate the $\not\!\!E_T$ cut applied in the analysis, and the f_{QCD} value is the percentage of QCD expected after applying the $\not\!\!E_T$ cut. The QCD contribution is expected to be roughly twice as large in electron events as in muon events.

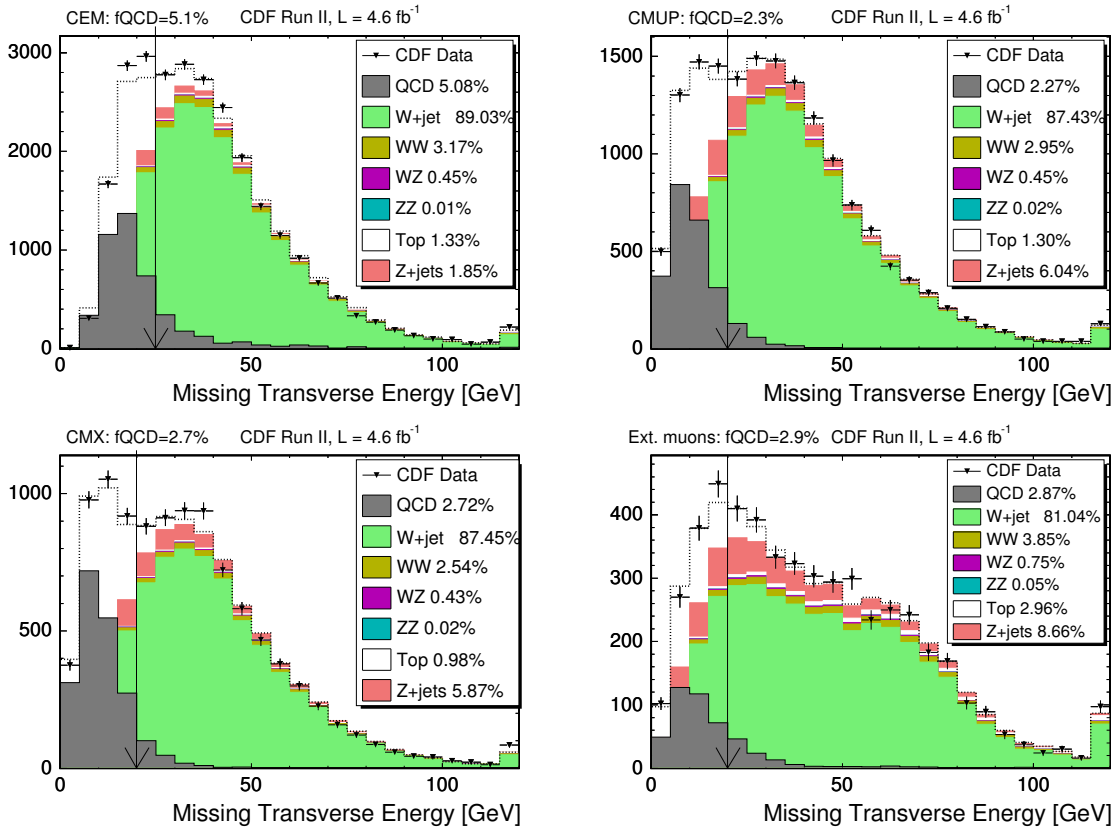

Figure 4.2: Fits to the $\not\!\!E_T$ distribution to determine the normalization of the QCD multi-jet background in the CEM, CMUP, CMX, and extended muon categories. The vertical arrow indicates the minimum $\not\!\!E_T$ required in the analysis.

A preliminary data-driven W+jets normalization is also derived from the fit to the $\not\!\!E_T$. This normalization is used in the modeling validation described in the next section. In the final fit to extract the diboson cross section, the W+jets normalization is a free parameter.

The expected event yields for all processes are shown in Table 4.3. The table has been divided into three lepton categories, which are the categories used in the final signal extraction fit. The CMUP and CMX muons are combined into one category since the kinematics and signal-to-background ratios are quite similar. The observed number of events in each category is also given. The observed and total predicted event yields

match well since the prediction is derived from a fit to the data.

Process	CEM	CMUP+CMX	Extended muons
WW	591 ± 50	523 ± 51	148 ± 13
WZ	84 ± 9	83 ± 10	29 ± 3
W+jets	16708 ± 394	15774 ± 260	3155 ± 70
Non-W	959 ± 384	443 ± 177	112 ± 45
Z+jets	304 ± 38	1071 ± 144	325 ± 41
$t\bar{t}$	120 ± 17	109 ± 16	64 ± 9
Single top	121 ± 18	108 ± 16	47 ± 7
ZZ	1 ± 0.2	4 ± 0.7	2 ± 0.3
Data	18888	18115	3881

Table 4.3: Expected number of events for each signal and background process in three lepton categories.

4.3 Modeling validation

Once the background levels are predicted, we want to investigate the agreement between data and Monte Carlo of various kinematic distributions. Figures 4.3 to 4.14 show the predicted and observed shapes of several variables. The relative contributions of the backgrounds are taken from Table 4.3, but the sum of the Monte Carlo contributions is normalized to the total number of data events. Thus the plots are shape comparisons only.

The four histograms plotted for each variable show the modeling in the three lepton categories separately and summed over all categories.

We focus on fairly simple kinematic quantities that will become relevant in the matrix element calculation: the energies and angles of the jets and leptons. The $\not\!\!E_T$ and transverse mass of the lepton-$\not\!\!E_T$ system are not used in the matrix element calculation, but validate that we understand our non-W model. Finally, we check the kinematics of the dijet system in order to validate the modeling of the correlations between

the two jets. We consider the angles between the two jets, $\Delta\phi = |\phi(jet1) - \phi(jet2)|$, $\Delta R_{jj} = \sqrt{(\eta(jet1) - \eta(jet2))^2 + (\phi(jet1) - \phi(jet2))^2}$, the invariant mass of the two jets, $M_{jj} = \sqrt{(E(jet1) + E(jet2))^2 - (\vec{p}(jet1) + \vec{p}(jet2))^2}$, and the p_T of the dijet system.

Overall the modeling is in good agreement with data. The fact that the lepton p_T (Figure 4.7), the $\not\!\!E_T$ (Figure 4.9), and the transverse mass of the leptonic W (Figure 4.10) are well-modeled gives us confidence in our QCD non-W modeling. Variables related to the jets, however, are not as well modeled. In particular there is some mismodeling of the first and second jet E_T (Figures 4.3 and 4.5), the η of the second jet (Figure 4.6), and in the kinematics of the dijet system (Figures 4.11 to 4.14). Systematic uncertainties on the shape of the W+jets background cover the observed mismodeling; this is discussed further in Chapter 7.

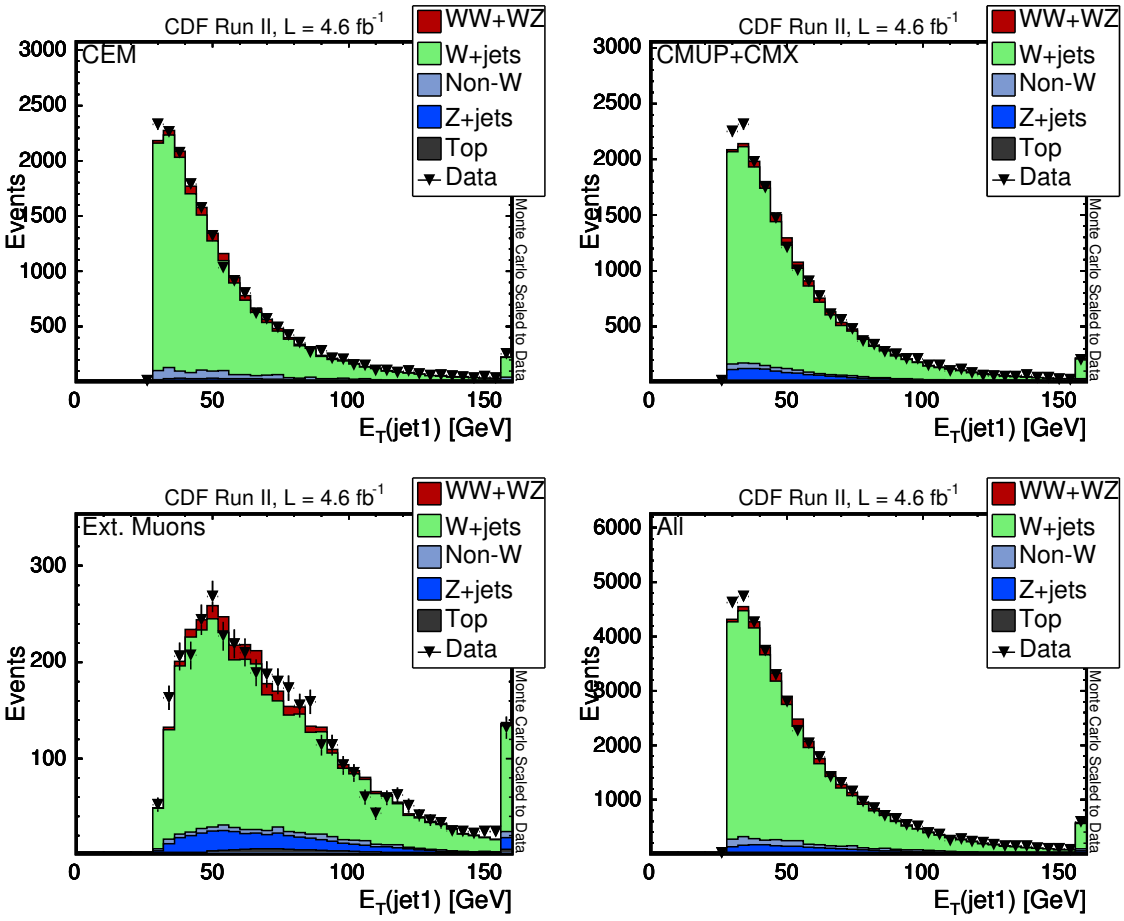

Figure 4.3: Comparison between the jet E_T distribution observed in data and the predicted model for the higher-E_T jet.

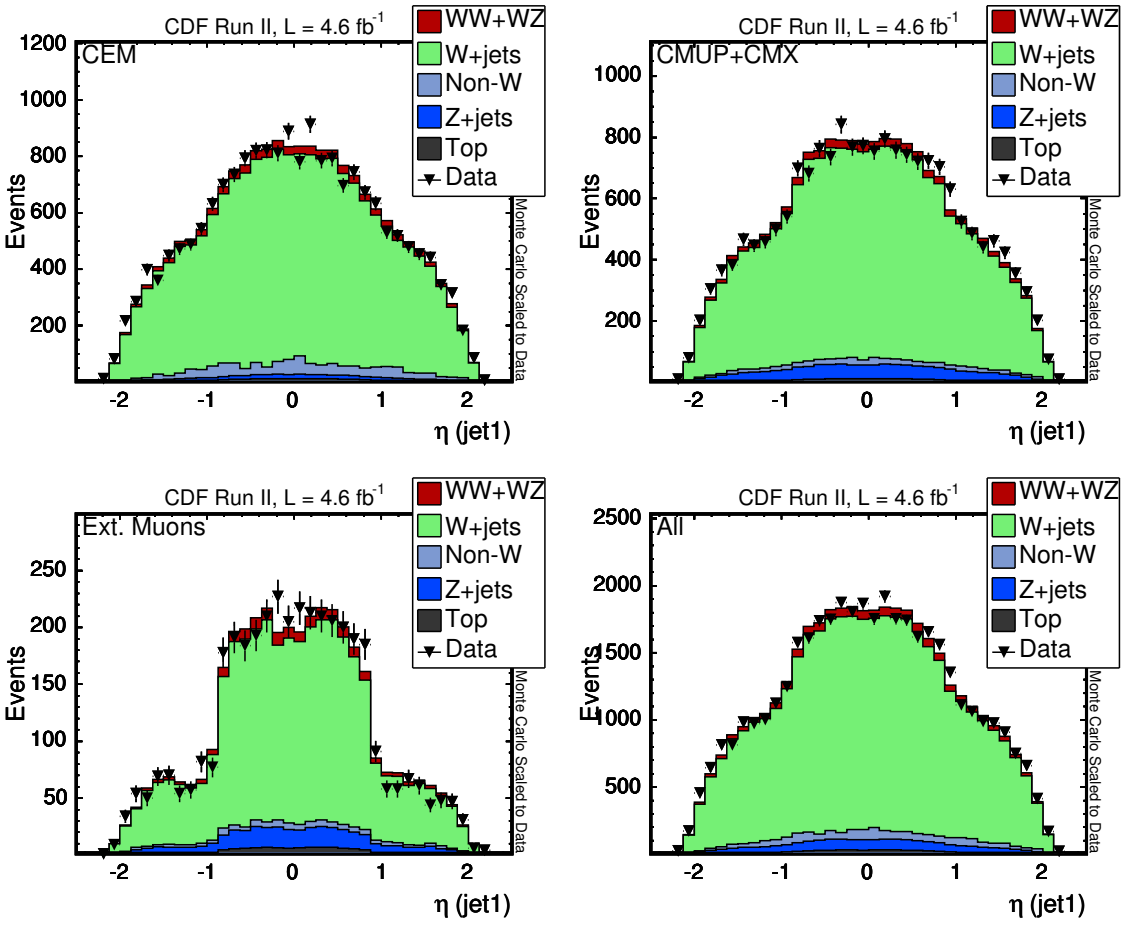

Figure 4.4: Comparison between the jet η distribution observed in data and the predicted model for the higher-E_T jet.

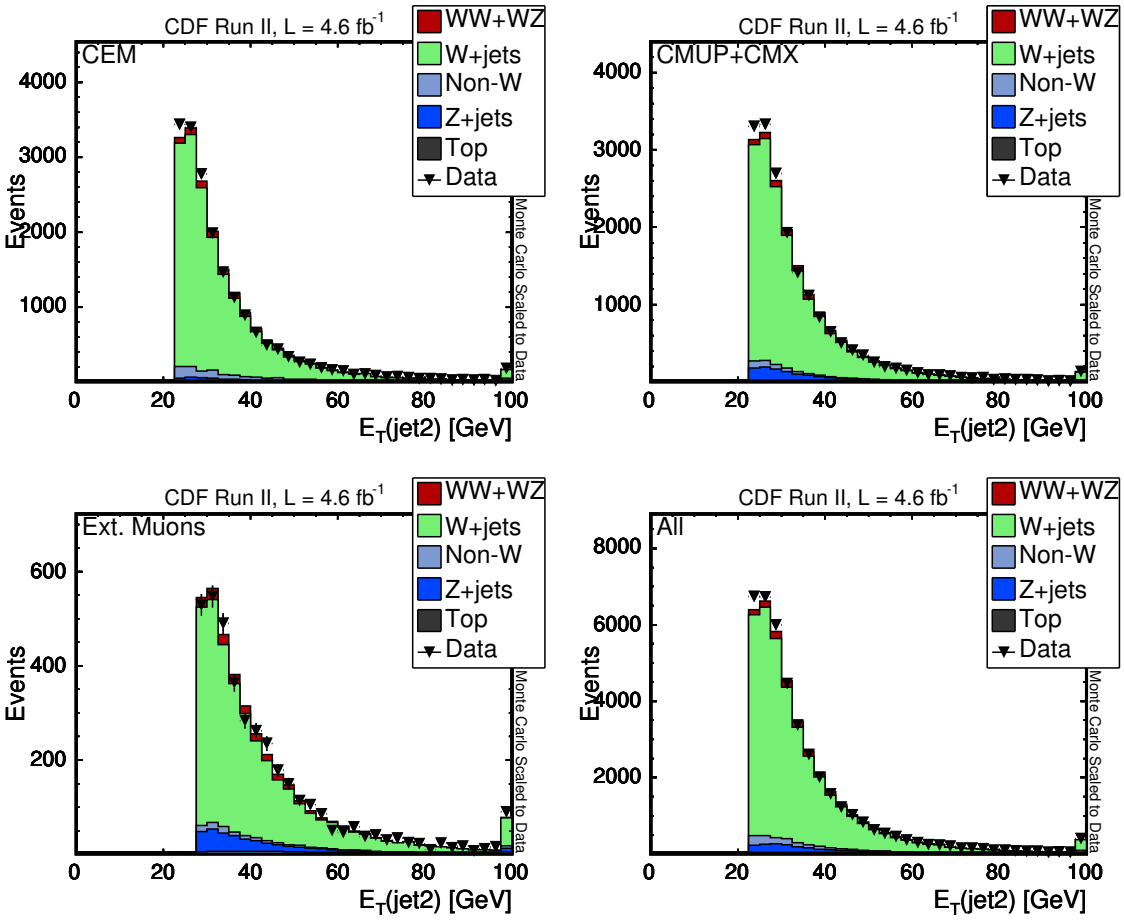

Figure 4.5: Comparison between the jet E_T distribution observed in data and the predicted model for the lower-E_T jet.

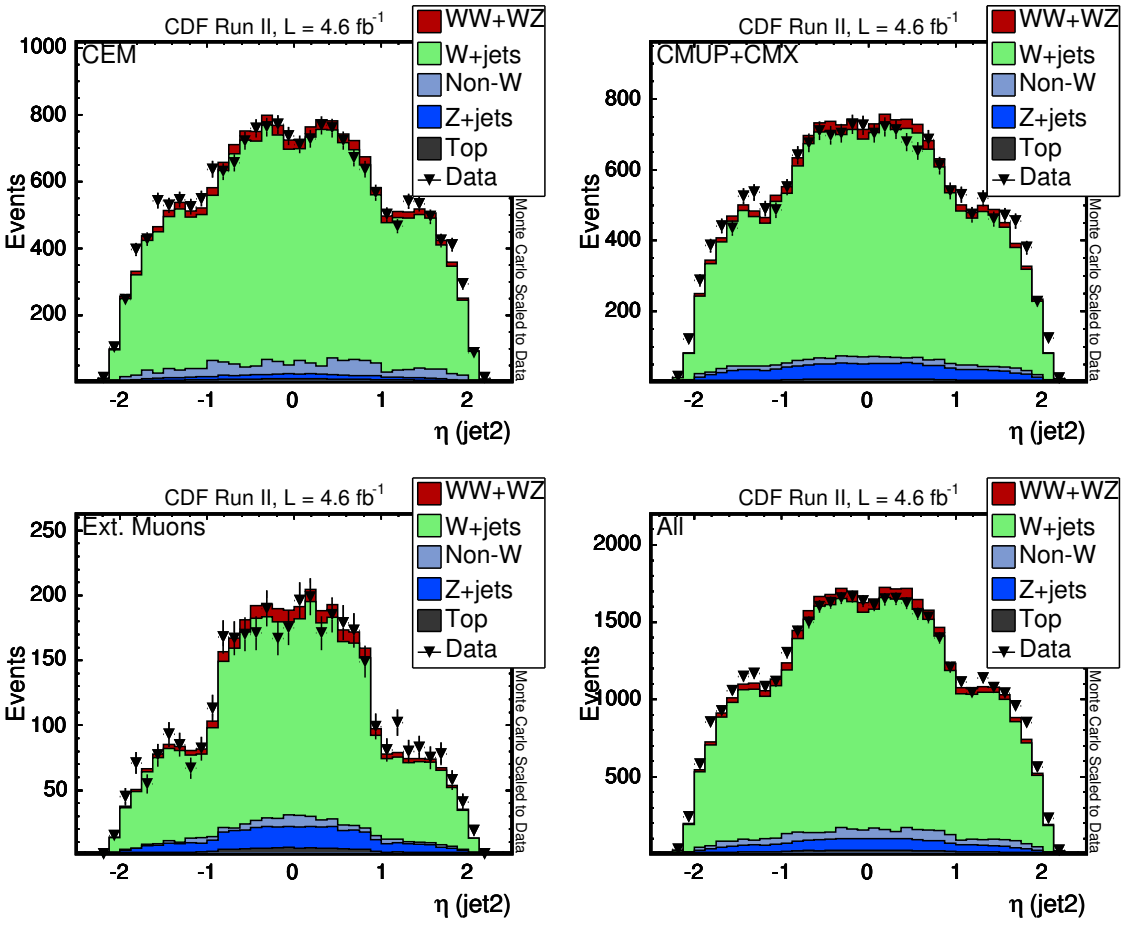

Figure 4.6: Comparison between the jet η distribution observed in data and the predicted model for the lower-E_T jet.

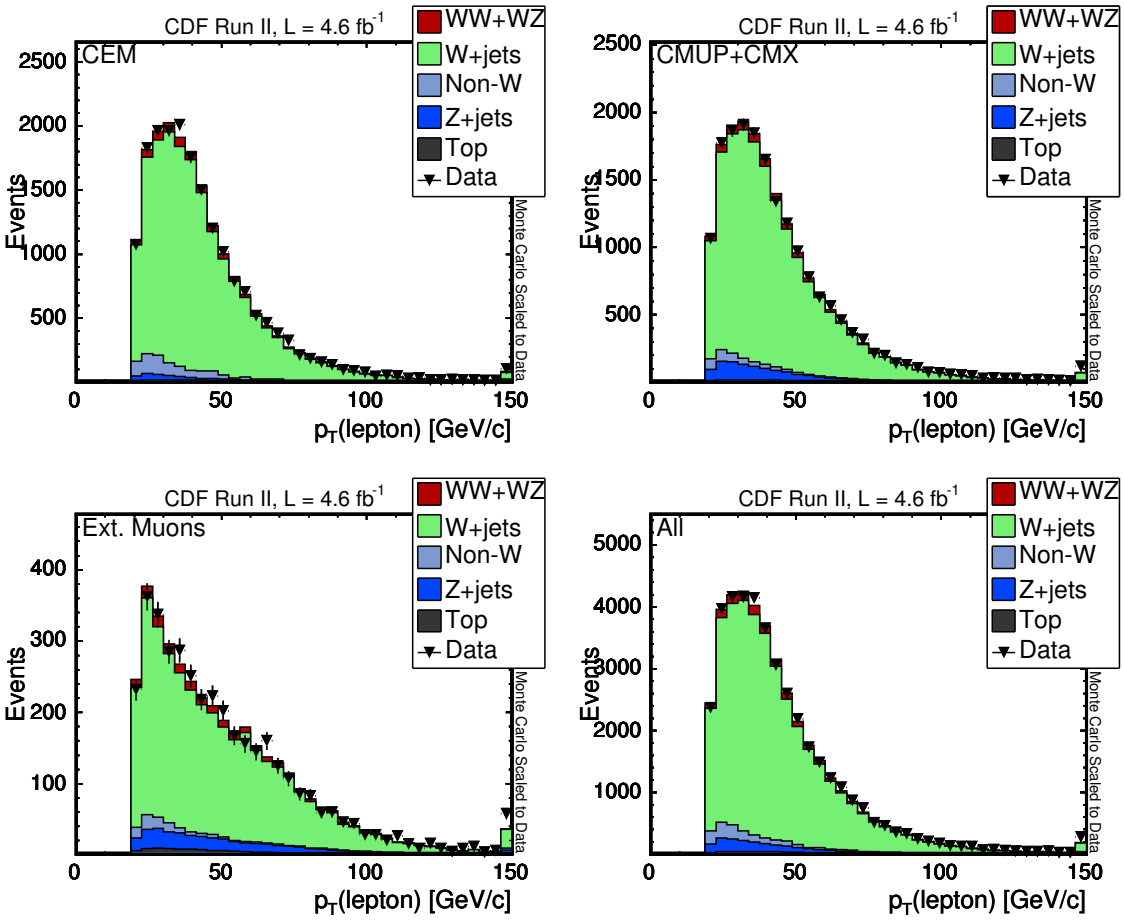

Figure 4.7: Comparison between the lepton p_T distribution observed in data and the predicted model.

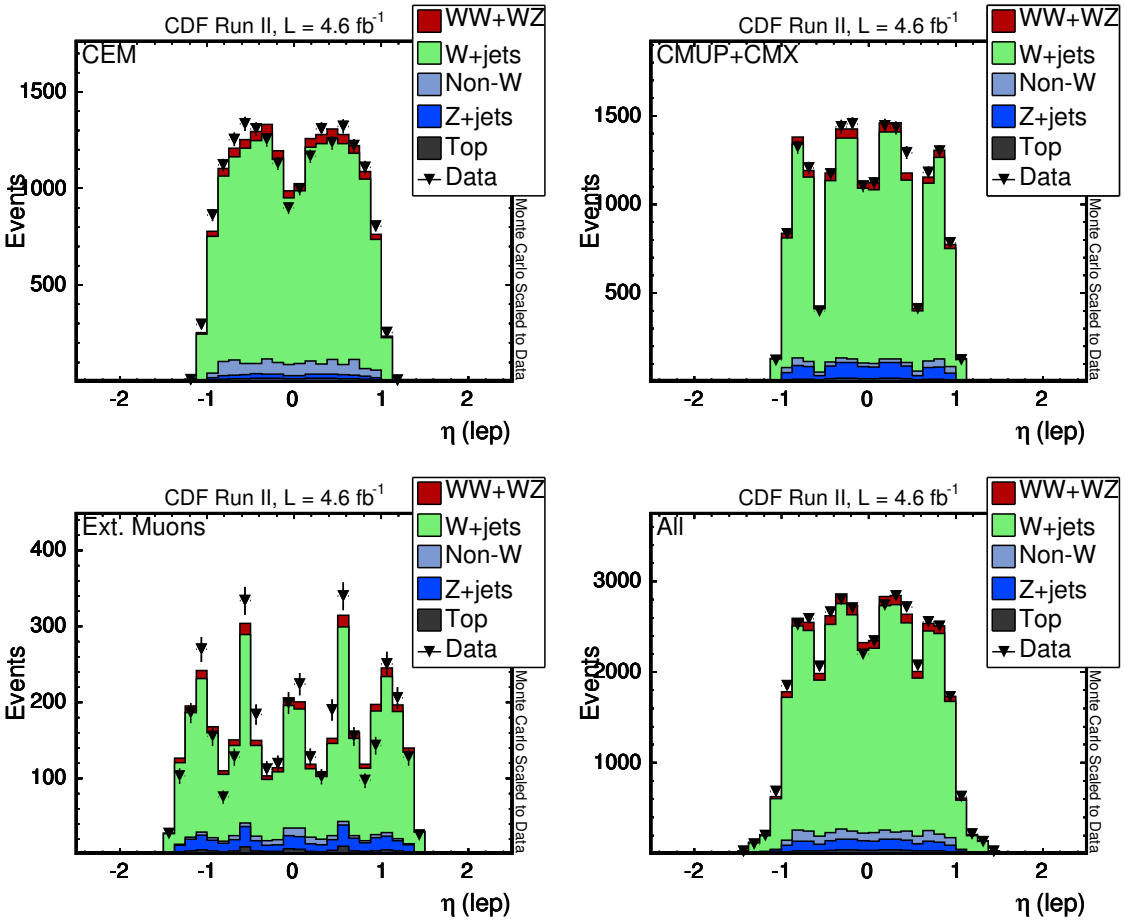

Figure 4.8: Comparison between the lepton η distribution observed in data and the predicted model.

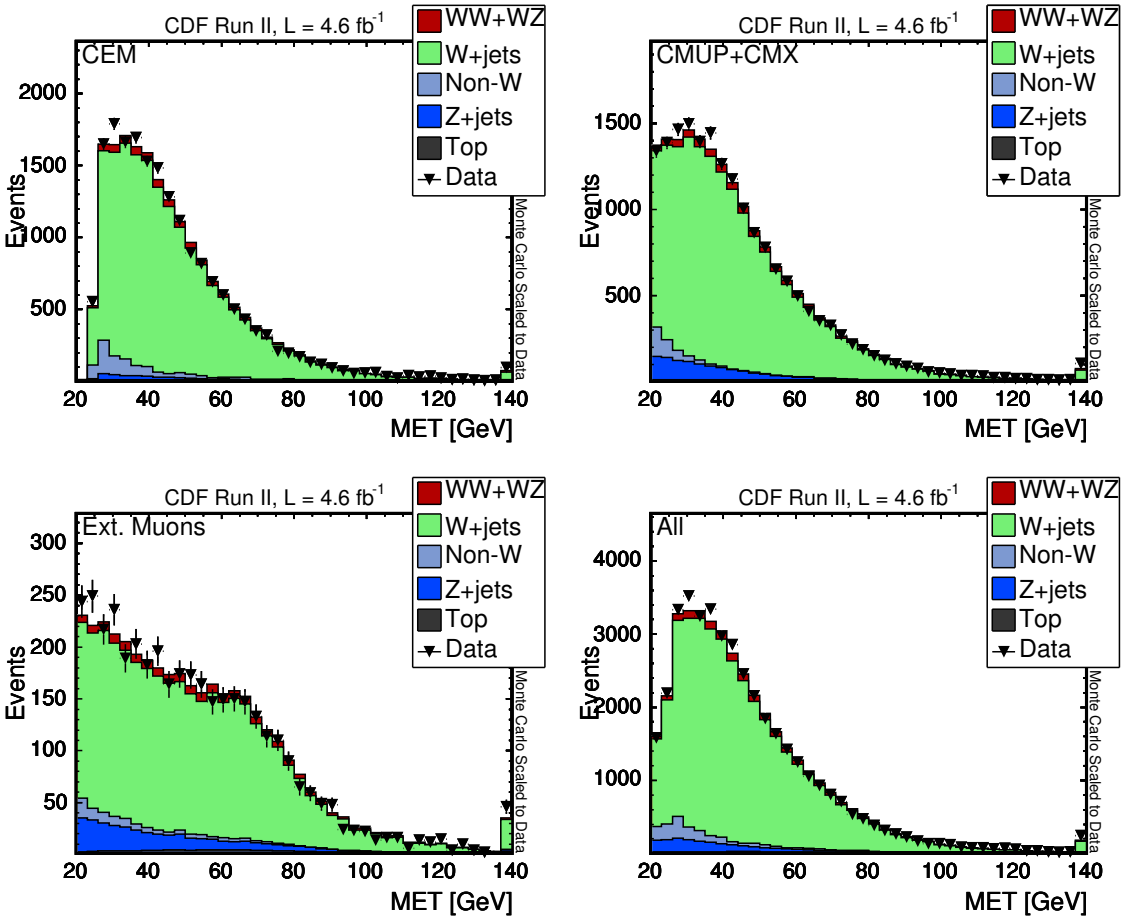

Figure 4.9: Comparison between the $\not\!\!E_T$ distribution observed in data and the predicted model.

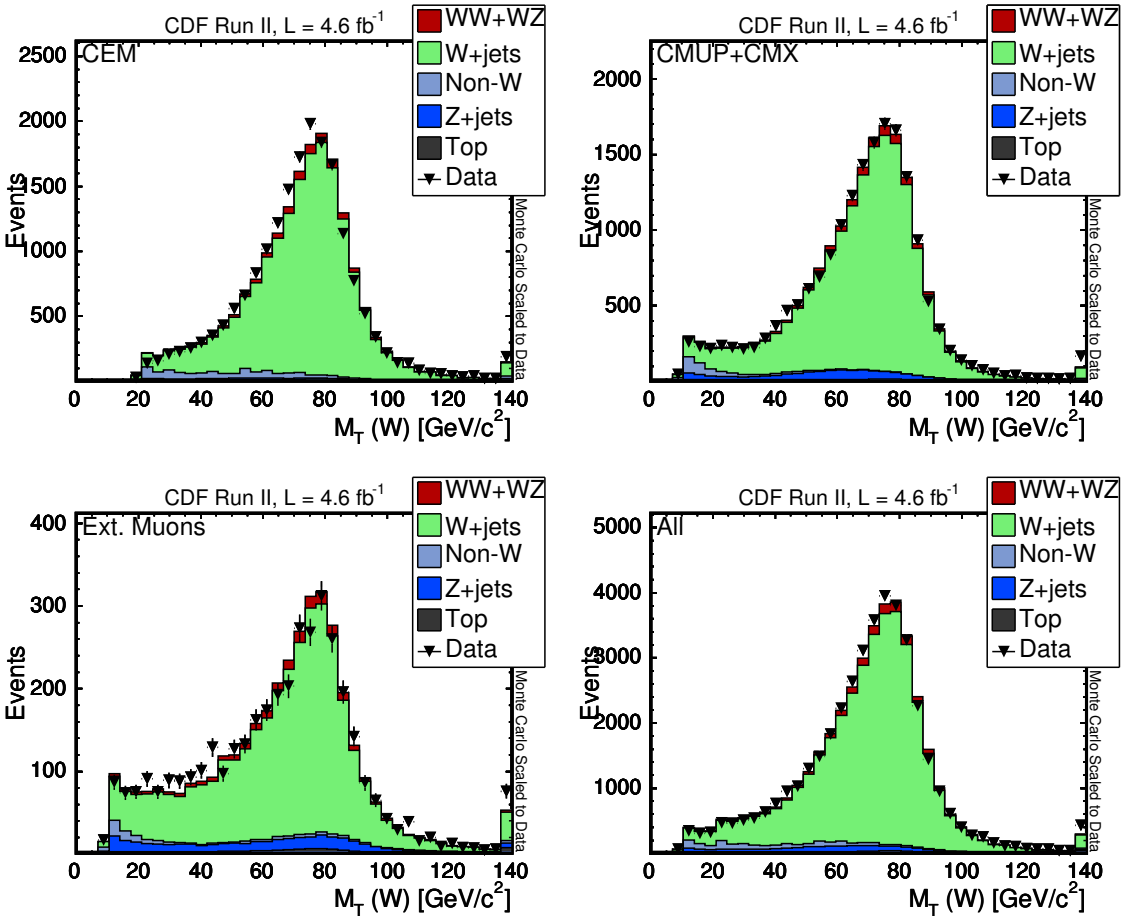

Figure 4.10: Comparison between the transverse mass of the leptonic W ($\not\!\!E_T$ + lepton system) distribution observed in data and the predicted model.

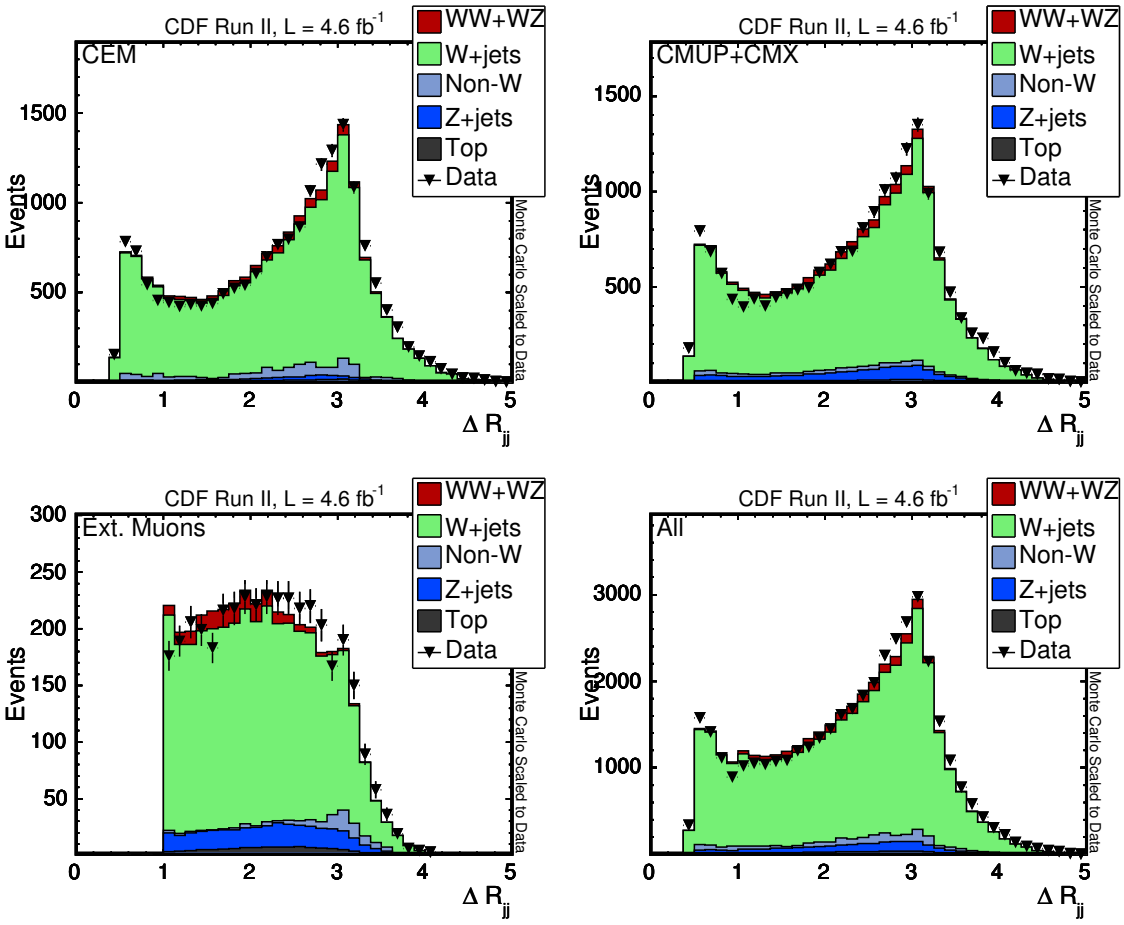

Figure 4.11: Comparison of the angular separation between the two jets observed in data and the predicted model.

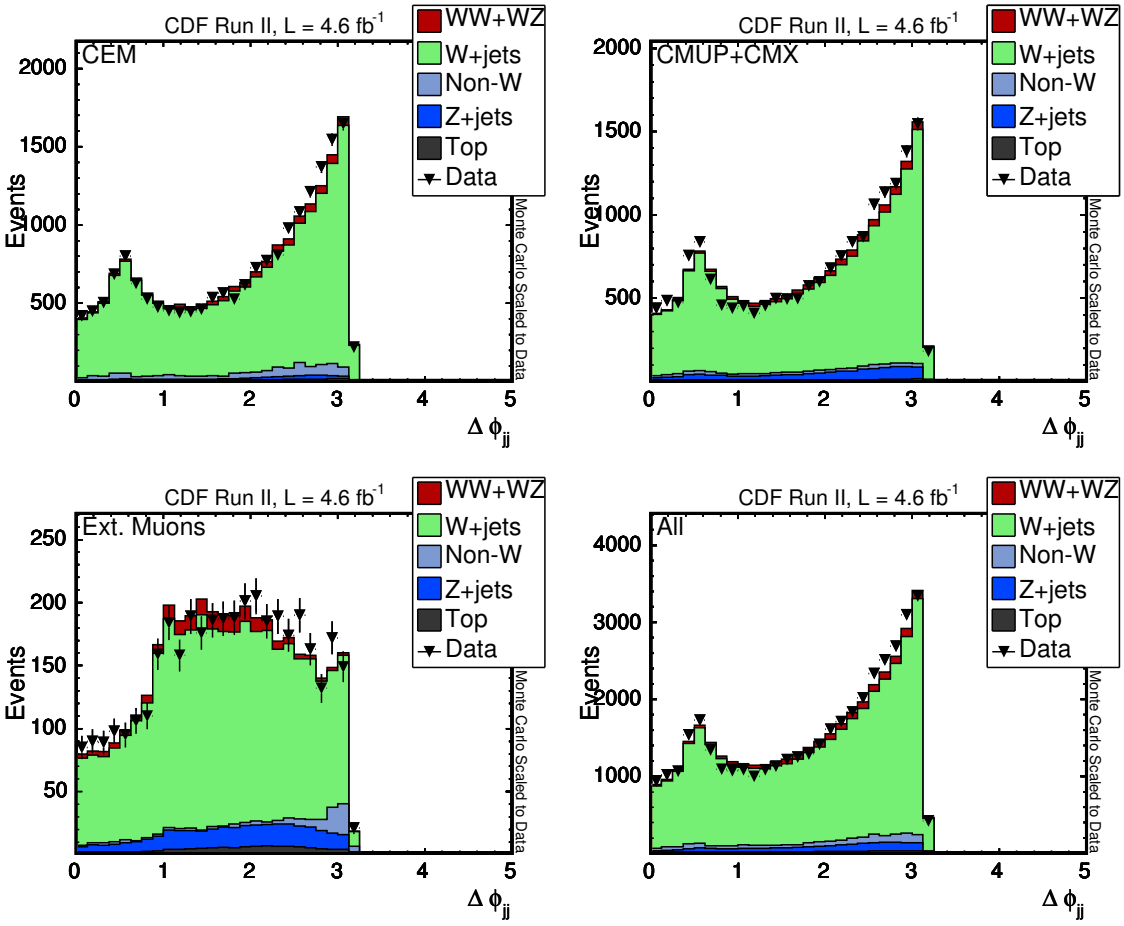

Figure 4.12: Comparison of the $\Delta\phi$ between the two jets observed in data and the predicted model.

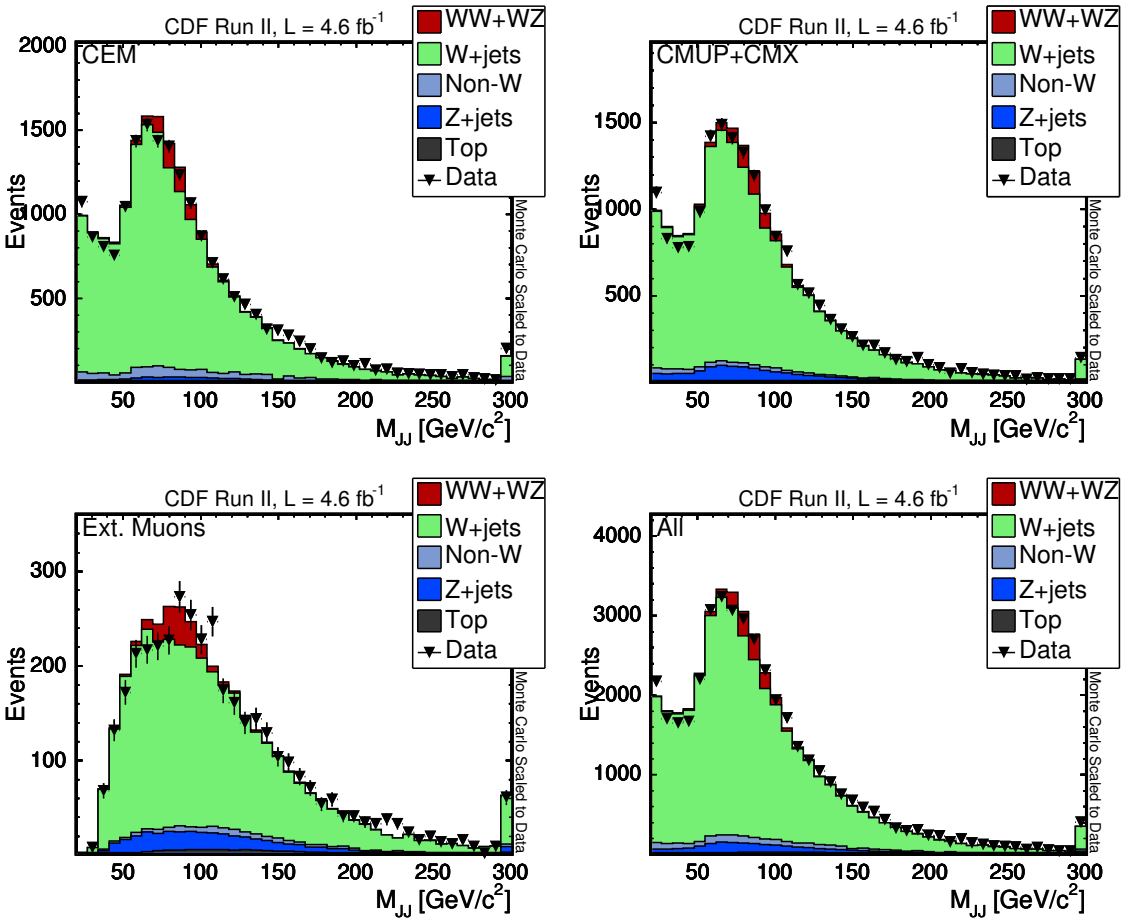

Figure 4.13: Comparison of the invariant mass of the two jets observed in data and the predicted model.

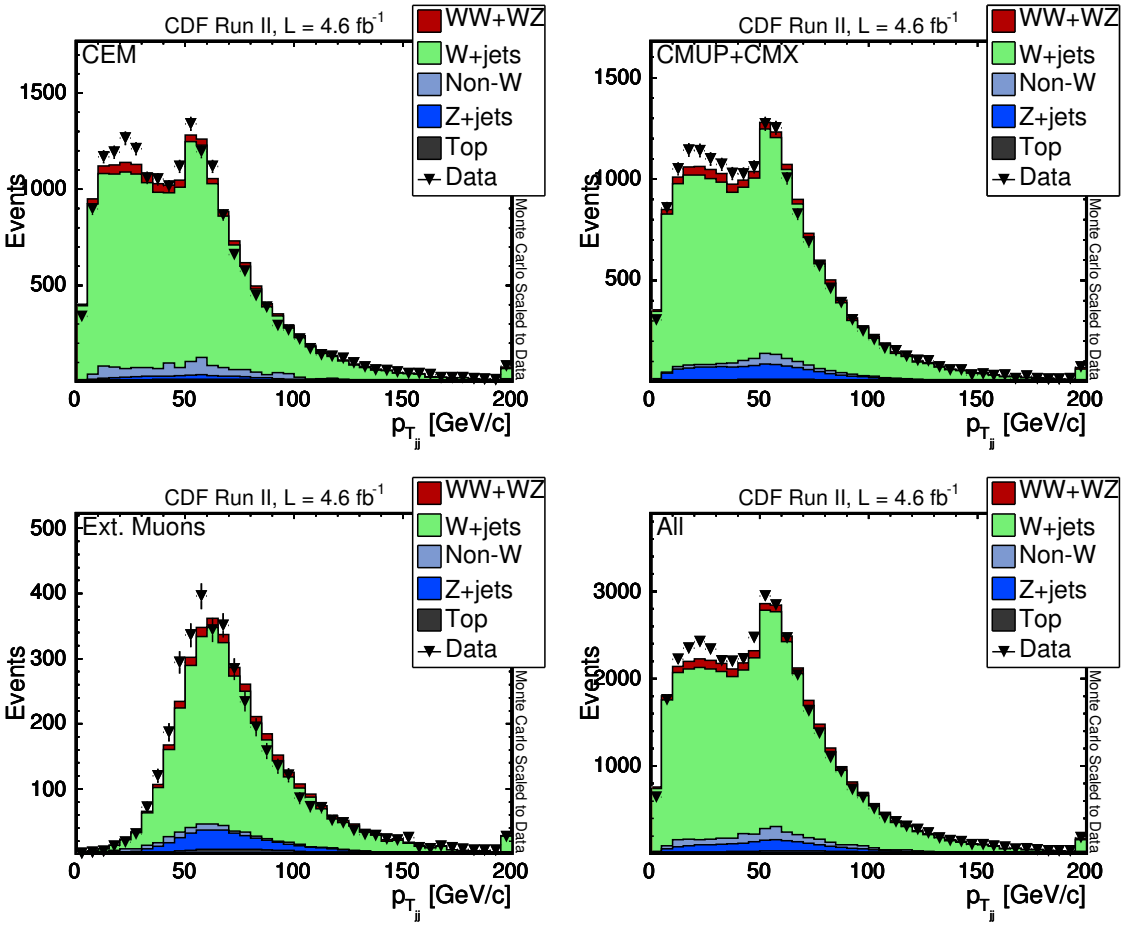

Figure 4.14: Comparison of the p_T of the dijet system observed in data and the predicted model.

CHAPTER 5

MATRIX ELEMENT METHODOLOGY

Based on the expected event yields presented in the previous chapter, nearly 30 times as many background as signal events should pass our event selection. Extracting the signal from the large background is difficult, so we use a matrix element technique that takes advantage of our knowledge of the event kinematics and the production mechanisms of the signal and background processes.

The matrix element method defines a likelihood for an event to be due to a given production process based on the differential cross section of the process. The likelihoods associated with different processes are combined to form a discriminant that will have a different shape for signal and background processes. The details of the matrix element method are described in this chapter.

5.1 Event probabilities

In general the differential cross section for an n-body final state with two incoming particles with momenta $\vec{q_1}$ and $\vec{q_2}$ and masses m_1 and m_2 is

$$d\sigma = \frac{(2\pi)^4 |\mathcal{M}|^2}{4\sqrt{(\vec{q_1}\cdot\vec{q_2})^2 - m_1^2 m_2^2}} \times d\Phi_n \tag{5.1}$$

where $d\Phi_n$ is a phase space factor given by

$$d\Phi_n = \delta^4(q_1 + q_2 - \sum_{i=1}^{n} p_i) \prod_{i=1}^{n} \frac{d^3 p_i}{(2\pi)^3 2E_i} \tag{5.2}$$

and E_i, p_i are the energies and momenta of the outgoing particles [1]. $\mathcal{M}$ is the matrix element of the process.

One can define a probability density for a given process by normalizing the differential cross section to the total cross section:

$$P \sim \frac{d\sigma}{\sigma}. \tag{5.3}$$

We do not include all of the constants necessary to define a true probability density in our calculation, so P is in fact a quantity proportional to a probability.

If one could measure exactly all of the momenta of incoming and outgoing particles, one could evaluate P for any process given the matrix element. In reality, however, the incoming parton energies cannot be measured and the final-state parton measurements are smeared by the experimental resolution. We integrate over all possible values of unknown or poorly known quantities:

$$P(x) = \frac{1}{\sigma} \int d\sigma(y) dq_1 dq_2 f(q_1) f(q_2) W(y, x), \tag{5.4}$$

where $f(q_1)$ and $f(q_2)$ are the parton distribution functions for the initial state partons and $W(y, x)$ is a transfer function relating measured quantities to parton-level quantities in the final state.

The parton distribution functions (PDFs) for the initial state partons are evaluated according to the CTEQ6.1 parameterization [20]. The PDFs give the probability density of finding a certain parton (quark or gluon) with a given fraction of the proton's longitudinal momentum as a function of the momentum transfer of the collision. If it is not clear whether the parton originated in the proton or anti-proton, the probabilities of both possibilities are evaluated and added together.

The effects of experimental measurement on the final state are treated as follows: the lepton energy and angle, as well as the jet angles, are assumed to be measured exactly. A transfer function (described in more detail in the next section) relates the measured jet energy to the parton energy.

The integrals over the PDFs and transfer function are carried out numerically. At each step of the integration, conservation of momentum is used to derive the momentum of the neutrino. Thus the measured $\not\!\!E_T$ is not used in the matrix element calculation. The z-momentum of the neutrino, p_z^ν cannot be determined by conservation of momentum because the z-momentum of the incoming parton system is not known. An additional integral over all possible values of p_z^ν is carried out [28].

Using equations 5.1 and 5.2 and neglecting the masses and transverse momenta of the initial partons, the full expression for a 4-particle final state is [28]

$$P(x) = \frac{1}{\sigma} \int 2\pi^4 |\mathcal{M}|^2 \frac{f(y_1)}{|E_{q1}|} \frac{f(y_2)}{|E_{q2}|} W(y,x) d\Phi_4 dE_{q1} dE_{q2}. \tag{5.5}$$

5.2 Transfer functions

The transfer function relating jet energy to parton energy parameterizes the shape of the $\delta_E = E_{parton} - E_{jet}$ distribution. A distribution of this quantity for jets originating from gluons, light flavor quarks, and b quarks is shown in Figure 5.1.

A double Gaussian parameterization is used to account for the central peak and long tail of the δ_E shape:

$$W_{jet}(E_{parton}, E_{jet}) = \frac{1}{\sqrt{2\pi}(p_2 + p_3 p_5)} (\exp \frac{-(\delta_E - p_1)^2}{2p_2^2} + p_3 \exp \frac{-(\delta_E - p_4)^2}{2p_5^2}). \tag{5.6}$$

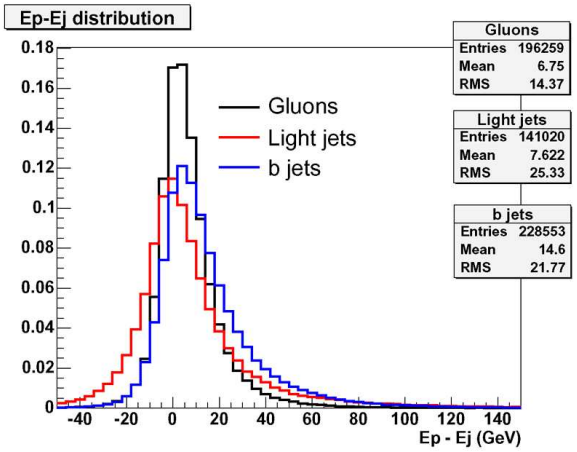

Figure 5.1: Transfer function (parton energy minus jet energy) for jets originating from light-flavor (up, down, and strange) quarks, bottom quarks, and gluons.

The parameters p_i are a linear function of the parton energy, $p_i = a_i + b_i E_{parton}$. The parameterization is derived in three η bins, $|\eta| < 0.8$, $0.8 < |\eta| < 1.2$, and $|\eta| > 1.2$.

Separate parameterizations are derived for light flavor quark jets, gluon jets, and b quark jets. The parameterization chosen is based on the diagram used; for example for the diagrams corresponding to W production in association with two b quarks (Wbb), we use the b quark parameterization. When there are two possible permutations, as in the case of the matrix element for W produced in association with a quark and a gluon, the event probability is calculated for each combination of transfer functions and the two results are added together.

5.3 Signal and background diagrams

We evaluate the matrix element probabilities for the signal processes and a selection of background processes. Having probabilities associated with every background process would in principle give the greatest discrimination power, but is not necessary for the

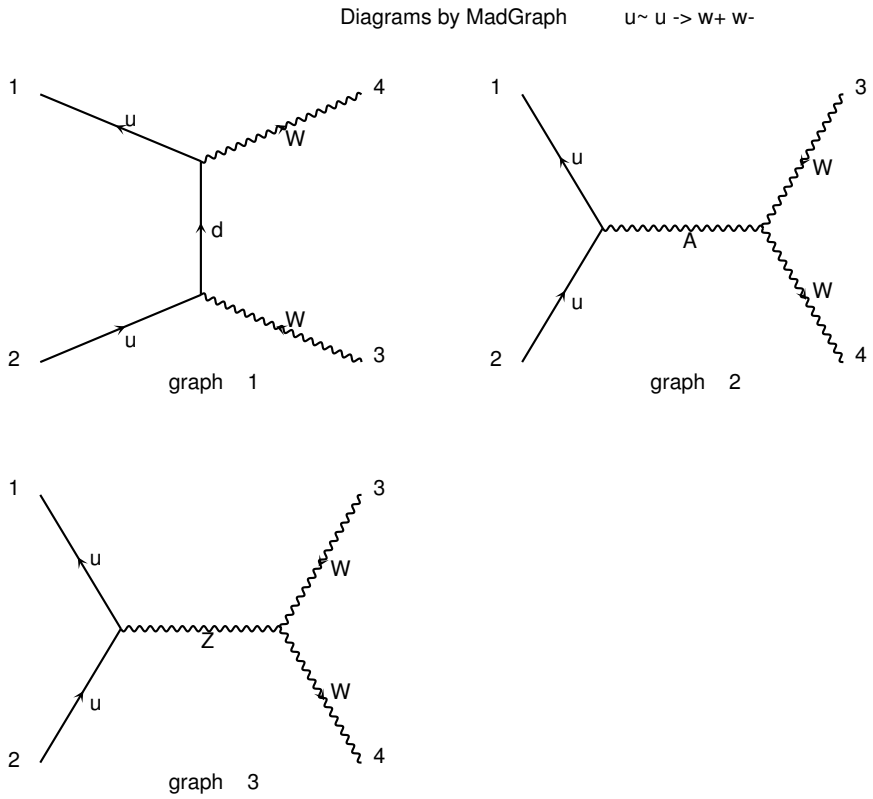

Figure 5.2: Leading-order WW production diagrams.

technique to be successful. The leading-order diagrams used for the matrix element calculation are provided by MADGRAPH[19].

The diagrams for the signal WW and WZ processes are shown in Figures 5.2 and 5.3.

The W+jets background is broken into contributions due to $W+$ two gluons (Wgg), $W+$ one gluon and one quark (Wgj), $W+$ two b-quarks (Wbb), and $W+$ one c-quark and one gluon (Wcg). A subset of the relevant diagrams is shown in Figures 5.4 and 5.5.

The matrix element probability is also calculated for the single top background, divided into three diagrams: s-channel and two t-channel contributions. While the background

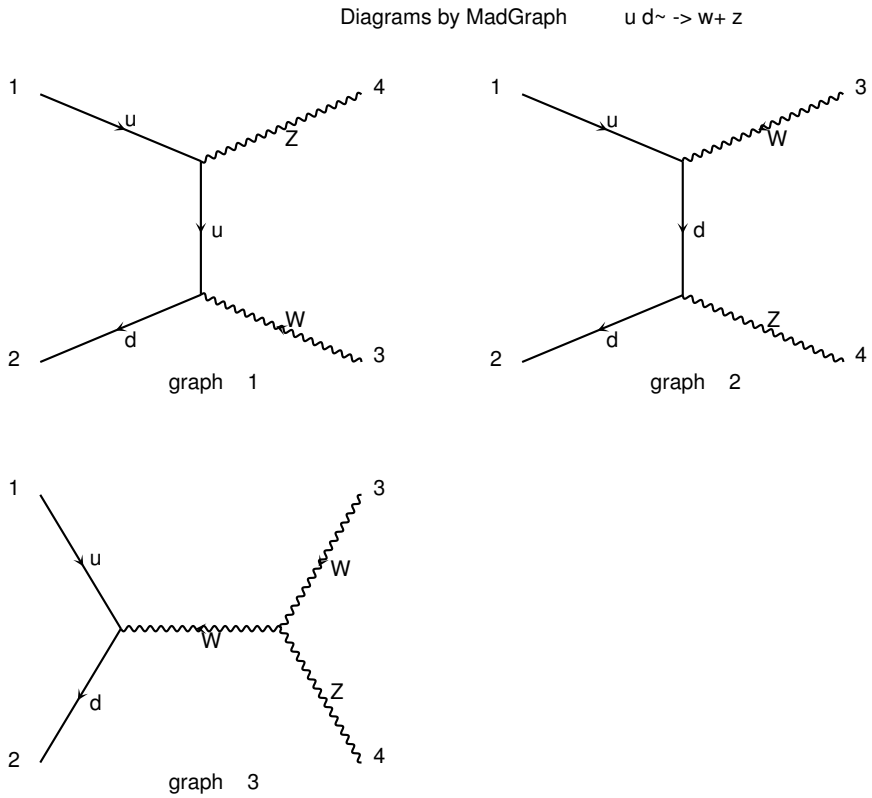

Figure 5.3: Leading-order WZ production diagrams.

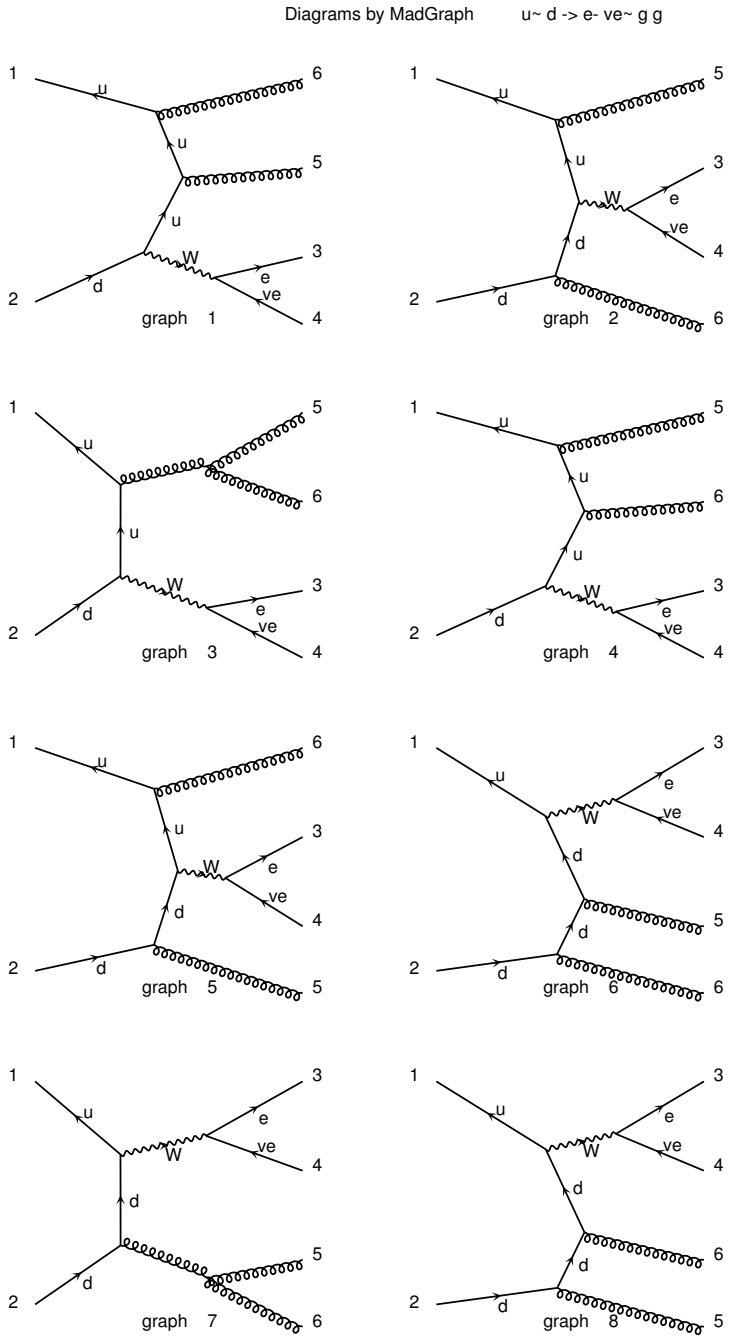

Figure 5.4: Examples of the Wgg production diagrams.

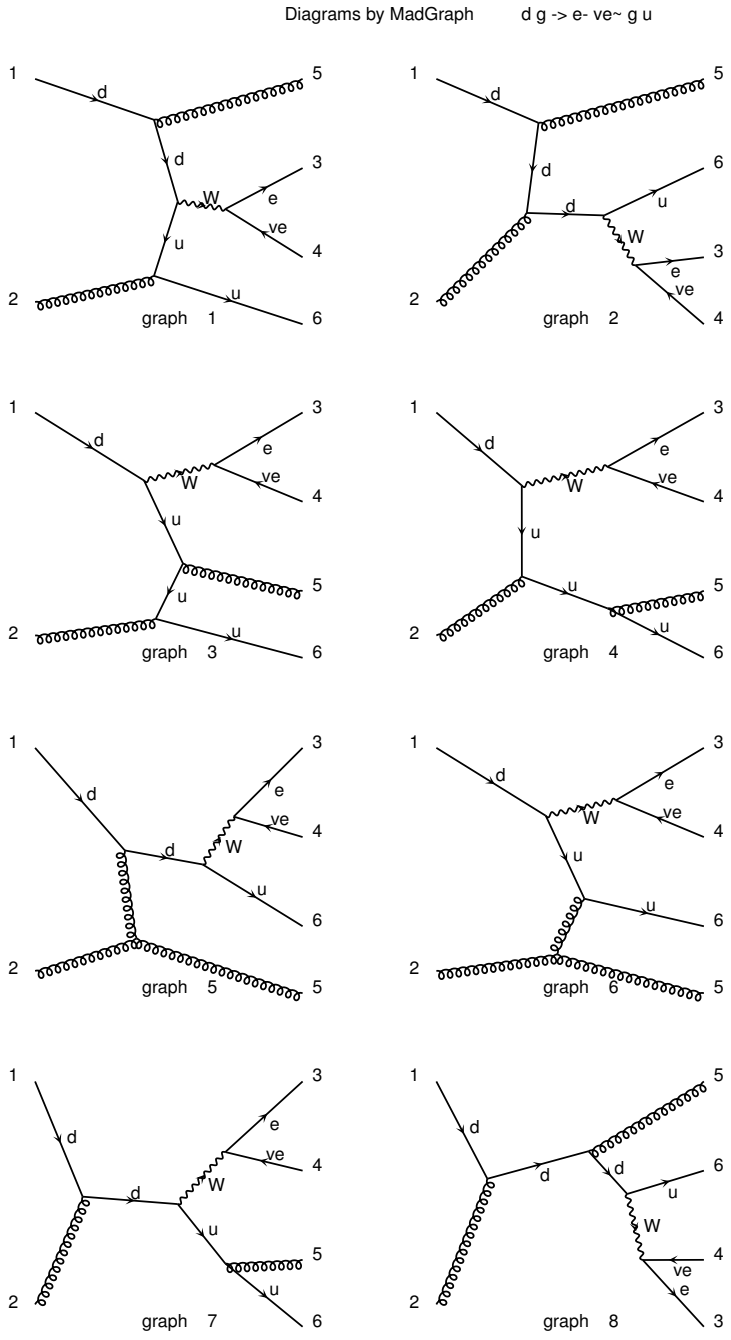

Figure 5.5: Examples of the Wgq production diagrams.

due to single top production is small, the calculation of the matrix elements was previously implemented for the single top searches and does not cost much computing time.

No matrix element calculation is carried out for the $t\bar{t}$, Z+jets, and QCD multi-jet backgrounds. All of these backgrounds require some additional assumptions, making the matrix element calculation more difficult. For example, $t\bar{t}$ events become a background if several jets or a lepton are not detected; dealing with this in the matrix element calculation requires additional integrations and a great deal of extra computing time. For the Z+jets background, a lepton either fakes a jet or escapes detection, two scenarios difficult to describe in the matrix element calculation. Finally, the QCD multi-jet background would require a large number of leading-order diagrams as well as a description of quarks or gluons faking leptons. The Z+jets and QCD background look very different than the signal (i.e. there will be no dijet W/Z resonance) so we expect good discrimination even without including probabilities explicitly for those backgrounds.

5.4 Event Probability Discriminant

The probabilities for individual processes described above (P_i, where i runs over the processes) are combined to form a discriminant, a quantity with a different shape for background-like events than for signal-like events. The way in which the probabilities are combined to form a discriminant is somewhat arbitrary, but generally the discriminant has the form $P_{signal}/(P_{background} + P_{signal})$ so that background-like events will take values close to zero and signal-like events will have values close to unity. The P_{signal} and $P_{background}$ are just the sum of individual probabilities for signal and background processes, but we put in some additional factors to form the Event Probability Discriminant, or EPD.

First, as noted above, the P_i are not true probability densities in that they are not normalized. We normalize the the P_i relative to each other by calculating them for each event in large Monte Carlo samples. We then find the maximal P_i over all Monte Carlo events corresponding to a given process, P_i^{max}. The normalized probabilities are then given by P_i/P_i^{max}.

In addition, we multiply each P_i by a coefficient, C_i. This coefficient has the effect of weighting some probabilities more than others in the discriminant. The full EPD is then given by:

$$EPD = \frac{\sum_{i=1}^{n_{sig}} \frac{C_i P_i}{P_i^{max}}}{\sum_{i=1}^{n_{sig}} \frac{C_i P_i}{P_i^{max}} + \sum_{j=1}^{n_{BG}} \frac{C_j P_j}{P_j^{max}}}, \tag{5.7}$$

where the summation over signal processes runs over WW and WZ ($n_{sig} = 2$) and the summation over background processes runs over Wgg, Wgj, Wbb, Wcg, and the single top diagrams.

The coefficients C_i change the shape of the EPD and can be optimized to achieve the greatest expected sensitivity in the signal extraction. Running through the full signal extraction with different values of the coefficients is not feasible, so a simplified fit is carried out. The optimization is performed using only Monte Carlo models (no data) and the expected yields of signal and background processes.

The simplified version of the signal extraction is a maximum likelihood fit to extract β, the ratio between the $WW + WZ$ cross section and the predicted $WW + WZ$ cross section. The likelihood is defined as

$$L(\beta) = \sqrt{\sum_{i=1}^{n_{bin}} \frac{(\beta S_i)^2}{(\beta S_i) + B_i + (\beta \Delta S_i)^2 + (\Delta B_i)^2}}, \tag{5.8}$$

where S_i and B_i are the expected number of signal and background events in the ith bin. ΔS_i and ΔB_i are the statistical uncertainty on S_i and B_i, where both the expected Poisson uncertainty and the uncertainty due to limited Monte Carlo statistics are taken into account.

The effect of the optimization of the coefficients C_i is illustrated in Figure 5.6. The EPD when all C_i are set to unity is shown on the left for the WW signal and the W+jets background. The optimized EPD is shown on the right. The coefficients increase the difference in shape between signal and background and as a result increase the sensitivity of the analysis.

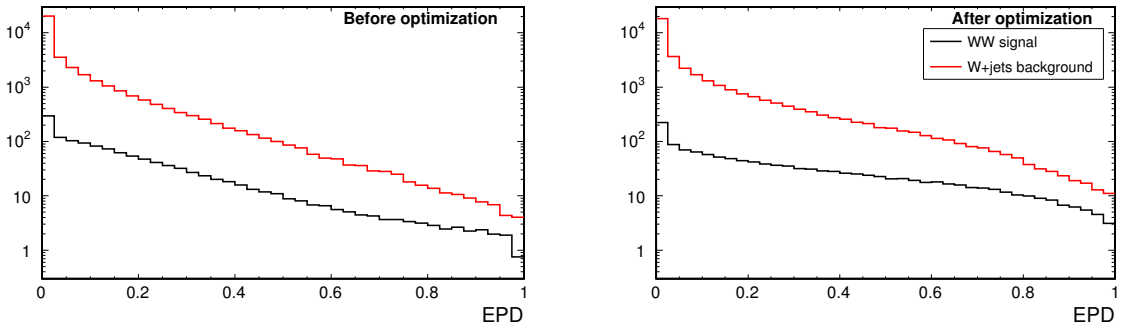

Figure 5.6: WW and W+jets EPD before coefficient optimization (left) and after coefficient optimization (right).

Figure 5.7 (left) shows the EPD templates for signal and background processes normalized to unit area. The background processes all have similar shapes while the signal process falls more slowly. A stack plot with the expected normalizations of signal and background processes taken from Table 4.3 is shown in Figure 5.7 (right).

We validate the modeling of the EPD for background events by comparing data and simulation in the region with $M_{jj} < 55$ GeV/c^2 and $M_{jj} > 120$ GeV/c^2, where we expect very little signal. The result of the comparison is shown in Figure 5.8. The agreement between data and simulation is very good.

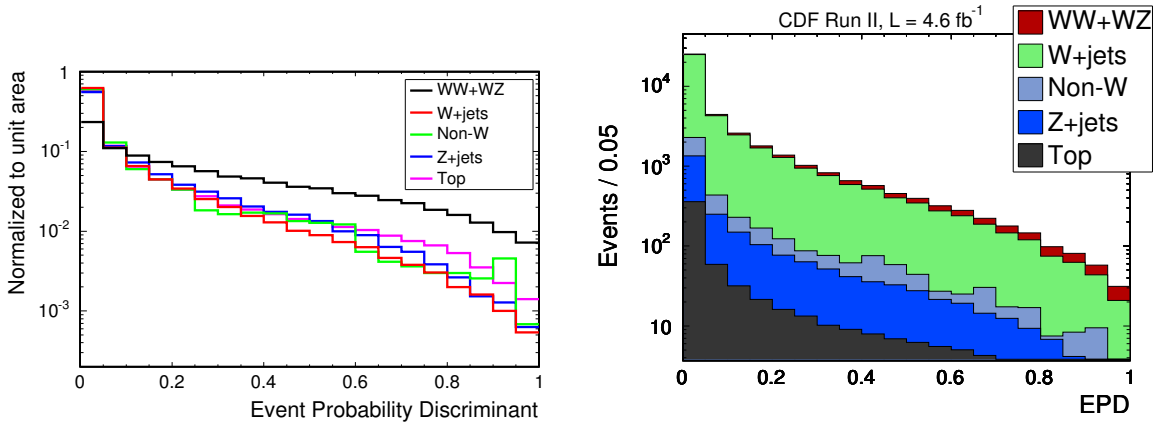

Figure 5.7: Shape of the EPD for signal and background processes, normalized to unity (left) and stacked with expected normalizations (right).

5.5 Effectiveness of the discriminant

The effectiveness of the EPD in isolating signal-like events can be seen by plotting the invariant mass of the two jets (dijet mass, or M_{jj}). This quantity is expected to have a resonance around the W or Z mass for signal-like events. Stack plots of M_{jj} in four EPD ranges are shown in in Figure 5.9. The bin with low EPD values (0<EPD<0.25), in the top left plot, has events in the full dijet mass range from 20 to 200 GeV. For EPD>0.25, however, the M_{jj} distribution is a peak around the W/Z mass. As the EPD range approaches unity, the expected signal-to-background ratio increases.

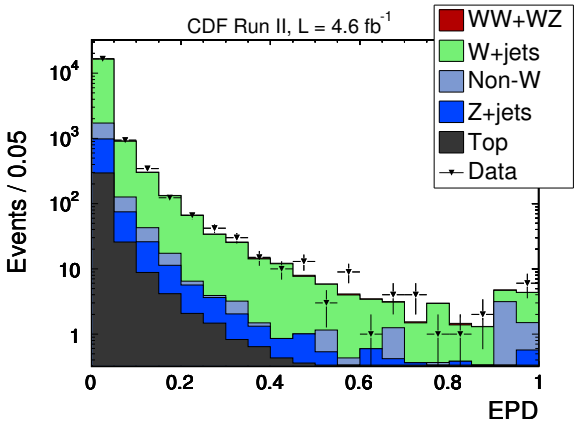

Figure 5.8: Comparison of the EPD in data and simulation for events with $M_{jj} < 55$ GeV or $M_{jj} > 120$ GeV.

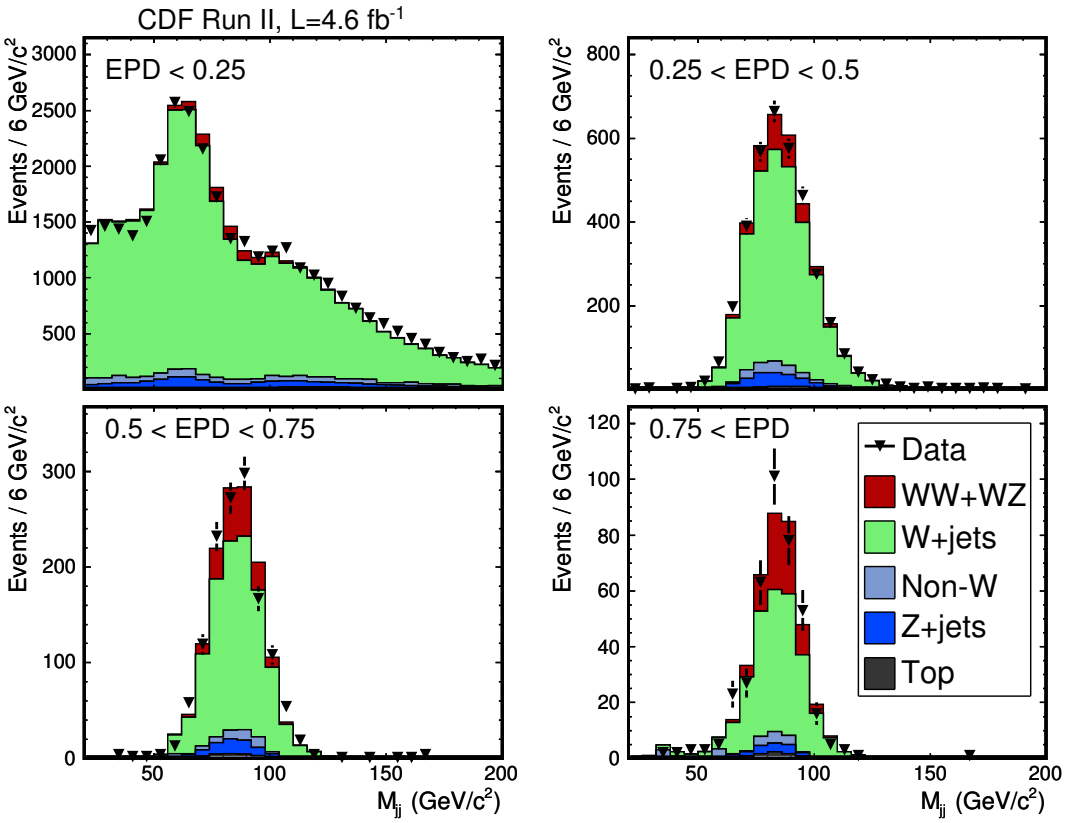

Figure 5.9: Distribution of the dijet mass in four EPD bins.

CHAPTER 6

LIKELIHOOD FIT

The cross section of the diboson signal is extracted by fitting the shape of the Event Probability Discriminant in the data to a sum of signal and background templates. We also extract a signal significance, a measure of whether or not the signal could be due to a background fluctuation. The fitting procedure is described in detail in this chapter.

6.1 Fitting procedure

We use a Bayesian approach to a maximum likelihood fit. Given a set of observables x from which we wish to determine a quantity θ, the posterior p.d.f. $p(\theta|x)$ can be determined using Bayes' theorem:

$$p(\theta|x) = \frac{L(x|\theta)\pi(\theta)}{\int L(x|\theta')\pi(\theta')d\theta'}, \tag{6.1}$$

where $L(x|\theta)$ is the likelihood function and $\pi(\theta)$ is the prior p.d.f. for θ [1]. The value at which the posterior p.d.f. is maximal is the fitted cross section, and the smallest interval around this value covering 68% of the total area of the p.d.f. defines the uncertainty on the measurement.

We use a package called MCLIMIT for our statistical treatment [29, 30]. Some details of its implementation are given here.

6.1.1 Treatment of systematic uncertainties

Systematic uncertainties are treated as nuisance parameters with prior p.d.f.s parameterizing their range of possible values. The uncertainties are marginalized, or integrated over, to derive a likelihood that is only a function of the parameter of interest [1]. Given systematic uncertainties ν with prior p.d.f.s $\pi(\nu)$,

$$L(x|\theta) = \int L'(x|\theta,\nu)\pi(\nu)d\nu. \tag{6.2}$$

In our fit, we wish to determine the $WW + WZ$ cross section, $\sigma(WW + WZ)$, which we parameterize as $\beta = \sigma(WW + WZ)/\sigma_{NLO}(WW + WZ)$, or the ratio of the measured cross section to the predicted NLO cross section. The prior p.d.f. of β is taken to be flat in all non-negative values of β. The nuisance parameters are assigned Gaussian priors, and are renormalized by their estimated standard deviations to obtain standard normal distributions.

When integrating over the prior p.d.f. of a nuisance parameter, some regions may contribute more to the likelihood than others and if some regions of the p.d.f. lead to very low likelihoods, they can effectively be excluded. In such a case the likelihood fit is actually constraining the value of a nuisance parameter, and by examining the posterior p.d.f. of that nuisance parameter one can conclude the regions strongly favored by the fit.

If there are many nuisance parameters, integrating over all of their prior p.d.f.s can be challenging. A numerical integration method that randomly samples the full space of a nuisance parameter's prior p.d.f. is a standard approach, but can run into difficulty when a nuisance parameter is strongly constrained and many of the integration points fall outside of the region relevant to the fit. Since that is a concern in our fit, we use a Markov Chain

Monte Carlo integration, which more efficiently finds the regions of nuisance parameter space contributing most to the likelihood [31].

6.1.2 The likelihood function

The definition of the likelihood function starts from the standard likelihood for a Poisson distributed variable:

$$L(\beta) = \frac{\mu^n}{n!} e^{-\mu}, \tag{6.3}$$

where μ is the number of expected events given β (with N_b background events and N_s signal events, $\mu = \beta N_s + N_b$) and n is the number of observed events. For a histogram with several bins,

$$L(\beta) = \prod_{k=1}^{n_{bin}} \frac{\mu_k^{n_k}}{n_k!} e^{-\mu_k} \tag{6.4}$$

and $\mu_k = \beta N_{sk} + N_{bk}$. Changing notations to reflect that the signals and backgrounds are a sum over processes, this becomes $\mu_k = \beta \sum_{j=1}^{2} N_{jk} + \sum_{j=3}^{n_b+2} N_{jk}$, where the first summation runs over the two signal processes (WW and WZ) and n_b is the number of background processes.

Systematic uncertainties are incorporated into the likelihood function as follows. Each systematic uncertainty i (up to n_{sys} total) is parameterized with nuisance parameter δ_i. The $\pm 1\sigma$ change in the normalization of the process j due to systematic uncertainty i is given by ϵ_{ji}. Integrating over all nuisance parameters, the likelihood is

$$L(\beta) = \int_{-\infty}^{\infty} \prod_{i=1}^{n_{sys}} d\delta_i \frac{1}{\sqrt{2\pi}} \exp(-\frac{{\delta_i}^2}{2}) \prod_{k=1}^{n_{bin}} \frac{\mu_k^{n_k}}{n_k!} e^{-\mu_k} \tag{6.5}$$

and $\mu_k = \beta \sum_{j=1}^{2} N_{jk} S_j + \sum_{j=3}^{n_b+2} N_{jk} S_j$, where S_j is a systematic factor given by

$$S_j = \prod_{i=1}^{n_{sys}} (1 + \delta_i \epsilon_{ji}). \tag{6.6}$$

The systematic factor described above takes into account the change in the normalization or rate of a given process due to a systematic uncertainty. In addition, the contribution of the systematic may vary with the histogram bin (i.e. the systematic uncertainty may affect the shape of the histogram). To take this into account, we define κ_{jik} as the change in the value of bin k of process j due to uncertainty i. The systematic factor is then bin-dependent, meaning

$$\mu_k = \beta \sum_{j=1}^{2} N_{jk} S_{jk} + \sum_{j=3}^{n_b+2} N_{jk} S_{jk} \tag{6.7}$$

and

$$S_{jk} = \prod_{i=1}^{n_{sys}} (1 + \delta_i \epsilon_{ji})(1 + \delta_i \kappa_{jik}). \tag{6.8}$$

Finally we must account for the fact that the effect of a systematic uncertainty may not be symmetric about the mean of a certain parameter. In this case we adopt a model where the single Gaussian prior p.d.f. for the nuisance parameter is replaced by two Gaussian distributions connected by a Heaviside step function. Breaking the ϵ_{ji} (κ_{jik}) defined earlier into ϵ_{ji+} and ϵ_{ji-} (κ_{jik+} and κ_{jik-}), the systematic factor becomes

$$S_{jk} = \prod_{i=1}^{n_{sys}} (1 + |\delta_i|(\epsilon_{ji+} H(\delta_i) + \epsilon_{ji-} H(-\delta_i)))(1 + |\delta_i|(\kappa_{jik+} H(\delta_i) + \kappa_{jik-} H(-\delta_i))). \tag{6.9}$$

The δ_i correlate shape and normalization uncertainties due to the same source.

To summarize, the full likelihood is given by Eq. 6.5, with μ_k defined as in Eq. 6.7 and the systematic factor defined as in Eq. 6.9.

6.2 Cross-checks of the fit

We use pseudo-experiments to check for any bias in the fitting procedure and to evaluate the expected precision of the measurement. The pseudo-experiments are generated by varying the bin contents of each template histogram according to Poisson distributions as well as randomly setting a value for each nuisance parameter according to its p.d.f. The pseudo-experiments are generated with a certain value of β, β_{exp}. The likelihood fit is applied to each pseudo-experiment to extract the fitted β, β_{meas}, with asymmetric uncertainties σ^{+}_{meas} and σ^{-}_{meas}.

In order to check that there is no bias in the fitting procedure, we plot the β_{meas} for 3000 pseudo-experiments generated with $\beta_{exp} = 1$. The mean β_{meas} is unity, meaning the fit is unbiased. We also check that the 1σ uncertainties on β contain 68% of the possible outcomes by checking the pull of the pseudo-experiments. The pull is defined as follows for fits with asymmetric uncertainties [32]:

$$\text{Pull} = \begin{cases} \frac{\beta_{exp}-\beta_{meas}}{\sigma^{+}_{meas}} & , \quad \beta_{meas} \leq \beta_{exp} \\ \frac{\beta_{meas}-\beta_{exp}}{\sigma^{-}_{meas}} & , \quad \beta_{meas} > \beta_{exp} \end{cases} \tag{6.10}$$

If the mean is being fit in an unbiased way, the mean pull will be zero. If the 1σ uncertainties are being calculated with the correct 68% coverage, the width of the pull will be one. The pulls for 3000 pseudo-experiments are shown in Figure 6.1 (right). The pulls have the proper behavior, with a mean of zero and a width of unity.

A second check of the fitting procedure is that it is linear as a function of β_{exp}. To test

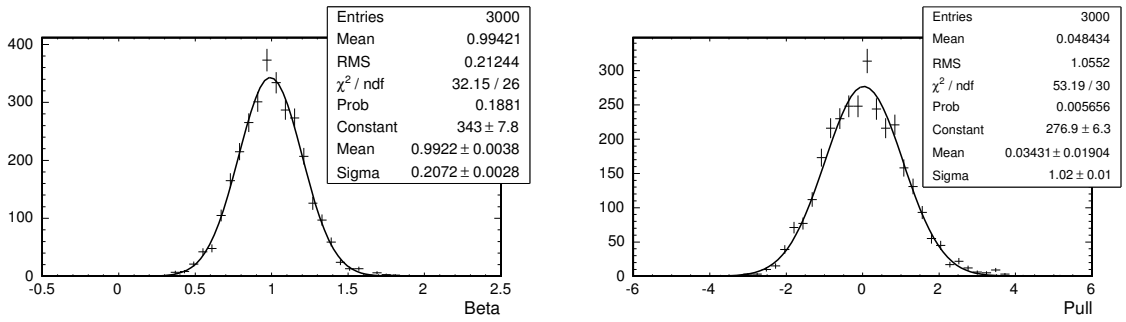

Figure 6.1: Fitted β and pulls of 3000 pseudo-experiments.

this, pseudo-experiments with different input values of β_{exp} were generated and the fit was applied to them. The measured cross section as a function of the input cross section is shown in Figure 6.2. The measurement scales with the input as it should.

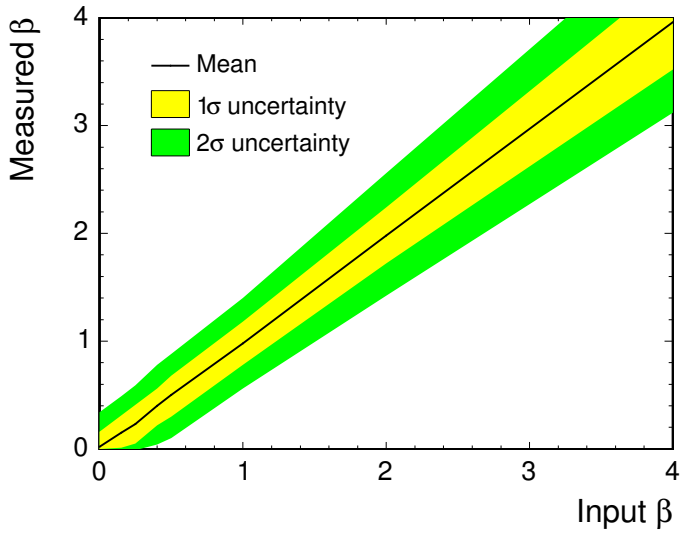

Figure 6.2: Linearity of the fitted cross section as a function of the input cross section in pseudo-experiments.

6.3 Signal significance

The significance of the signal is a measure of how much the data deviates from a model with no $WW + WZ$ production, or a background-only hypothesis. The significance is computed from the p-value, the probability that the background could fluctuate to create the observed signal. Pseudo-experiments assuming a $WW + WZ$ cross section of zero are generated. We determine how "signal-like" a pseudo-experiment (and the data) is by evaluating a test statistic. The test statistic chosen is based on the likelihood ratio $Q = L(1)/L(0)$, where the likelihood is defined as described above with all nuisance parameters set to their central values. $L(1)$ is the likelihood with the $WW + WZ$ cross section set to the predicted value, whereas $L(0)$ is the likelihood with the $WW+WZ$ cross section set to zero, corresponding to the background-only hypothesis. The test statistic is given by $-2 \ln Q$, meaning more signal-like pseudo-experiments have lower values of the test statistic. The p-value is the fraction of pseudo-experiments that have a lower test statistic than the data.

We also evaluate the expected significance, or the sensitivity, of the analysis by generating pseudo-experiments with the $WW + WZ$ production cross section set to the NLO expectation ($\beta = 1$). The test statistic is evaluated for each signal-like pseudo-experiment. The sensitivity is defined as the probability for a background-only pseudo-experiment to have a test statistic less than the median test statistic of the signal-like pseudo-experiments.

The significance is usually expressed in terms of σ, the standard deviation of a Gaussian distribution. The conversion from p-value to the number of σ, x, is done by finding the value x where an integral of a Gaussian distribution with a mean of zero from $x\sigma$ to infinity is equal to the p-value. For example, the integral of a Gaussian distribution with

a mean at zero from 1σ to infinity is about 0.16, so a p-value of 0.16 would correspond to a signal with a 1σ significance.

In summary, the following results will be quoted: the $WW + WZ$ production cross section and its uncertainty, and the significance of the signal. Pseudo-experiments based on Monte Carlo models will be used to evaluate the expected values for these results, while fits to the data will give the observed values.

CHAPTER 7

SYSTEMATIC UNCERTAINTIES

Uncertainties in various aspects of the measurement, like our understanding of the measurement apparatus and the Monte Carlo modeling, can systematically bias its outcome. In this chapter the sources of systematic uncertainty are described, and their effect on the cross section measurement is estimated using pseudo-experiments.

7.1 Sources of systematic uncertainty

Systematic uncertainties can affect both the rate (or predicted event yields) and the shape of the Event Probability Discriminant for signal and background processes. Table 7.1 summarizes the sources of uncertainty that we take into account, and what aspect of the measurement they affect.

7.1.1 Jet energy scale

The corrections used to set the jet energy scale (JES) are described in Chapter 3. The uncertainty on each correction is derived by comparison of data to Monte Carlo or by comparison of different Monte Carlo generators [15]. The size of various uncertainties in the JES as well as the total uncertainty are shown in Figure 7.1.

The dominant source of uncertainty on the JES for jets with $p_T < 60$ GeV is the correction for energy leaking out of the jet cone. For jets with $p_T > 60$ GeV, the uncertainty in the Monte Carlo description of the detector response to single particles is dominant.

Source	Signal normalization	Signal shape	Background normalization	Background shape
Jet energy scale	X	X		X
Parton distribution functions	X			
Initial and final state radiation	X			
Jet energy resolution	X			
Background cross sections			X	
Q^2 scale				X
W+jets modeling				X
Integrated luminosity	X		X	
Lepton identification efficiency	X		X	

Table 7.1: Sources of systematic uncertainty. Aspects of the analysis affected by the uncertainty are marked with an X.

The effect of the JES uncertainty on the measurement is estimated by varying the energy of all jets in Monte Carlo samples by $+1\sigma$ and -1σ, where σ is p_T-dependent and defined by the total uncertainty curve shown in Figure 7.1. This is done for the signal WW and WZ samples and for the dominant W+jets background.

The JES uncertainty has a small effect on the estimated signal acceptance because the efficiency of the jet E_T selection changes with the scale. The size of the acceptance uncertainty is around 1%. The normalization of the W+jets background is not affected significantly because it is determined from data. The more important effect of the JES uncertainty is on the shape of the EPD templates. The change in the EPD for the WW signal is shown in Figure 7.2 and for the W+jets background in Figure 7.3. The change in the background shape is relatively small compared to the change in the signal shape. The signal normalization uncertainty, the signal shape uncertainty, and the background shape uncertainty are all correlated in the fit, since they come from the same source.

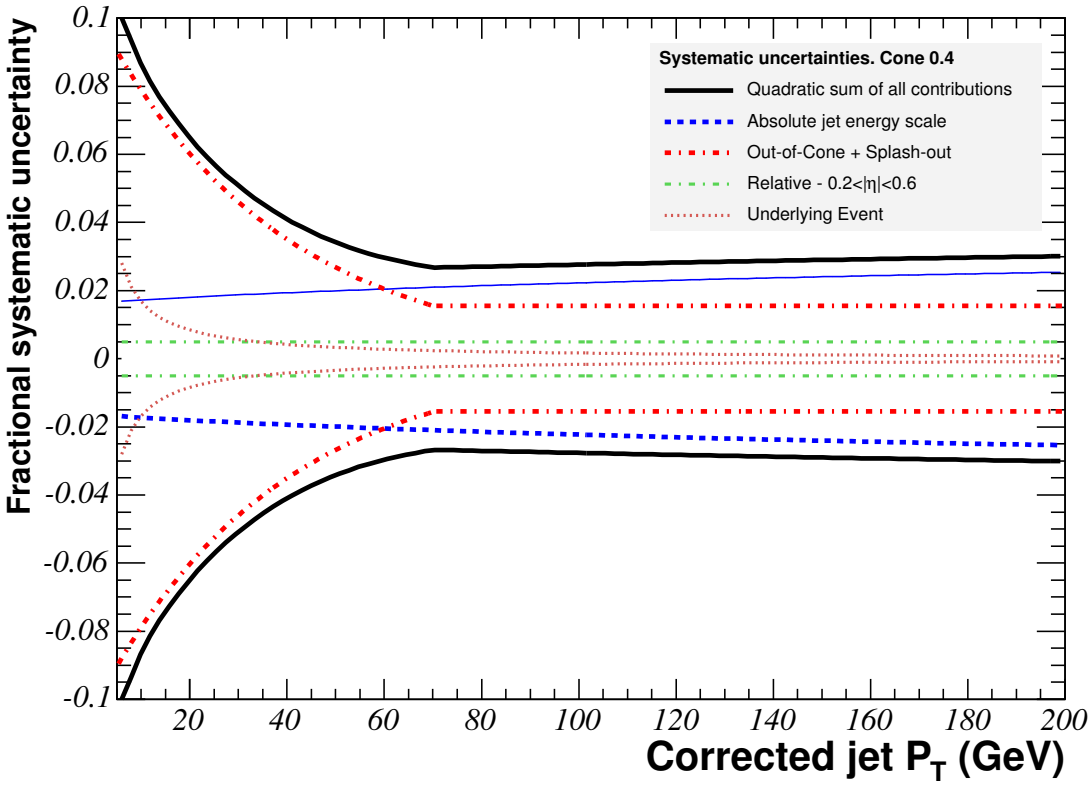

Figure 7.1: Fractional systematic uncertainty on jet energy corrections.

It is interesting to check the effect of the JES uncertainty on the modeling, especially for those variables where mismodeling was observed in Chapter 4. Figure 7.4 shows the modeling of the jet E_Ts, as well as ΔR_{jj} and p_{Tjj}. The mismodeling in the first and second jet E_T is mostly covered by the JES systematic uncertainty. The modeling of the dijet system is also significantly affected by the JES, but the discrepancy between data and Monte Carlo is not completely covered by this systematic uncertainty.

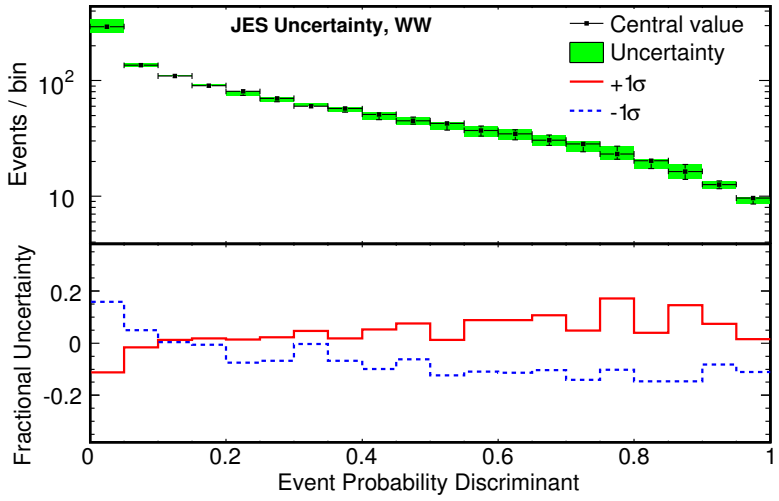

Figure 7.2: Change in the shape of the WW EPD template due to the JES uncertainty.

7.1.2 Parton distribution functions

The parton distribution functions (PDFs) used in generating the Monte Carlo models (see Section 4.1.1) are determined by fitting several different experimental results [20]. There are uncertainties associated with this fit, which are provided by the CTEQ collaboration in the form of alternate PDF sets. An additional uncertainty in the PDFs comes from the choice of Λ_{QCD}, a parameter that defines the strong coupling constant α_s in the parameterization. Two PDF parameterizations with different choices of Λ_{QCD} are provided by MRST [33]. In total 43 sets of PDFS are used to evaluate the uncertainty due to PDFs: CTEQ6M, the 20 pairs of uncertainty sets on CTEQ6M, MRST72, and MRST75.

Rather than regenerate the Monte Carlo samples with different PDFs, we reweight the generated samples according to the probability densities of the incoming partons in the systematically altered PDFs. Based on the reweighted samples, we determine the change in the signal acceptance due to the PDF uncertainty.

The uncertainties are combined as follows. The acceptance with each of the 20

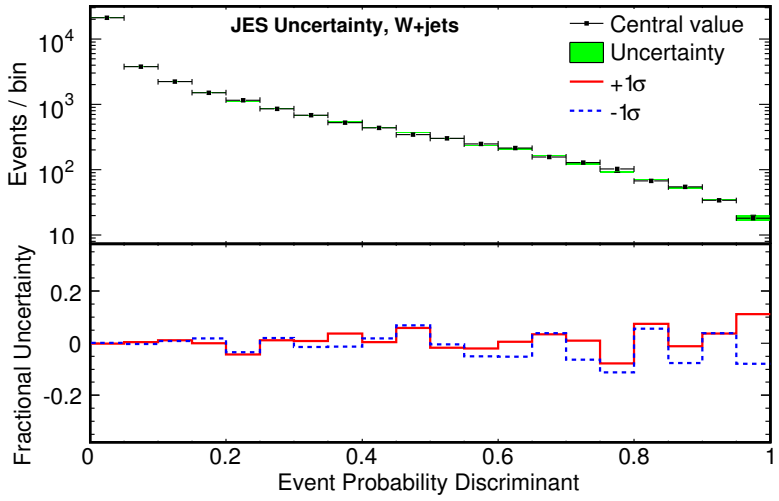

Figure 7.3: Change in the shape of the W+jets EPD template due to the JES uncertainty.

CTEQ6M uncertainty sets is compared to the central value; the 20 uncertainties are symmetrized and added in quadrature. The CTEQ6M uncertainty is then added in quadrature to the difference in acceptance between MRST72 and MRST75 [34]. The total uncertainty on the signal acceptance is found to be 2.5%.

7.1.3 Initial and final state radiation

The PYTHIA parameterization of initial and final state radiation (ISR and FSR) is controlled by certain parameters that have uncertainties associated with them. Careful comparison with data determined reasonable uncertainties for these parameters. The signal WW and WZ samples were generated with the level of ISR and FSR increased and decreased, and the change in the acceptance was estimated [34]. This results in a rate uncertainty of about 5% on the signal.

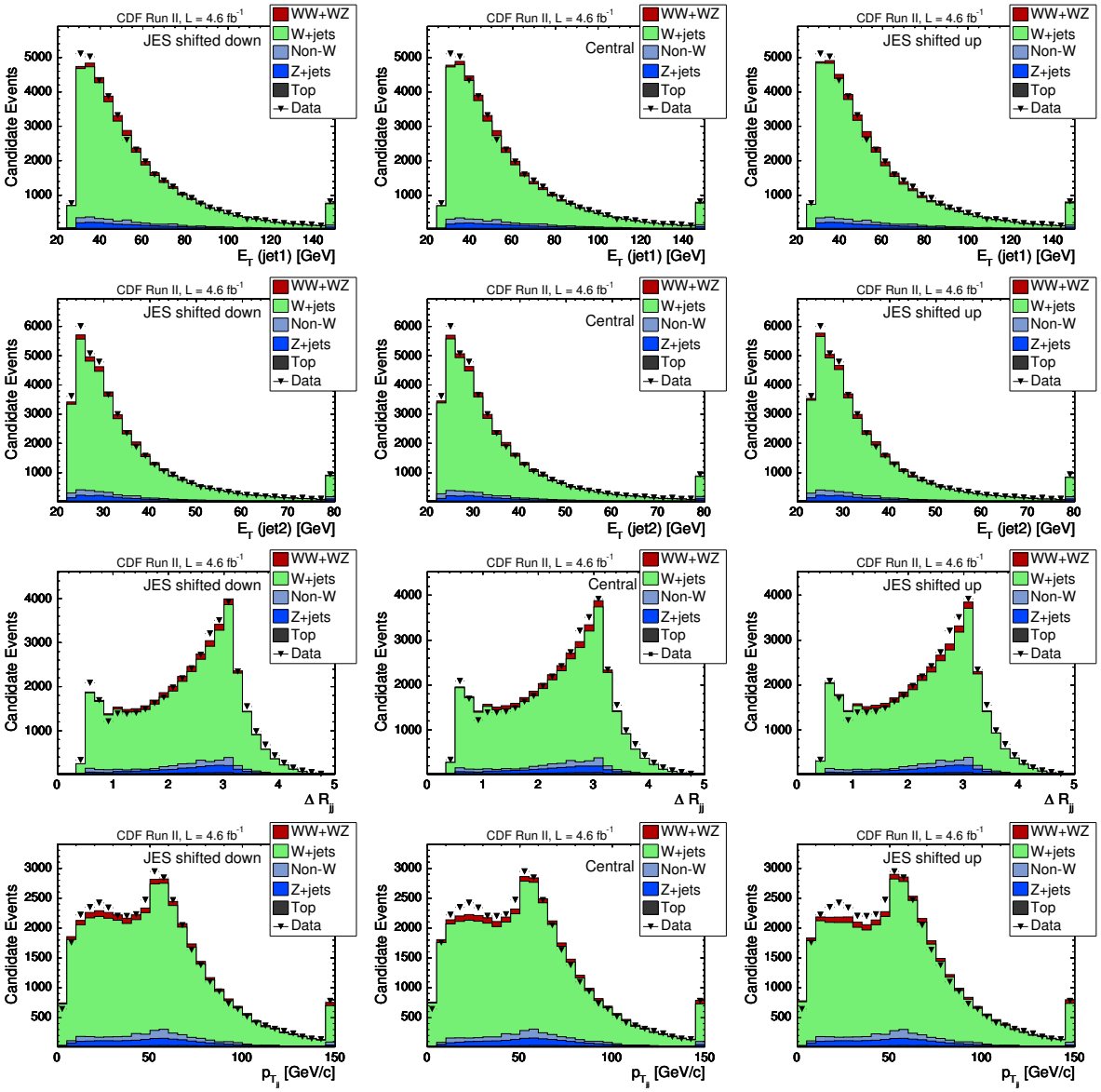

Figure 7.4: Modeling of various variables with the JES shifted down by 1σ (left), the central value of the JES (center), and the JES shifted up by 1σ (right). The top row shows the E_T of the higher-E_T jet, the second row shows the E_T of the second jet, the third row shows the ΔR between the two jets, and the fourth row shows the p_T of the dijet system.

7.1.4 Jet energy resolution

The modeling of the jet energy resolution can be a source of systematic uncertainty. First, it can affect the signal acceptance: if the dijet resonance is wider, more signal events may fall below the jet E_T thresholds or outside of the dijet mass window used in the fit. Second, the modeling of the jet energy resolution is used in deriving the transfer functions used in the matrix element calculation. If the resolution in data is significantly different, the shape of the EPD could be affected.

The Monte Carlo description of the jet resolution is compared to the resolution in data in γ+jet and dijet events. The uncertainty in the jet energy resolution is found to vary as $\Delta(\sigma/p_T) = 0.03 \pm 1.7/p_T$ [35].

We first determine the effect of the systematic in the direction leading to a wider resolution: $0.03+1.7/p_T$. Both jets in the event are smeared by an additional factor, and the matrix element calculation was repeated. The effect on the shape is negligible, so no shape uncertainty is taken into account. The acceptance is also re-derived, and found to decrease by 1%.

Since the effect of this uncertainty is so small, we do not investigate the effect of a narrower resolution, which is more difficult to model. Just a 1% uncertainty on the acceptance is imposed.

7.1.5 Background normalizations

The background normalizations are considered part of the statistical uncertainty in this measurement. In the likelihood fit, however, they are treated like other systematic uncertainties.

The uncertainty on the W+jets normalization is taken to be 20%, significantly more conservative than either the measured or theoretical cross section uncertainty. The value chosen for this uncertainty is unimportant since the likelihood fit ultimately constrains the W+jets cross section to a few percent.

The normalization of the non-W background was derived from a fit to the $\not\!\!E_T$ spectrum as described in Chapter 4. The uncertainty on this normalization associated with using different non-W models was investigated and a conservative uncertainty of 40% is assigned.

The uncertainties on the Z+jets, single top, and $t\bar{t}$ normalizations are estimated from the uncertainty in their cross sections and uncertainty in the Monte Carlo acceptance [25, 26, 27]. The single top and $t\bar{t}$ sources of uncertainty are closely correlated, so the normalization uncertainties in these two backgrounds are correlated in the likelihood fit.

Table 7.2 summarizes the size of the uncertainties on the background normalizations.

Background	Normalization uncertainty
W+jets	20%
Z+jets	15%
non-W	40%
$t\bar{t}$ and single top	12%

Table 7.2: Uncertainties in the background normalizations.

7.1.6 Factorization and renormalization scale

The factorization and renormalization scale, or Q^2 scale, is a parameter in the perturbative expansion used to calculate matrix elements in ALPGEN. There is no correct value for this scale since it is an artifact of perturbation theory. Higher-order calculations become

less dependent on the choice of scale, but ALPGEN is a leading-order generator and its modeling can be affected by the choice of scale.

The default choice in ALPGEN is $Q^2 = m_W^2 + \Sigma m_T^2$, where m_W is the mass of the W boson, m_T is the transverse mass, and the summation is over all final-state partons. ALPGEN W+jets samples were generated with the default scale doubled and divided by two. The effect of this change in scale on the modeling of the jet E_Ts and the dijet variables is shown in Figure 7.5. The shapes of several W+jets kinematic distributions are significantly changed.

The change in the shape of the W+jets EPD associated with the use of different Q^2 scales is shown in Figure 7.6. This change due to the Q^2 scale is considered a 1σ uncertainty, but we truncate the uncertainty at 1σ to avoid extrapolation to larger shape changes. We note that the treatment of this uncertainty is somewhat arbitrary in that there are several other possible choices of scale and the definition of 1σ is not unique.

7.1.7 W+jets modeling

As described above, the JES and Q^2 scale uncertainties cover some discrepancies observed between the Monte Carlo modeling and the data, particularly in the jet E_Ts. But the large discrepancy observed in the p_T of the dijet system shown in Figure 4.14 is not covered by either of these uncertainties. As a result we assign a systematic uncertainty to account specifically for the mismodeling observed in this variable.

The mismodeling in p_{Tjj} is present in both electron and muon channels. In the electron channel, the non-W background is somewhat larger than in the muon channels, and the modeling of the background is statistically limited. In order to avoid being affected by the non-W modeling of p_{Tjj}, we use only the central muon samples (CMUP + CMX) to derive the systematic uncertainty.

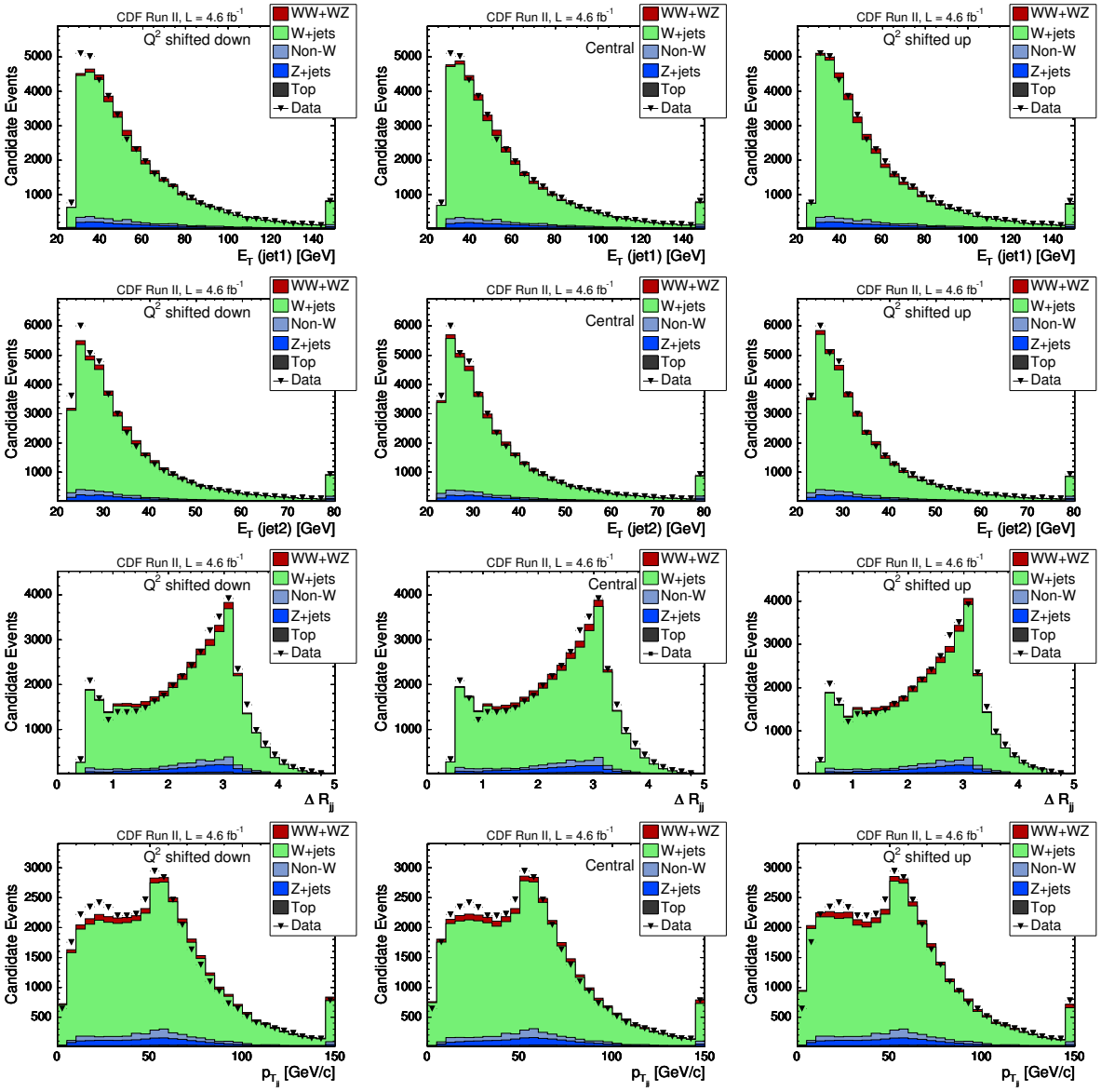

Figure 7.5: Modeling of various variables with the Q^2 scale decreased by a factor of two (left), the central choice of Q^2 scale (center), and the Q^2 scale increased by a factor of two (right). The top row shows the E_T of the higher-E_T jet, the second the E_T of the second jet, the third the ΔR between the two jets, and the fourth the p_T of the dijet system.

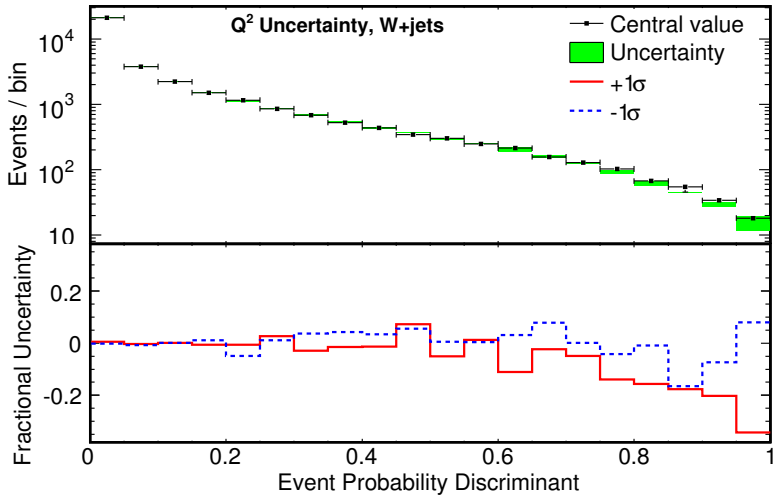

Figure 7.6: Uncertainty on the shape of the W+jets EPD template due to the Q^2 scale uncertainty.

The basic strategy we use to derive the uncertainty associated with mismodeling in a certain variable is to reweight the Monte Carlo models as a function of that variable until agreement is achieved. The systematically varied EPD template is then derived from the reweighted Monte Carlo. It is possible to bias the measurement by doing this: if one requires the Monte Carlo models to look exactly like data in the signal region, the measurement will favor a result that is close to the expectation. In order to avoid biasing the result, we remove the signal region with $55 < M_{jj} < 120$ GeV from the samples and data used to derive the weights.

The effect of reweighting $p_{T\,jj}$ on the W+jets EPD is shown in Figure 7.7. The change in the EPD shape is relatively small. The same shape uncertainty is imposed in the Z+jets background model, since the W+jets and Z+jets models should have roughly equivalent mismodeling in the dijet system. The change in the template is considered a 1σ uncertainty, but the uncertainty is truncated at 1σ so that the shape uncertainty is not further extrapolated.

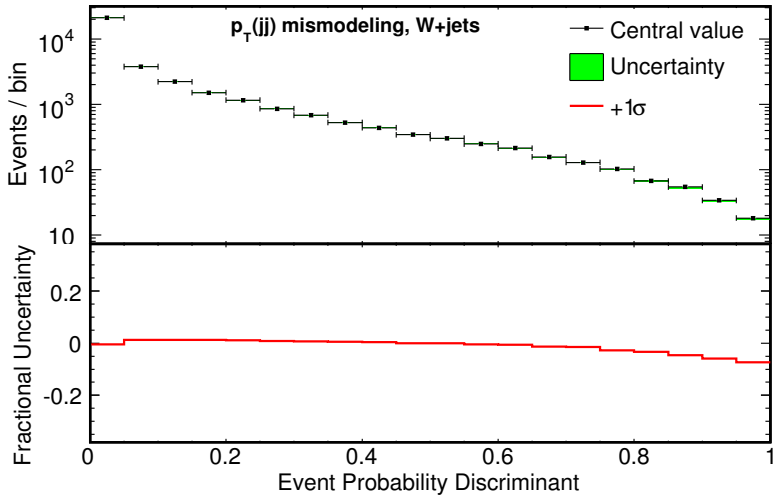

Figure 7.7: Uncertainty on the shape of the W+jets EPD template associated with p_{Tjj} mismodeling.

An equivalent uncertainty is imposed to deal with mismodeling observed in the η of the second jet in the event, shown in Figure 4.6. The change in the W+jets EPD template associated with this uncertainty is shown in Figure 7.8. The change in the shape is very small and unlikely to affect the outcome of the measurement.

7.1.8 Integrated luminosity

The integrated luminosity of the data sample is calculated from the rate of inelastic collisions observed in the CLC (see Section 2.2.5). The rate is converted to luminosity using the total inelastic $p\bar{p}$ cross section and the acceptance of the CLC detector. The inelastic cross section is estimated from previous CDF measurements [36] while the acceptance is estimated from the detector simulation. The total uncertainty in the integrated luminosity calculation is 6%.

All signal and background samples except for the non-W and W+jets samples (whose normalizations were determined from a fit to the data) have a 6% uncertainty on their

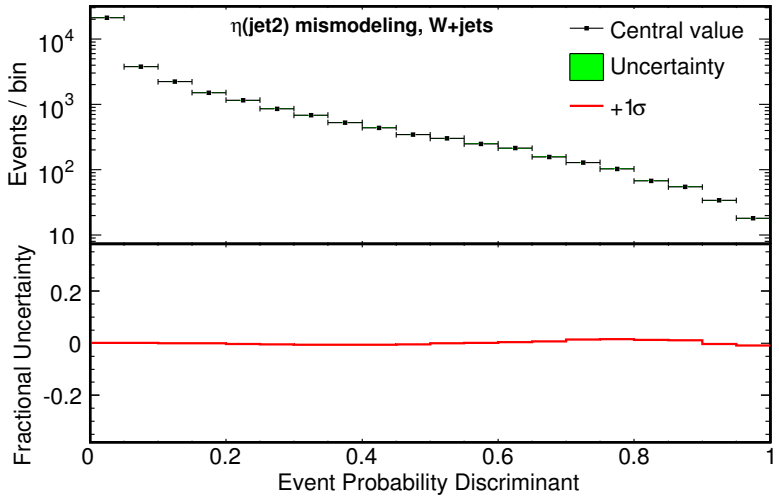

Figure 7.8: Uncertainty on the shape of the W+jets EPD template associated with the mismodeling in the η of the second jet.

normalizations due to the the luminosity uncertainty.

7.1.9 Trigger and lepton identification efficiencies

The efficiencies of the triggers and lepton identification can both be determined in data by using pure samples of Z bosons decaying to two leptons. The uncertainty on the trigger efficiency is dependent on the trigger selection, but is always less than 1.5%. The lepton identification efficiency is compared in data and Monte Carlo and a scale factor corrects the Monte Carlo efficiencies to agree with the data. The uncertainty on the scale factor is also less than 1%. As a result a "lepton identification uncertainty" of 2% is applied on the normalization on all samples except for the non-W and W+jets samples.

7.1.10 Monte Carlo statistics

The uncertainty due to limited Monte Carlo statistics does not fall into any of the categories mentioned at the beginning of this section: it is not an overall rate uncertainty

or a shape uncertainty that is correlated across bins. Rather it is a bin-by-bin statistical uncertainty, in principal given by the square root of the number of Monte Carlo events in the bin. The Monte Carlo samples are weighted, however, so the uncertainty is actually the sum in quadrature of the weights in a bin. The technical implementation of this uncertainty involves the introduction of a separate nuisance parameter for each bin.

7.2 Expected effects of systematic uncertainties

The expected uncertainty on the cross section measurement was determined by running pseudo-experiments, as described in Chapter 6. The effect of each systematic uncertainty individually was determined by adding the uncertainties one-by-one to the statistical uncertainty.

The statistical uncertainty can be defined in different ways. In this analysis, we consider the background normalization uncertainties as well as the Monte Carlo statistical uncertainties part of the statistical uncertainty.

The order in which systematic uncertainties are added or removed affects the outcome of this test. As a result the contribution of each uncertainty itself has an associated uncertainty.

Table 7.3 shows the expected contribution of each uncertainty to the uncertainty on the diboson cross section measurement. The statistical uncertainty and the total systematic uncertainty are roughly the same size. The dominant systematic uncertainties are due to the JES, the Q^2 scale, and the luminosity.

Uncertainty	Contribution to σ_{WW+WZ} uncertainty (%)
Statistical	14
JES	8 ± 1
JER	0^{+2}_{-0}
Q^2 scale	7 ± 1
p_{TJJ} mismodeling	2 ± 2
η_2 mismodeling	0^{+2}_{-0}
PDF	2^{+1}_{-2}
IFSR	4 ± 2
Luminosity	6 ± 1
Event selection efficiency	2 ± 1
Total	21

Table 7.3: Expected uncertainties on the measurement of the $WW + WZ$ cross section.

7.2.1 Uncertainties constrained by the measurement

As described in Section 6.1.1, the likelihood fit can effectively constrain some nuisance parameters. We determine whether or not an uncertainty is expected to be constrained by calculating the standard deviation (width) of the posterior p.d.f. for each nuisance parameter. If the standard deviation of the posterior p.d.f. is smaller than the width of the prior p.d.f., the uncertainty is constrained. Table 7.4 shows the expected width of the posterior p.d.f. as a percentage of the width of the prior p.d.f.

The normalization of the W+jets background is expected to be highly constrained to 9% of the width of its prior p.d.f. This makes sense, because there are several high-statistics EPD bins where the W+jets contribution is dominant which can constrain the normalization of this background.

The jet energy scale is also expected to be well-constrained by the fit. This is probably because of the large change in the shape of the EPD associated with the JES uncertainty. The data will be able to use this large difference in shapes to constrain the JES.

Nuisance parameter	Expected posterior width (% of prior width)
W+jets normalization	9.2
Z+jets normalization	86
non-W normalization	72
Top normalization	98
ZZ normalization	98
JES	43
JER	98
W+jets Q^2 scale	65
W+jets p_{TJJ} mismodeling	93
W+jets η_2 mismodeling	99
PDF	98
IFSR	99
Event selection efficiency	98
Luminosity	96

Table 7.4: Average width (standard deviation) of the posterior probability density function of the nuisance parameters for 3000 pseudo-experiments. A width of 100% indicates an unconstrained nuisance parameter.

Other nuisance parameters that are expected to be somewhat constrained are the Z+jets normalization, the non-W normalization, and the Q^2 scale.

CHAPTER 8

RESULTS

The analysis described in the previous chapters is applied to a data sample corresponding to 4.6 fb^{-1} of integrated luminosity. The results of the fit to data are described in Section 8.1. Various cross-checks of the result are described in Section 8.2.

8.1 Fit to data

We fit the EPD distribution observed in data to a sum of EPD templates as described in Section 6.1. The data is shown superimposed on the predicted distribution in Figure 8.1. The fit result for the $WW + WZ$ cross section is $\beta = \sigma_{meas}/\sigma_{NLO} = 1.09^{+0.22}_{-0.20}$, corresponding to a measured cross section of $\sigma(p\bar{p} \to WW + WZ) = 16.5^{+3.3}_{-3.0}$ pb. The result is in good agreement with the predicted $WW + WZ$ cross section at next-to-leading order (NLO) of 15.1 ± 0.9 pb. The posterior probability density for the cross section from the fit to the data is shown in Figure 8.2.

We extract the p-value and significance of the measurement, shown in Figure 8.3. The signal corresponds to a 5.4σ excess, where 5.1σ was expected.

8.2 Cross-checks

8.2.1 Results in each channel

As a cross-check, we perform the fit in each lepton channel separately: central electrons, central muons, and extended muons. The results are shown in Table 8.1. The measured

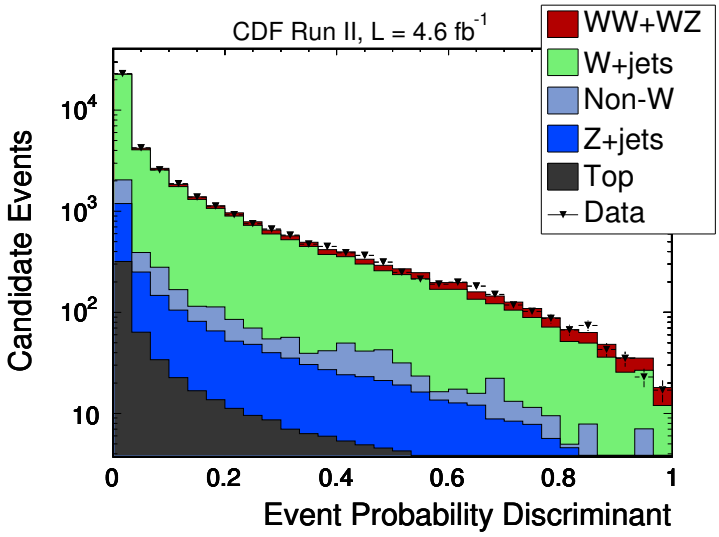

Figure 8.1: Stacked EPD templates with data superimposed.

cross sections are consistent with each other and with the total result.

Central electrons	Central muons	Extended muons	All
$1.05^{+0.31}_{-0.28}$	$1.26^{+0.31}_{-0.28}$	$0.82^{+0.48}_{-0.41}$	$1.10^{+0.23}_{-0.20}$

Table 8.1: Fitted $\beta = \sigma_{meas}/\sigma_{NLO}$ for the $WW + WZ$ cross section when the fit is performed in the three lepton channels independently and when performed over the three channels.

8.2.2 Nuisance parameter posterior values

The behavior of the fit in the data is investigated further by examining the posterior p.d.f.s of the nuisance parameters. The mean of the posterior p.d.f. corresponds to the most likely value of the nuisance parameter, whereas its standard deviation (width) indicates the constraint placed on the nuisance parameter by the fit. These values are summarized in Table 8.2, along with the expected constraints. The fitted values of the nuisance parameters are all well within 1σ of the mean of the prior p.d.f. and the fitted constraints

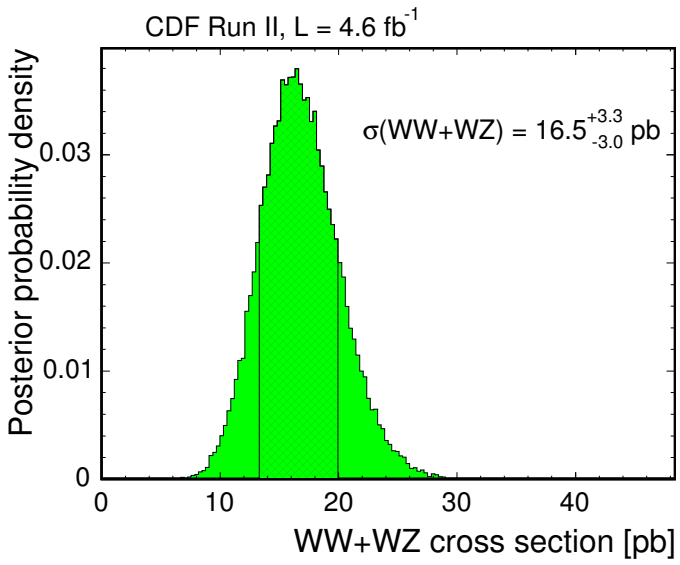

Figure 8.2: Posterior probability density for the $WW + WZ$ cross section.

match the expected constraints well. The W+jets normalization is very well constrained, as expected, to 10% of the width of its prior p.d.f (20%). This corresponds to a constraint of 2% on the W+jets normalization.

8.2.3 Fit using the dijet mass

We repeat the analysis, fitting the invariant mass of the two jets (again, we refer to this as the dijet mass or M_{jj}) rather than the EPD. In principle the dijet mass distribution will exhibit a resonance close to the W/Z mass for our signal (since the two jets are products of a W or Z decay), whereas for the background it will be smoothly falling. However the event selection sculpts the shape of M_{jj}, as shown in Figure 8.4. Nonetheless there is a difference between the expected signal and background shapes which can be exploited to extract the $WW + WZ$ signal.

We do not expect the fit to the dijet mass to be as sensitive as the fit to the EPD. The EPD has regions with higher signal-to-background ratios (S/B) than the dijet mass: for

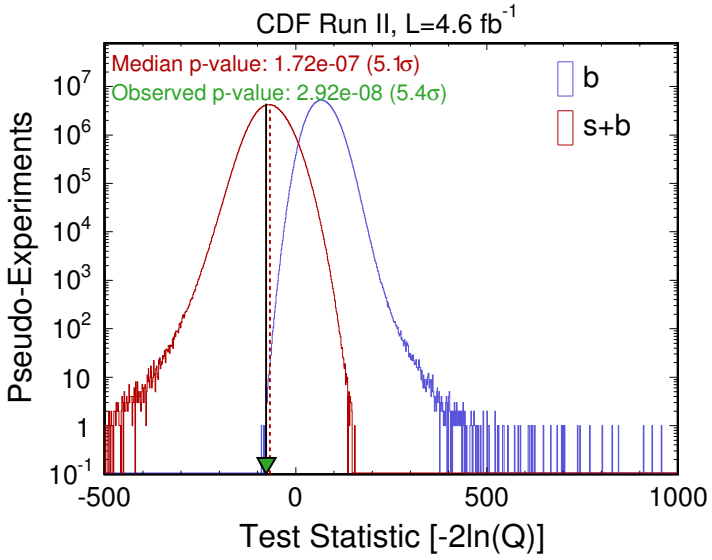

Figure 8.3: Expected and observed significance and p-value.

the most signal-rich bin in the M_{jj} distribution, $S/B = 0.13$ whereas the most signal-rich bin of the EPD has $S/B = 0.50$. The region with higher S/B in the EPD will increase the significance of the measurement. Based on pseudo-experiments, the expected sensitivity of the measurement with the dijet mass is 4.7σ, whereas with the EPD it is 5.1σ.

The precision of the cross section measurement, on the other hand, is expected to be better with the dijet mass than with the EPD. While the same systematic uncertainties are taken into account in both fits, their effects on the measurement are different. The JES and Q^2 scale have a significantly smaller effect when fitting M_{jj} than when fitting the EPD, whereas the uncertainty on the shape of $p_{T\,jj}$ is more important when fitting M_{jj}. Based on pseudo-experiments, the expected total uncertainty on the cross section measurement using the dijet mass is 19%, compared to the 21% expected with the EPD.

The result of fitting the dijet mass distribution in the data gives a cross section of $11.8^{+3.0}_{-2.7}$ pb. The result is compared to the result from the matrix element analysis and the predicted cross section at NLO in Table 8.3. The fitted cross sections are both con-

Nuisance parameter	Fitted value (% of 1σ)	Fitted constraint (% of prior width)	Expected constraint (% of prior width)
W+jets normalization	-3	10	9
Z+jets normalization	+9	87	86
non-W normalization	-40	76	72
Top normalization	-10	102	98
ZZ normalization	-2	97	98
JES	-48	42	43
JER	+11	100	98
W+jets Q^2 scale	-44	69	65
W+jets p_{Tjj} mismodeling	0	95	93
W+jets η_2 mismodeling	-4	100	99
PDF	+11	104	98
IFSR	-6	104	99
Event selection efficiency	-17	104	98
Luminosity	-1	101	96

Table 8.2: Posterior values of nuisance parameters after fitting data. Values are given as percentage of the prior width.

sistent with the prediction. There is some difference between the results from the matrix element analysis and the results from the dijet mass analysis. To determine whether the difference is significant, the correlation between the two analyses must be determined. The correlation was estimated by generating correlated pseudo-experiments based on our models; systematic uncertainties were not taken into account for this test. We expect roughly a 60% correlation between the two fits, meaning the discrepancy between the two results is at the 1.8σ level.

Matrix element	Dijet mass	Theory (NLO)
$16.5^{+3.3}_{-3.0}$ pb	$11.8^{+3.0}_{-2.7}$ pb	15.1 ± 0.8 pb

Table 8.3: Fitted cross sections from fits to the matrix element discriminant and the dijet mass compared to the predicted cross section at NLO.

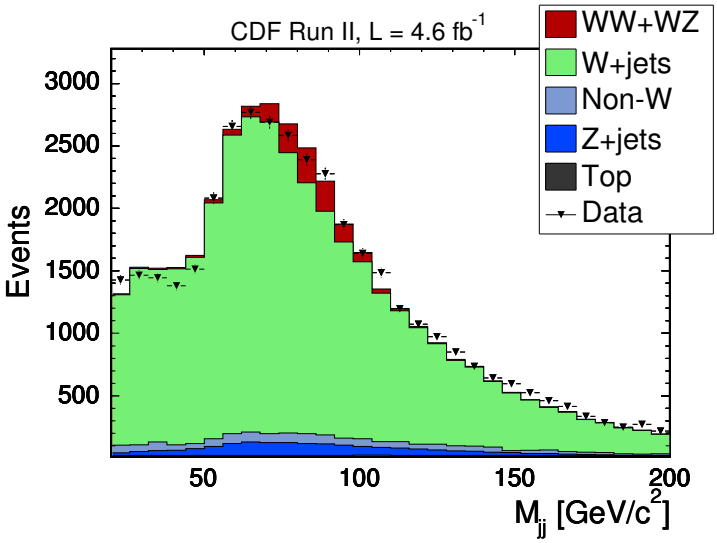

Figure 8.4: Stacked dijet mass distributions with data superimposed.

The p-value and significance of the measurement with M_{jj} is shown in Figure 8.5. The observed significance is 3.5σ, while 4.7σ is expected.

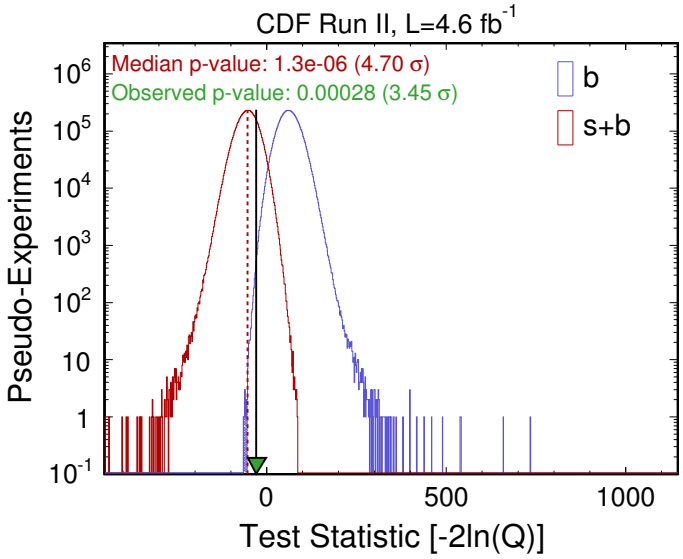

Figure 8.5: Expected and observed p-value and significance from a fit to the dijet mass.

CHAPTER 9

CONCLUSIONS

I have presented the measurement of the $WW + WZ$ production cross section in the channel with an identified electron or muon and two jets. The measurement was carried out in 4.6 fb^{-1} of integrated luminosity from $p\bar{p}$ collisions at $\sqrt{s} = 1.96$ TeV collected by the CDF II detector.

The first challenge was to observe the signal in a channel with large backgrounds primarily due to W+jets. The first observation of $WW + WZ$ production in the lepton plus jets final state was achieved previously. This thesis presents the details of the method used for that observation, with some improvements and a larger data sample. The analysis in this thesis confirms the observation of $WW + WZ$ production in the lepton plus jets final state with a significance of 5.4σ.

The cross section is measured to be $\sigma(p\bar{p} \to WW + WZ) = 16.5^{+3.3}_{-3.0}$ pb, consistent with the theoretical prediction at next-to-leading order. This result is the most precise measurement of the $WW + WZ$ cross section in this decay channel at the Tevatron.

The expected systematic uncertainty on the cross section measurement is larger than the expected statistical uncertainty. Improving the precision of the cross section measurement in this channel will require further study of the major sources of systematic uncertainty: the jet energy scale, the Q^2 scale, and the modeling of initial and final state radiation. All of these are correlated, probably making our current estimate of their effect too conservative.

This measurement represents an important milestone in the search for the Higgs boson at the Tevatron. Similar techniques to those presented here are used in the search for a Higgs boson with mass less than 135 GeV. This measurement establishes the validity of these techniques and improves our understanding of the important backgrounds and systematic uncertainties for that search.

REFERENCES

[1] C. Amsler *et al.* (Particle Data Group). 2008 Review of Particle Physics. *Phys. Lett.*, B667:1, 2008.

[2] J. M. Campbell and R. K. Ellis. Update on Vector Boson Pair Production at Hadron Colliders. *Phys. Rev.*, D60:113006, 1999.

[3] D0 collaboration. Measurement of the WW Production Cross Section with Dilepton Final States in $p\bar{p}$ Collisions at $\sqrt{s} = 1.96$ TeV and Limits on Anomalous Trilinear Gauge Couplings. arXiv:hep-ex/0904.0673, submitted to Phys. Rev. Lett., 2009.

[4] CDF Collaboration. Measurement of the WW Production Cross Section in $p\bar{p}$ collisions at $\sqrt{s} = 1.96$ TeV using 3.6 fb^{-1} of CDF Run II Data. CDF Public note 9753, 2009.

[5] V. Abazov *et al.* (D0 Collaboration). Measurement of the $p\bar{p} \rightarrow WZ + X$ cross section at $\sqrt{s} = 1.96$ TeV and limits on WWZ trilinear gauge couplings. *Phys. Rev.*, D76:111104, 2007.

[6] A. Abulencia *et al.* (CDF Collaboration). Observation of WZ Production. *Phys. Rev. Lett.*, 98:161801, 2007.

[7] T. Aaltonen *et al.* (CDF Collaboration). First Observation of Vector Boson Pairs in a Hadronic Final State at the Tevatron Collider. *Phys. Rev. Lett.*, 103:091803, 2009.

[8] V. M. Abazov *et al.* (D0 Collaboration). Evidence of $WW + WZ$ Production with Lepton + Jets Final States in Proton-Antiproton Collisions at sqrt(s) = 1.96 TeV. *Phys. Rev. Lett.*, 102:161801, 2009.

[9] CDF collaboration. Measurement of the $WW+WZ$ Production Cross Section Using the Lepton + Jets Final State at CDF II. arXiv:hep-ex/0911.4449, submitted to Phys. Rev. Lett., 2009.

[10] T. Aaltonen *et al.* (CDF Collaboration). First Observation of Electroweak Single Top Quark Production. *Phys. Rev. Lett.*, 103:092002, 2009.

[11] V.M. Abazov *et al.* (D0 Collaboration). Observation of Single Top Quark Production. *Phys. Rev. Lett.*, 103:092001, 2009.

[12] T. Aaltonen *et al.* (CDF Collaboration). Search for a Standard Model Higgs boson in $WH \rightarrow l\nu b\bar{b}$ collsions at $\sqrt{s} = 1.96$ TeV. *Phys. Rev. Lett.*, 103:101802, 2009.

[13] Tevatron. http://www-bdnew.fnal.gov/tevatron/.

[14] Cdf. http://www-cdf.fnal.gov/.

[15] A. Bhatti *et al.* Determination of the Jet Energy Scale at the Collider Detector at Fermilab. *Nucl. Instrum. Methods*, A566:375, 2006.

[16] T. Sjöstrand, S. Mrenna and P. Skands. PYTHIA 6.4 physics and manual. *JHEP*, 0605:026, 2006. arXiv:hep-ph/0603175.

[17] M. L. Mangano *et al.* ALPGEN: A generator for hard multiparton processes in hadronic collisions. *JHEP*, 0307:001, 2003.

[18] S. Hoeche *et al.* Matching Parton Showers and Matrix Elements. In *Proceedings of the HERA and the LHC workshop.*

[19] J. Alwall *et al.* `MadGraph/MadEvent` v4: the next web beneration. *JHEP*, 0709:028, 2007.

[20] J. Pumplin *et al.* New Generation of Parton Distributions with Uncertainties from Global QCD Analysis. *JHEP*, 0207:012, 2002.

[21] R. Brun and F. Carminati. GEANT Detector Description and Simulation Tool. *CERN Programming Library Long Writeup*, W5013, 1993.

[22] E. Gerchtein and M. Paulini. CDF Detector Simulation Framework and Performance. In *CHEP03 Conference Proceedings*, 2003.

[23] R. Veenhof. GARFIELD, a drift chamber simulation program. Version 6.22, CERN.

[24] G. Grindhammer, M. Rudowicz, and S. Peters. The Fast Simulation of Electromagnetic and Hadronic Showers. *Nucl. Instrum. Methods*, A290:469, 1990.

[25] D. Acosta *et al.* (CDF Collaboration). First Measurements of Inclusive W and Z Cross Sections from Run II of the Fermilab Tevatron Collider. *Phys. Rev. Lett*, 94:091803, 2005.

[26] M. Cacciari *et al.* Updated Predictions for the Total Production Cross Sections of Top and of Heavier Quark Pairs at the Tevatron and at the LHC. *JHEP*, 0809:127, 2008.

[27] B.W. Harris *et al.* Fully Differential Single-Top-Quark Cross Section in Next-to-Leading Order QCD. *Phys. Rev.*, D66:054024, 2002.

[28] Peter Dong. *Measurement of Electroweak Single Top Quark Production in Proton-Antiproton Collisions at 1.96 TeV.* PhD thesis, UCLA, 2008.

[29] T. Junk. Confidence level computation for combining searches with small statistics. *Nucl. Instrum. Methods*, A434:435, 1999.

[30] A.L. Read. Presentation of search results: the CL_s technique. *J. Phys.*, G28:2693, 2002.

[31] CDF Collaboration. Combined Upper Limit on Standard Model Higgs Boson Production for Winter 2009. CDF Public note 9674, 2009.

[32] L. Demortier. Pulls. CDF Public note 5776, 2001.

[33] A.D. Martin *et al.* Parton Distributions and the LHC: W and Z Production. *Eur. Phys. J*, C14:133, 2000.

[34] A. Abulencia *et al.* (CDF Collaboration). Top Quark Mass Measurement Using the Template Method in the Lepton + Jets Channel at CDF II. *Phys. Rev.*, D73:032003, 2006.

[35] T. Aaltonen *et al.* (CDF Collaboration). First direct bound on the total width of the top quark in $p\bar{p}$ collisions at $\sqrt{s} = 1.96$ TeV. *Phys. Rev. Lett.*, 102:042001, 2009.

[36] F. Abe *et al.* (CDF Collaboration). Measurement of the Antiproton-Proton Total Cross Section at $\sqrt{s} = 546$ and 1800 GeV. *Phys. Rev.*, D50:5550, 1994.